



POLITÉCNICA

CERN-THESIS-2020-415
// 2020



ESCUELA TÉCNICA SUPERIOR DE INGENIEROS INDUSTRIALES
UNIVERSIDAD POLITÉCNICA DE MADRID

José Gutiérrez Abascal, 2. 28006 Madrid
Tel.: 91 336 3060
info.industriales@upm.es

www.industriales.upm.es



Lorena Vega Cid

05 TESIS DOCTORAL

INDUSTRIALES

TESIS DOCTORAL

THERMAL MODELLING, CONCEPTION AND DESIGN OF A COOLING SYSTEM FOR THE LHC INJECTION KICKER MAGNETS TOWARDS HIGH LUMINOSITY LHC OPERATION

SEPTIEMBRE 2020

Lorena Vega Cid

DIRECTOR DE LA TESIS DOCTORAL:

Alberto Abánades Velasco

TESIS DOCTORAL
PARA LA OBTENCIÓN DEL
TÍTULO DE **DOCTOR**



POLITÉCNICA

Declaration

I hereby declare that except where specific reference is made to the work of others, the contents of this dissertation are original and have not been submitted in whole or in part for consideration for any other degree or qualification in this, or any other university. This dissertation is my own work and contains nothing which is the outcome of work done in collaboration with others, except as specified in the text and Acknowledgements.

Lorena Vega Cid
September 2020

Acknowledgements

This thesis is the result of fruitful collaboration and support from many people, and I would like to acknowledge their contributions to the completion of this work.

First of all, I would like to highlight the guidance from my supervisors at CERN, **Mike Barnes** and **Wim Weterings**. I was encouraged to pursue the PhD thanks to the trust they placed in me since the very beginning. They have been key figures in the development of this thesis and I have learned a lot from both of them, from a professional and personal approach.

From Mike I have learnt to be meticulous with the theoretical studies, to apply the scientific method with rigor and, ultimately, to enjoy the research and work with passion. He has always closely followed my progress, giving useful ideas and providing technical guidance. We had very fruitful discussions regarding the results of all the simulations I performed, and very nice ideas came out of these discussions. He was organizing regularly technical meetings with colleagues of the working group, giving me the opportunity to show the progress of my studies and discuss with experts. This also helped me to improve my skills for giving oral presentations and he was always giving good advice on how to structure the information. Regarding the technical writing, he reviewed and corrected thoroughly all the publications and reports I wrote, providing useful feedback. Besides, he has invested a lot of time and effort in reading this thesis, even after I finished my contract at CERN. I cannot be more grateful for that.

On a personal level, I want to highlight the great humility that characterizes him, being always willing to invest his time to explain and discuss ideas, treating with a huge respect to all his colleagues and listening to everyone's ideas with interest. Indeed, he made me feel valued since the beginning and this had a great impact in growing self-confidence and bringing out the best of me.

Wim has contributed to the PhD with a more practical vision, which has been key in the development of this thesis. He has been a great complement to Mike's theoretical approach. He also followed very closely my studies, organizing weekly meetings to discuss and share ideas. He was giving very useful advises, especially when it came to discuss aspects of the mechanical design. I have profited a lot from his vast experience as a mechanical engineer, and thanks to his suggestions I could come up with an efficient design of the cooling system,

accounting for technical details that otherwise I would have missed, and ultimately, meeting successfully the goals of this thesis.

On the personal side, he has always shown a great willingness to help me, and thanks to his inclusive and easy-going personality, I have always felt integrated and valued. I admire his leadership ability. He takes care of all the members of his team, making efforts to maintain a good atmosphere and integrating all the members. Besides, I want to highlight his emphasis on the necessity of collaboration and communication between engineers and technicians, valuing their work in the same manner. I have seen how important this is for a mechanical design to be successful, from its conception to the production, assembly and commissioning. I would like to extend my gratitude to his team from **TE-ABT-EDS**, because they helped me to prepare the technical drawings and gave me support with the preparation of the 3D models for analysis; they were always kind and helpful to me.

Another key person in this thesis has been **Vasileios Vlachodimitropoulos**. He performed the electromagnetic studies with rigor and professionalism, which has been fundamental in the achievement of the goals of the thesis. The proposed solution was fruit of the collaboration between us, as his input was fundamental for properly assessing the cooling needs. I want to highlight the excellent communication between us, we spent hours brainstorming and many ideas emerged from these discussions. But his contribution to this thesis goes beyond the professional part. Apart from being an excellent colleague, he was a good friend, supporting me whenever I needed, and always finding good words to keep me motivated.

Apart from them, I want to extend the gratitude to all the colleagues from the group **TE-ABT**. Many of them took part in regular meetings to follow the progress, and offered their help with kindness whenever I needed. Besides, I want to highlight the contributions from my friend **Edmundo López**. He helped me in many occasions with the ANSYS simulations, always being willing to spend time to give me good advises and to discuss ideas. He also referred me to useful contacts from his section (EN-STI-TCD). I would like to highlight specially the help from **David Carbajo**, who helped me to properly define the thermo-structural model for analysis of the cooling system, **Lorenzo Teofili**, who showed me how to transfer correctly the heat loads from CST to ANSYS, which was key for the success of the studies, and **Giulia Romanogli**, who gave me very useful advises and referred me to contacts that lately were key for the production of the cooling system. One of these contacts was **Fritz Mostchmann**, who did a great job by finding a technique for brazing ferrite to copper, which was a key part in the design of the cooling system for improving the heat transfer. I was impressed by his professionalism and commitment to the job.

Apart from the help I have received from the colleagues at CERN mentioned above, I have also been supported by the colleagues from the ETSII (Escuela Técnica Superior de Ingenieros Industriales) from the UPM (Universidad Politécnica de Madrid). I am particularly grateful to the director of the thesis, **Alberto Abánades**, who has followed the project from the distance, being always willing to discuss ideas and keeping track of my progress. I also appreciate the feedback he has given about the publications and the thesis, and his help with the administrative procedures for the deposit of the thesis.

I also want to thank **Victor de la Peña**, from the ETSIB (Escuela Técnica Superior de Ingeniería de Bilbao). He was the director of my Master's thesis, and I had the chance to find not only a great professional but a good friend and advisor. He has helped me a lot since then, especially in the last steps of the thesis, referring me to contacts for being part of the tribunal of the thesis.

I wish to thank particularly the international experts that have reviewed my thesis, which was required for obtaining the international mention in the PhD: **Renuka Rajput-Ghoshal**, from JLab in USA, and **Hernán Furci**, from EPFL in Switzerland. They kindly accepted to review the thesis, providing useful feedback and demonstrating great professionalism and commitment. I would like to thank **Anne-Marie Valente Feliciano**, **Mike Barnes**, **Giovanna Vandoni**, **Torsten Koettig** and **Alberto Abánades**, who helped me in finding or put me in contact with the above-mentioned experts.

Throughout these years, my family, from a distance, has always been by my side, providing unconditional support and trusting in my capabilities. Special thanks to my sister Miriam and Soraya, who have always encouraged me to fight for devoting my life to the scientific research, reminding me the vocation that moved me to start this adventure at CERN.

I cannot forget my friends of the "Council of Sages", Álvaro and Luised. Thanks to their wisdom and their particular sense of humour, I always found a reason to laugh in the coffee-pause. This helped me to overcome difficulties, as the best way to face them is with a smile. For this, I want to thank Jorge too, who has also been source of many smiles, being always by my side in this adventure. All in all, this experience has not only been about getting a PhD, but meeting great people. Unexpectedly, I have built a family far from my hometown, and I have created great memories these years thanks to them. Many of them have been, and will remain, an important part of my life.

Lastly, I would like to dedicate this thesis to my nephew Ander. Working at CERN was a dream for me. I still remember the first time I read about this place and how astonished I was with the beauty of the experiments they were performing here. I was at school back then, and even though working at CERN seemed unreachable for a 14-year old girl, I can say now that, with effort and passion, I have managed to get where I want to be. I hope this work serves

as inspiration for him and, if needed, helps him finding the courage to follow his vocation, whatever it will be.

Abstract

The CERN Large Hadron Collider is equipped with two fast single-turn injection kicker systems that deflect the incoming particle beam onto the accelerator's orbit. The high intensity LHC beam, circulating for many hours, can cause considerable heating of the injection kicker magnets. Finite element models have been developed and validated to study the beam induced heating and thermal behaviour of these magnets. These models are used to predict the power deposition and temperatures for various operation scenarios. According to predictions, heating issues are expected for High Luminosity LHC operation with high intensity beams unless appropriate measures are taken. Cooling of the magnet yokes is complicated as the magnets are in vacuum and are pulsed at high voltage. A description of the evolution of the studies is presented, culminating with the conception and design of a cooling system, which is thoroughly described, from the conception process to the final proposed solution.

Table of contents

List of figures	xv
List of tables	xxi
1 Introduction	1
1.1 Context	1
1.2 LHC Injection Kicker Magnets	3
1.3 Structure of the thesis	9
2 Background	11
2.1 Electromagnetic interactions of charged particles with accelerators' components	11
2.2 Literature review	14
3 Methodology	27
4 Thermal modelling of the MKI magnets	31
4.1 Analysis tools	31
4.1.1 Build the geometry	32
4.1.2 Mesh optimization	38
4.2 Modelling boundary conditions	43
4.2.1 Convection coefficient	43
4.2.2 Power loss	47
4.3 Presentation and validation of the models	53
5 Studied alternatives	63
5.1 Increasing thermal emissivity of vacuum tanks	63
5.1.1 Multilayer coating	66
5.1.2 Laser Engineered Surfaces	69
5.1.3 Chemical etching	73

5.1.4	Flame spray	75
5.1.5	Plasma spray	79
5.1.6	Summary of emissivity studies and conclusions	82
5.2	Removing the bake-out jackets	83
5.3	Cooling down the ferrite yokes	84
5.4	Cooling of ferrite rings	92
5.4.1	Upgraded magnet	95
6	Design of the water cooling system	99
6.1	Methodology	99
6.2	Results of studies	101
6.2.1	Proposal of design approach	102
6.2.2	Optimization of the system dimensions	107
6.2.3	Hydraulic system design	115
6.2.4	Building a prototype	120
7	Conclusions	127
7.1	Summary	127
7.2	Contributions to the state of the art	130
7.3	Future work	132
	References	133

List of figures

1.1	CERN Accelerator Complex [55].	2
1.2	LHC baseline plan showing the energy of the collisions (red) and luminosity (green) [16].	3
1.3	Four MKI kicker magnets in the LHC tunnel.	4
1.4	Lorentz force acting on the injected beam (positively charged particles) passing through the aperture of the MKIs.	5
1.5	Simplified schematic of LHC beam injection process for beam 1.	5
1.6	Pulse in a kicker magnet.	6
1.7	Internal view of a MKI magnet. Detail of the apertures for the injected and circulating beams.	7
1.8	CAD model of a MKI magnet.	8
1.9	Cross-section of CAD model of the upstream end of a MKI magnet.	8
2.1	Contraction of the electric field lines in ultra-relativistic particles [46].	12
2.2	Image charges induced in the walls of a vacuum pipe by a passing particle beam [39].	12
2.3	Distorted field lines due to non-uniform geometries and resistive materials [46]	13
2.4	Contribution of the HL-LHC beam normalized spectrum (BNS, in black) and the real part of the longitudinal impedance (in red) in the frequency domain to the calculation of the dissipated power in the TDIS (in blue) [72].	13
2.5	Effect of the beam screen and the ceramic (alumina) tube on the real part of the longitudinal impedance of the MKIs.	15
2.6	Screen conductors connected to the beam pipe.	16
2.7	Screen conductors at capacitively coupled end with metallization on the ceramic tube <i>Courtesy M. Barnes</i>	16
2.8	CST results of the expected impedance for different beam screen configurations: with 12, 19 an 24 conductors.	17
2.9	Real longitudinal impedance of the MKIs for different overlap lengths.	20

2.10	Initial 2D model for thermal simulations with ANSYS [®] Mechanical [™] . . .	20
2.11	Internal surface of vacuum tanks.	23
3.1	Methodology.	28
4.1	Power distribution for Run2 nominal parameters, averaged per group of components with similar power deposition <i>Courtesy: H. Day</i>	34
4.2	Comparison of results with a model of 16 cells and a model with 10 cells. . .	35
4.3	Slots for screen conductors in the beam screen.	35
4.4	Modelling alternatives of the beam screen. Model <i>a</i> : Reference. Models <i>b</i> , <i>c</i> , <i>d</i> : Proposed simplifications.	36
4.5	Simplification of the geometry of the HV plate. a) CATIA model with real dimensions. b) ANSYS model after simplification of the geometry: use of symmetry and removal of rounded edges and small holes.	38
4.6	Global Mesh controls. <i>Yellow: Settings that have been manually modified/ Blue: Relevant information</i>	39
4.7	Local Mesh Controls. <i>Yellow: Setting that have been modified</i>	41
4.8	Settings of MultiZone method. <i>Yellow: Settings that have been modified</i> . . .	42
4.9	ANSYS thermal model with mesh.	43
4.10	Convection coefficient obtained from Churchill and Chu correlation.	44
4.11	ANSYS ferrite temperature predictions for different values of the convection coefficient.	45
4.12	Cross-section of bake-out jacket (Thickness 28 mm)	46
4.13	Photo of a bake-out jacket.	46
4.14	ANSYS thermal model including the bake-out jackets.	47
4.15	Methodology to obtain the power loss distribution.	47
4.16	Scaling factor calculation.	49
4.17	Heat load introduced in the ferrite yokes in the 2D thermal model.	50
4.18	Heat load introduced in the ferrite yokes in the 3D thermal model.	50
4.19	Example heat load imported from CST introduced in the upstream ferrite rings. 51	
4.20	Example heat load imported from CST introduced in the upstream ferrite yokes.	51
4.21	One of the two PT100 located on the side plate.	52
4.22	PT100 located on the clamp next to the ferrite rings.	52
4.23	Comparison of the normalized power distribution for the different models used. 53	
4.24	LHC fill #4569 used for validation of Model 2, with the total power scaled by 3. <i>25 ns beam, 2244 bunches, 1.15e11 protons per bunch</i>	54

4.25	Measurements during LHC fills #5068 and #5069 and predictions for Model 3, with the total power scaled by 4 (25 ns beam, 2064 bunches, 1.27e11 protons per bunch).	55
4.26	Measurements during LHC fills #5068 and #5069 and predictions for Model 3, with total power scaled by 5 (25 ns beam, 2064 bunches, 1.27e11 protons per bunch).	56
4.27	Measured Tube_Up temperatures in the eight MKI magnets from 7/6/2017 to 26/6/2017.	56
4.28	Copper clamp for the PT100.	57
4.29	PT100 location.	57
4.30	Analysis of the suitability of the current PT100 locations and proposed alternatives (Fills #5068 and #5069).	58
4.31	Measurements during LHC fill #6719 and predictions for Model 4, with scaling factor of 2.4 (25 ns beam, 2544 bunches, 1.1e11 protons per bunch).	60
4.32	Measurements during LHC fill #6719 and predictions for Model 4, without scaling factor (25 ns beam, 2544 bunches, 1.1e11 protons per bunch.)	60
5.1	Maximum predicted temperature of the yoke vs emissivity of the vacuum tank. Simulation performed for Model#1 of power deposition (see Table 4.3). Total power: 616 W	64
5.2	Maximum predicted temperature per component for different thermal emissivity of the vacuum tank. Dashed red line: Curie temperature of ferrite types CMD5005/8C11 and 4M2 used in yokes and rings respectively. <i>Model 3 of power deposition for HL-LHC. Total power: 616W.</i>	64
5.3	Description of the multilayer interference in optical coatings.	67
5.4	Magnetron sputtering process [Denton Vacuum]	68
5.5	FTIR spectroscopy of the SS304L sample with multilayer coatings.	69
5.6	Photographs and scanning electron microscope images of laser treated copper samples (The treated part corresponds to the black square in each sample [70]	71
5.7	Emissivity measurements of the LESS treated SS304L sample.	72
5.8	Chemical etching process [71].	74
5.9	Emissivity measurements of the SS304L with chemical etching [71].	75
5.10	Cross sections of typical flame spray process with powder [74].	76
5.11	Emissivity measurements of the SS304L samples with flame sprayed coatings.	77
5.12	RGA scan normalised to mass peak 2 amu (red and blue) and acceptance thresholds (yellow) of Inconel 600 flame sprayed coating of SS304L (sample C). <i>Courtesy: J.A. Li Hellstrom</i>	79

5.13	Classification of thermal spray processes according to particle velocity and flame temperature [1].	80
5.14	Plasma spray process. Courtesy of Praxair Surface Technologies, Inc. [74].	80
5.15	Emissivity measurements of the SS304L with Al_2O_3 sprayed coating. . . .	81
5.16	RGA scan normalised to mass peak 2 amu (blue) and acceptance thresholds (red) of 100% fine Al_2O_3 plasma sprayed coating of SS304L sample. Courtesy: A.K. Riihimaki [60].	82
5.17	Temperatures predicted with and without bake-out jackets. Dashed red line: Curie temperature of ferrite types CMD5005/8C11 and 4M2 used in yokes and rings respectively. <i>Model 3 of power deposition for HL-LHC. Total power: 616W.</i>	83
5.18	Relation between the maximum temperature of the first yoke with and without jackets. <i>Model 3 of power deposition.</i>	84
5.19	Cross-section of an MKE magnet with details of the cooling system [73]. . .	85
5.20	<i>Case a:</i> Cold plate pressed against the yoke with cooling pipe connected at the bottom surface of the plate.	86
5.21	<i>Case b:</i> Cold plate pressed against the yoke with cooling loop embedded . .	87
5.22	<i>Case c:</i> Cooled horizontal ground plate.	87
5.23	Detail of the holes in the ground plate for the connection of the HV feedthrough to the coaxial cables.	89
5.24	Temperature for case <i>b</i> with embedded cooling pipes at 15°C and 25°C in contact with only the first ferrite yoke. Dashed red line: Curie temperature of ferrite types CMD5005/8C11 and 4M2 used in yokes and rings respectively. <i>Model 3 of power deposition for HL-LHC. Total power: 616W.</i>	90
5.25	Temperature for case <i>b</i> with cold plates attached to various yokes. Dashed red line: Curie temperature of ferrite types CMD5005/8C11 and 4M2 used in yokes and rings respectively. <i>Model 3 of power deposition for HL-LHC. Total power: 616W.</i>	91
5.26	Detail of the upstream ferrite rings with shorter metallic cylinder.	92
5.27	Power distribution for overlap lengths of 40 mm and 117 mm. <i>Model 3 of power deposition.</i>	93
5.28	Temperatures for overlap lengths of 40 mm and 117 mm, with (dotted lines) and without (continuous lines) cooling of the rings. Dashed red line: Curie temperature of ferrite types CMD5005/8C11 and 4M2 used in yokes and rings respectively. <i>Model 3 of power deposition for HL-LHC. Total power: 616W (reference) and 450W (modified).</i>	93

5.29	Normalised power distribution for 40 mm and 56 mm overlap lengths. . . .	95
5.30	Power distribution map in the upstream rings for the Post-LS1 and upgraded designs.	95
5.31	Predicted temperatures for maximum power expected in the upgraded magnet. Dashed red line: Curie temperature of ferrite types CMD5005/8C11 and 4M2 used in yokes and rings respectively. <i>Model 4 of power deposition. Total power: 100 W</i>	96
5.32	Comparison of the measured temperatures in all the magnets at the sensor located in the upstream end of the side plates during mid-2018.	97
6.1	Scheme of the methodology of the process.	99
6.2	Thermal network model for heat transfer.	102
6.3	Cold plate pressed to the flat surface of the ferrite tube.	105
6.4	Effect of the radial thickness of the ferrite on the real longitudinal beam impedance of the magnet [?]	108
6.5	Total power in ferrite cylinder as a function of the longitudinal length. . . .	109
6.6	Original configuration of the vacuum gap and the upstream end of the screen conductors [35].	109
6.7	Studied modifications of the transition between the metallic tube and the cooper tube to optimize the heat distribution [29].	110
6.8	Modified MKI beam screen configuration.	110
6.9	Expected power distribution along the longitudinal length of the ferrite cylinder with and without the insert.	111
6.10	Studied modifications of the vacuum gap and screen conductors to optimize the heat distribution.	112
6.11	Azimuthal distribution of power in the ferrite cylinder with different beam screen configurations [79].	112
6.12	Real part of longitudinal beam coupling impedance for different configurations of the beam screen design [79].	113
6.13	Maximum temperature in ferrite cylinder versus thermal contact conductance at the joint between the ferrite and copper tube. <i>Safety factor of 2.5 included in the power.</i>	113
6.14	Temperatures obtained with and without cooling system. <i>Model 4 of power deposition for HL-LHC.</i>	114
6.15	Left: Temperature distribution in the cooling system obtained with the model including the cooling pipes. Right: Detail of the temperature distribution in the copper tube.	117

6.16	ANSYS Structural analysis results. Left: Von Mises stress distribution in cooling pipes, with detailed view at the end. Right: Christensen stress distribution in ferrite tube.	117
6.17	Ferrite rings after metallization with BAg-64 paste: a) Without prior outgassing; b) With prior outgassing (<i>Courtesy: F. Motschmann.</i>)	122
6.18	Assembly of ferrite ring and copper ring for the brazing test. (<i>Courtesy: F. Motschmann.</i>)	122
6.19	Assembly of ferrite ring and copper ring for the brazing test. <i>Courtesy: F. Motschmann.</i>	123
6.20	First brazing applied to the ferrite cylinder of final dimensions. <i>Courtesy: F. Motschmann.</i>	124
6.21	Second brazing applied to the ferrite cylinder of final dimensions. <i>Courtesy: F. Motschmann.</i>	124
6.22	Cooling system installed in the MKI magnet.	125

List of tables

2.1	Power loss for different beam screen configurations and LHC operation scenarios [36, 32].	18
2.2	Effect of the bake-out jackets on the ferrite yoke temperature, calculated for a power deposition of 250 W/m (30% above the predicted power for Run1)	22
2.3	Measured thermal emissivity of various components of the MKI with infrared thermography.	23
4.1	Properties of the components of the beam screen.	37
4.2	Total power in all the magnets calculated from measured beam coupling impedance, and Run2 beam parameters (<i>2808 bunches, 25ns spacing, 1.15E11ppb, 1ns bunch length</i>)	48
4.3	Summary of power distribution from different CST models.	53
4.4	Total power loss and the corresponding scaling factors applied to each power distribution model.	53
4.5	Effect of increasing the power by 25% upon the maximum predicted temperatures in actual and proposed PT100 locations.	58
4.6	Total power loss for Run1 and the corresponding correction factors applied to each power distribution model.	61
5.1	Maximum temperature of the first yoke for different configurations of a cooling system based on cold plates attached to the first yoke. <i>Model 3 of power deposition. Total power: 616 W</i>	88
6.1	Design guidelines deduced from thermal network model.	103
6.2	Hydraulic system parameters.	116
6.3	Calculation of the number of windings.	120

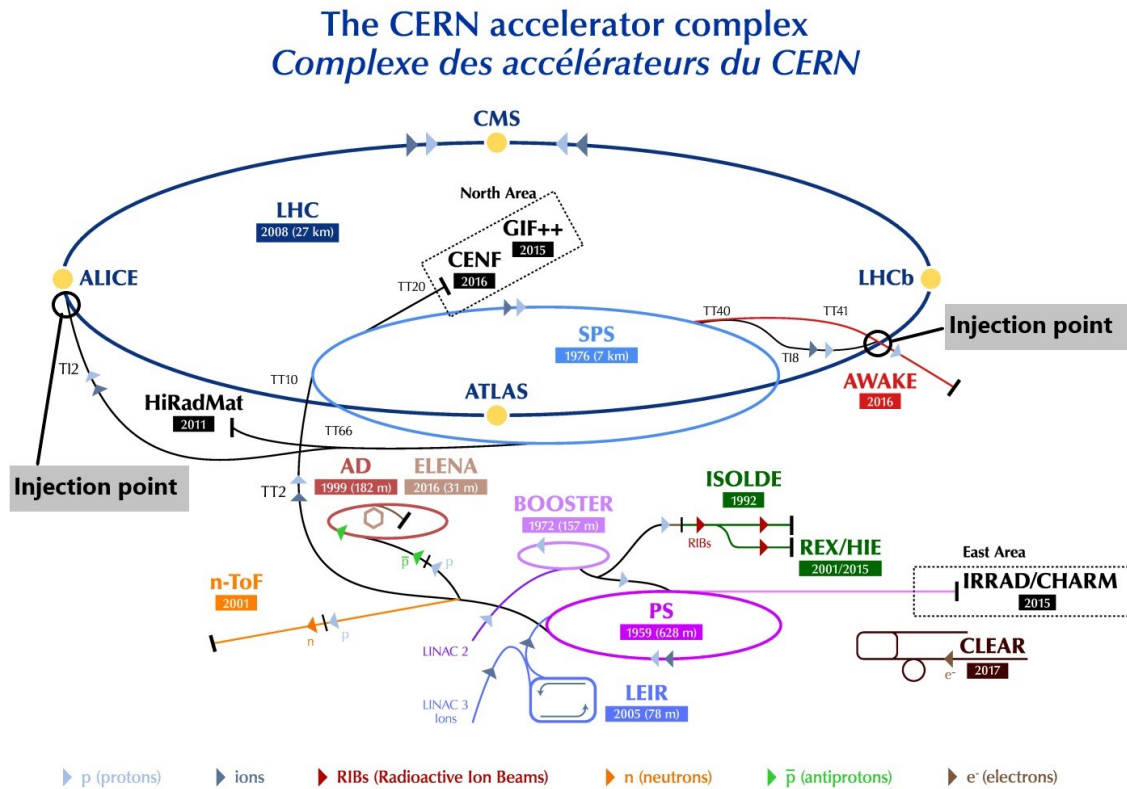
Chapter 1

Introduction

1.1 Context

At CERN, the European Organization for Nuclear Research, particle accelerators and detectors are used to study the basic constituents of matter. Since its foundation in 1954, Physicists and Engineers have unified their efforts towards increasing the discovery potential and pushing the limits of the energy frontier of the accelerators.

The flagship accelerator of CERN is the Large Hadron Collider (LHC), world famous for being the most powerful particle accelerator ever built. Two high-energy particle beams are accelerated to close to the speed of light before they are made to collide, in four points, where the detectors are located to analyze the products of the collisions. The experiments at the four points are called CMS, ALICE, LHCb and ATLAS (Fig. 1.1).



LHC - Large Hadron Collider // SPS - Super Proton Synchrotron // PS - Proton Synchrotron // AD - Antiproton Decelerator // CLEAR - CERN Linear Electron Accelerator for Research // AWAKE - Advanced WAKEfield Experiment // ISOLDE - Isotope Separator OnLine // REX/HIE - Radioactive Experiment/High Intensity and Energy ISOLDE // LEIR - Low Energy Ion Ring // LINAC - LINear ACcelerator // n-ToF - Neutrons Time Of Flight // HiRadMat - High-Radiation to Materials // CHARM - Cern High energy AcceleRator Mixed field facility // IRRAD - proton IRRADiation facility // GIF++ - Gamma Irradiation Facility // CENF - Cern Neutrino platForm

Fig. 1.1 CERN Accelerator Complex [55].

Following periods of operation (Runs), the LHC is stopped during Long Shutdowns (LS) and Technical Stops at the end of each year (YETS) for upgrades. The next major upgrade is the High Luminosity LHC (HL-LHC), aiming at achieving instantaneous luminosities a factor of five larger than the LHC nominal value. This parameter is directly related to the performance of particle colliders [45]. After five years of design study and R&D, and ten years of developments, prototyping, testing and implementation, the HL-LHC operation is expected to start in 2024 [16]. All of the collider's parameters and existing technologies must be adapted to this major project (Fig. 1.2). The studies presented in this thesis are within the context of the upgrades towards HL-LHC operation.

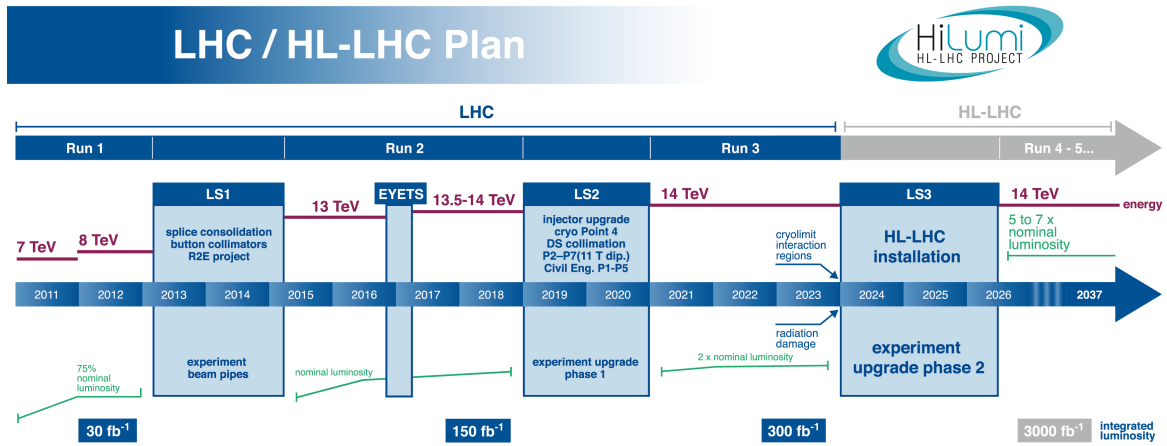


Fig. 1.2 LHC baseline plan showing the energy of the collisions (red) and luminosity (green) [16].

1.2 LHC Injection Kicker Magnets

Since an accelerator has a limited dynamic range, a chain of accelerators is needed to pre-accelerate the beam before it is finally injected into the LHC. All the accelerators are connected via transfer lines, and kicker magnets are used to extract/inject the beam out of/into each of the accelerators.

In the case of the LHC, the accelerator immediately before is the Super Proton Synchrotron (SPS), and they are interconnected by two transfer lines, one sending the beam to the LHC in a clockwise direction, and the other in an anticlockwise direction. At the end of both transfer lines, in the points where they meet the LHC (see "Injection point" in Fig. 1.1), Injection Kicker Magnets (MKIs) are installed to inject the beam onto the LHC's orbit [13]. Each set of MKIs is composed of four magnets as shown in Fig. 1.3, and these are the object of study of this thesis.



Fig. 1.3 Four MKI kicker magnets in the LHC tunnel.

The beam to be injected into the LHC approaches the first kicker magnet at an angle of approximately 0.8 mrad. The MKIs must deflect the beam into the accelerator's orbit by means of the Lorentz force as follows: When the beam is approaching the LHC, the MKI magnets are pulsed at a high voltage, and a current of approximately 5 kA passes through a High Voltage (HV) busbar and returns through a ground busbar, which are located in the aperture of the magnet, parallel to the beam direction. This results in a magnetic field as shown in Fig. 1.4. A U-core yoke of NiZn soft ferrite is used to guide the field lines, ensuring that the magnetic field is homogeneous to within $\pm 0.5\%$ over the specified good field region of the aperture of the magnet, so that all the particles experience the same force and subsequent deflection to within the $\pm 0.5\%$. This is necessary to maintain the focusing of the beam. When the moving charged particles pass through the aperture they experience the Lorentz force, and are therefore deflected at an angle which is dependent upon the momentum of the particles and the strength of the magnetic field integrated along the length of the kicker magnets.

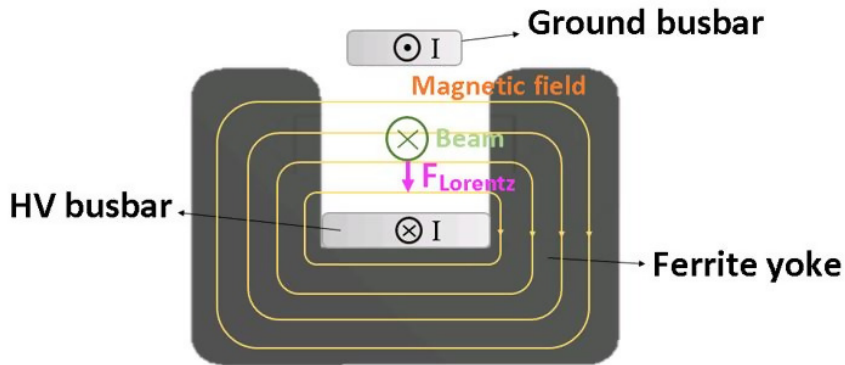


Fig. 1.4 Lorentz force acting on the injected beam (positively charged particles) passing through the aperture of the MKIs.

In order to meet the stringent pulse response requirements, the system is designed with a low impedance of 5 ohms and a carefully matched high bandwidth. An MKI system consists of a multi-cell pulse forming network (PFN) and a 33-cell travelling wave kicker magnet, connected by a matched transmission line and terminated by a matched resistor (TMR). The PFN design voltage is 60 kV and, allowing for overshoot, the magnet design voltage is 35 kV. The nominal PFN operating voltage is 54 kV [11].

There are four MKI systems at each injection point. In the following, the LHC beam injection process is described in more detail. To facilitate the understanding, a simplified scheme is shown in Fig. 1.5. It is worth mentioning that the beam is not continuous, but it is divided in groups of particles called bunches, which in turn are grouped forming batches. The injection is done batch by batch and the LHC can be filled with up to 12 batches.

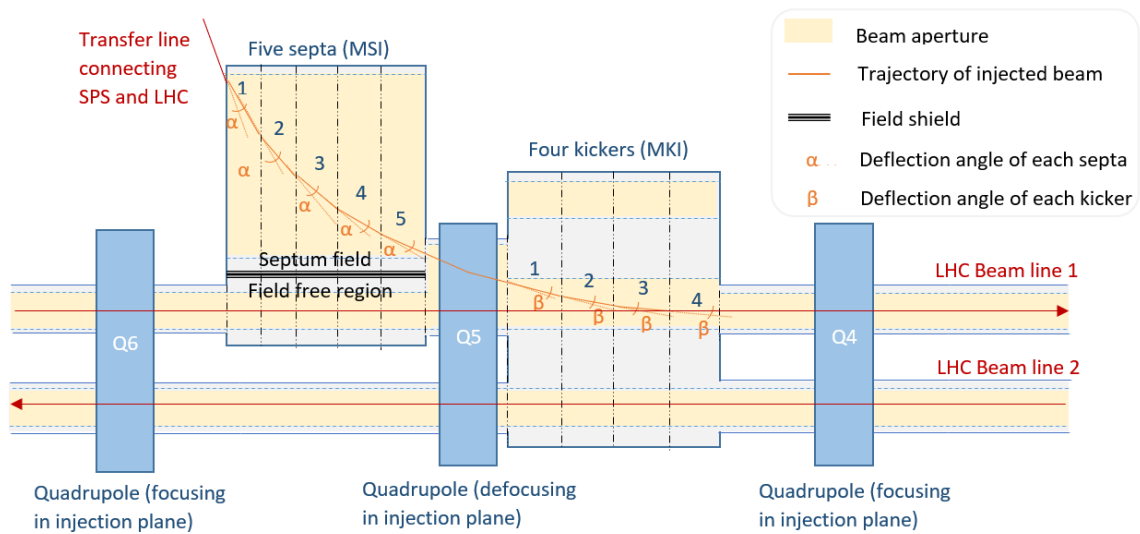


Fig. 1.5 Simplified schematic of LHC beam injection process for beam 1.

Two types of magnets are used in combination: five septa and four kickers. The former are characterized by dividing the space in two separated field regions, one where strong magnetic fields are present, and the other shielded from those fields. The beam coming from the SPS passes through the high field region of the septa and is deflected an angle α in each septum, while the beam circulating in the LHC passes through the no-field region without being deflected. The deflection of the incoming beam, provided by the septa, minimizes the required strength of the kicker magnets, which finally compensate the remaining angle, each one deflecting at an angle β . Note that in the kickers, the incoming beam and the one circulating in the same direction in the LHC, pass through the same aperture. For this reason, it is of key importance that the kickers magnetic field rises and falls while there is no beam circulating through them, that is within the time period between the circulating batches, and it must closely follow the current pulse with minimal distortion (see Fig. 1.6). If not, they will deflect the beam that is already in the LHC's orbit, leading to a deviation in the trajectory with the subsequent risk of introducing beam instabilities or even causing an impact with the other magnets. The septum and kicker are either side of a quadrupole (defocusing in the injection plane) which provides some of the required deflection and minimizes the required strength of the kicker magnet[13].

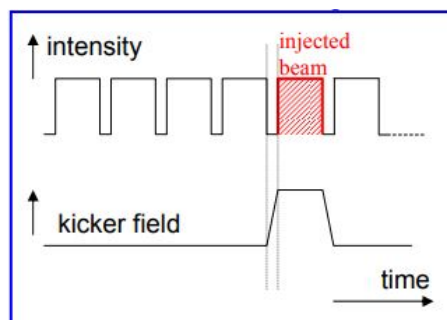


Fig. 1.6 Pulse in a kicker magnet.

It should be noted that the kickers have three apertures for the beam to pass through (see Fig. 1.7), only one of which (the central one) is associated with the injected beam and thus has a pulsed field. The two outer apertures are outside the ferrite yoke and are field free: one of them has counter rotating beam and the other is unused. The reason for having two outer apertures is that a symmetric configuration allows those magnets to be installed in both injection points (clockwise and anti-clockwise direction).

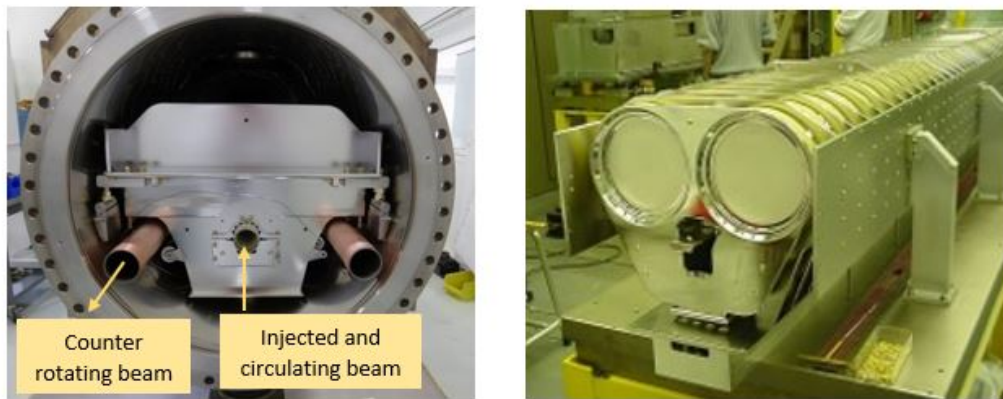


Fig. 1.7 Internal view of a MKI magnet. Detail of the apertures for the injected and circulating beams.

The MKI kicker magnets are installed inside tanks in ultra high vacuum conditions as this is a reliable dielectric. They are formed by 33 repeated cells, as shown in Fig 1.8, and the main components are indicated in Fig. 1.9. Each cell consists of the U-core ferrite yoke between two high voltage plates, and two ceramic capacitors between one of the HV plates in contact with the ferrite yoke and a plate connected to ground [13]. Fig. 1.9 also shows a ceramic tube, with screen conductors lodged in its inner wall, placed within the aperture of the magnet to reduce the electromagnetic interaction of the beam with the ferrite yokes and thus, reduce the beam induced heating [4]. The conductors, which provide a path for the image current of the beam, are directly connected to the beam pipe at one end whilst the other end of the conductors is capacitively coupled to the beam pipe in order to prevent a continuous (DC) path for longitudinal eddy currents and hence to preserve the fast field rise time of the magnet. At both ends of the magnet nine ferrite rings are installed to damp low-frequency resonances [36].

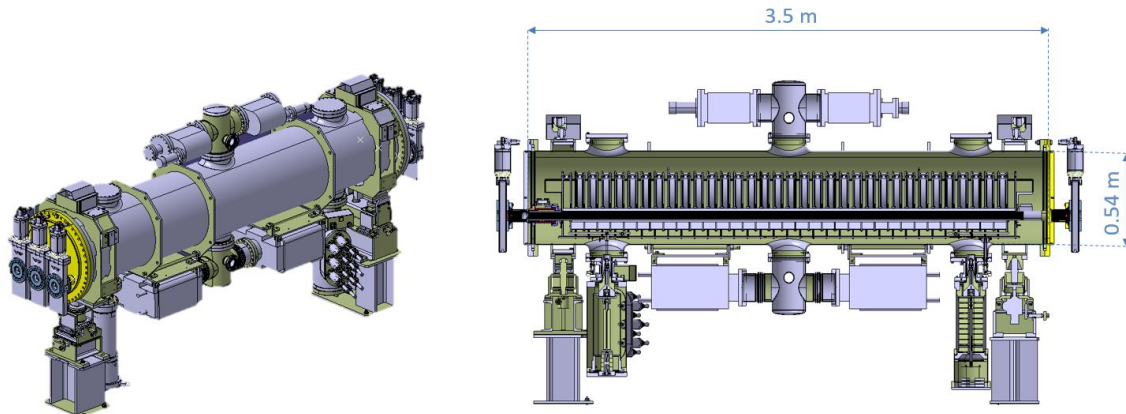


Fig. 1.8 CAD model of a MKI magnet.

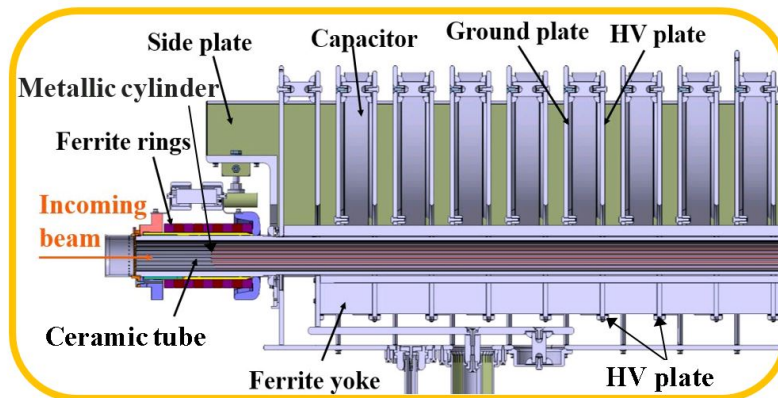


Fig. 1.9 Cross-section of CAD model of the upstream end of a MKI magnet.

Once the magnets are inserted inside the vacuum tank, they must follow a conditioning process before their final installation in the LHC. First, the complete magnet is baked out in an oven at 315°C tens of hours. This is required to achieve vacuum of 10^{-11} mbar when installed and in operation. Subsequently the kicker magnet is HV pulse conditioned. After that, and again to ensure that ultra high vacuum conditions can be reached, it is vented with dry nitrogen and finally vacuum valves, ion pumps and Penning gauges are installed. This is followed by the installation of the bake-out jackets, done outside the clean-room, to prevent dust being generated in a clean environment. Those jackets are used to re-bake the MKI before a final HV conditioning is done. Historically, they remain on the tank in case a bake-out of the MKI needs to be carried out in the LHC tunnel [4].

The problem of the MKIs is that, even though they are only required to be pulsed during injection, the beam keeps circulating through the central aperture during the LHC operation cycle, which can last for 35 hours, leading to beam induced heating of the ferrite and

consequently, to an increase of the temperature of the kicker magnets. This is caused by means of electromagnetic interaction of the beam with the magnet. If the Curie temperature of the ferrite yokes is exceeded, they temporarily lose their ferromagnetic properties and mis-kicking of the beam at the next injection might occur. This temperature is 125°C for ferrite type 8C11 [41] and CMD5005 [56], used in the ferrite yokes, and 200°C and 250°C for the ferrite types 4M2 and 4B3 [41], respectively, presently used for the ferrite rings.

During Run1 in 2011, the ferrite yoke in one kicker magnet reached the Curie temperature and LHC operation was paused to avoid mis-injection. Since then a campaign of beam coupling impedance [38, 32, 34, 80, 81] and thermal studies [67, 77, 78] was carried out to better understand both the electromagnetic interaction and the heat distribution within the magnets. Numerical models were developed to predict the heat loads and temperatures during different operation scenarios. As a result of these studies, upgrades were implemented to improve the screening of the beam, aiming at reducing the electromagnetic interaction and hence, the head load. Thanks to that, no heating issues occurred during Run2.

However, further measures must be taken as a significant increase of the heat load is expected in the next LHC period (HL-LHC) due to operation with higher intensity beams. A description of the evolution of the studies will be presented in this thesis, culminating with the conception and design of a cooling system to cope with the increased heat load, ensuring a safe operation with the temperature of the ferrites always below the Curie limit.

It must be highlighted that by the time this thesis started, the cooling methods implemented in similar systems were not applicable to the LHC kicker magnets, because the cooling power required was particularly high. This was due to the high intensity beams circulating in the LHC, the world's largest and most powerful particle accelerator, resulting in significant beam induced heating. Other distinctive feature of these magnets that made the installation of a cooling system specially challenging was the limitation of materials and cooling components that could be used inside these magnets due to the ultra high vacuum environment and the presence of high voltage components. Thus, any modification proposed should be carefully studied to avoid compromising their functionality.

1.3 Structure of the thesis

In the first chapter, a general introduction of the LHC injection kicker magnets has been presented, from the description of the injection process to the basic operating principles of these magnets. It is concluded with the presentation of the issues that will limit their operation, hence putting this thesis into context.

In the second chapter, the background of the project is presented. It contains a detailed explanation of the nature of the electromagnetic interaction between the beam and the magnet causing heating. The concepts that are necessary for the proper understanding of the problem and the investigated solutions are introduced. Besides, in order to provide context of the starting point of this thesis, a review of the measures that were implemented or studied previously is included as well.

The third chapter continues with the methodology that has been followed in this thesis. Chapter four is dedicated to the presentation of the tools that have been used to carry out the investigation. In particular, the models created for computational simulations are thoroughly described, emphasizing all the improvements made to the available ones.

The following chapters cover the whole process of finding a solution to the problem, starting from the calculation of temperatures in different LHC operation scenarios to assessing the cooling needs, and analyzing several alternatives to deal with the heating. Furthermore, the thermal studies done for each of the studied alternatives are reported to support the decisions made regarding its application. In some cases, the alternatives were directly discarded, in other cases, further investigations were carried out. Those studies culminate with the conception and design of a cooling system, thoroughly described in chapter six, where a complete description of each of the steps followed is provided.

In the last chapter, the conclusions are reported, discussing the highlights of the thesis and finishing with the steps that will be followed during the next months until the implementation of the prototype of the cooling system in one of the MKIs, to test its performance in-situ with LHC beam.

Chapter 2

Background

Heating of an accelerator component is caused by the interaction of the electromagnetic field of the circulating beam with its surroundings. A better understanding of this phenomena is key to understanding the measures that were taken to deal with the heating of the magnets. In the first section a basic introduction to the electromagnetic fields associated with ultra-relativistic particles is provided, describing their interaction with the vacuum chambers as they travel through an accelerator. Consequences related to these phenomena are as well discussed. In the second section, a literature review of the alternatives that were investigated prior to the start of this thesis are presented, to give an overview of the status of the project in the initial stages of the thesis, introducing as well the lines of research that were followed.

2.1 Electromagnetic interactions of charged particles with accelerators' components

The electric field lines associated with a charged particle at rest extend isotropically in all directions. As the particle is accelerated to close-to the speed of light (ultra-relativistic particle), the field lines experience a length contraction in the direction of motion as indicated in Fig.2.1 [46].

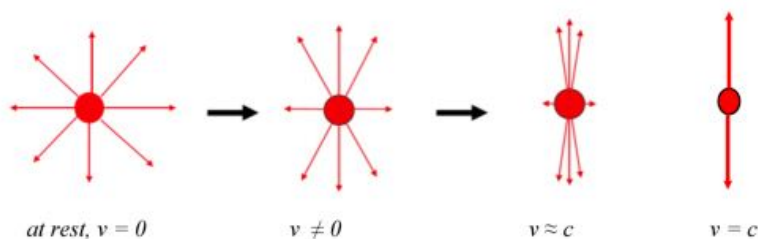


Fig. 2.1 Contraction of the electric field lines in ultra-relativistic particles [46].

When ultra-relativistic charged particles travel through a vacuum pipe, which is assumed to be smooth and made of a perfect conducting material, the electric field lines are perpendicular to the pipe. To cancel the electric fields outside the vacuum pipe, charges that oppose the current of the travelling particles are induced in the inner wall of the pipe [18]. They are known as image charges and they travel with the particle beam through the accelerator structures, creating a wall current as shown in Fig. 2.2.

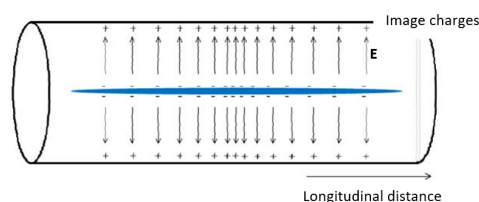


Fig. 2.2 Image charges induced in the walls of a vacuum pipe by a passing particle beam [39].

However, the accelerator components are sometimes made of resistive materials or present non-uniform geometries, which retard the image charges. In that case, a component of the electric field appears in the longitudinal direction of the wall inducing electromagnetic fields that act back on the circulating beam of particles. The field lines are distorted as shown in Fig. 2.3, and the fields that are left behind are called wakefields when they are expressed in the time domain. An equivalent quantity in the frequency domain is the beam coupling impedance, which is obtained by applying the Fourier transform to the wakefields. The impedance is a complex number and it has a transverse and a longitudinal component. The study of both is necessary as the transverse impedance can cause the deflection of the beam which leads to instabilities, whereas the longitudinal, apart from instabilities, causes energy loss of the particles and creates heating of the vacuum components [46]. However, in the context of this thesis, as it is mainly focused on the heating of the magnets, only the study of the longitudinal impedance will be of interest.

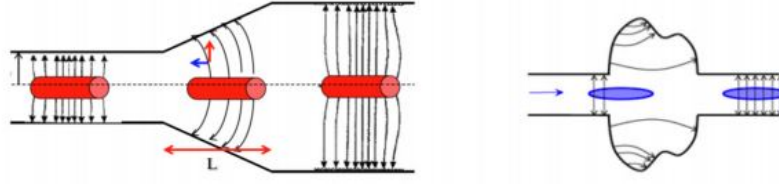


Fig. 2.3 Distorted field lines due to non-uniform geometries and resistive materials [46]

The power losses are calculated according to Eq. (4.3) [23], assuming a filling scheme of N equi-spaced, equi-populated, Gaussian bunches:

$$P_L = 2I_b^2 \sum_{n=0}^{\infty} |Y(\omega_n)|^2 \Re\{Z_L(\omega_n)\}, \quad (2.1)$$

where $I_b = MNef_0$ is the average beam current, being M the bunch intensity, N the number of bunches and f_0 the beam revolution frequency in the accelerator, $Y(\omega)$ is the Fourier transform of the normalised beam current and $\omega_n = n2\pi f_0$ its harmonic multiples. Finally, $\Re\{Z_L(\omega_n)\}$ is the real part of the longitudinal beam impedance.

To help better understand the implications of Eq. (2.1), a graphical example is used to support the explanation: In Fig. 2.4, the terms in the equation have been plotted separately showing its contribution to the calculation of the dissipated power. This plot corresponds to calculations done for the Target Dump for Injection Segmented (TDIS).

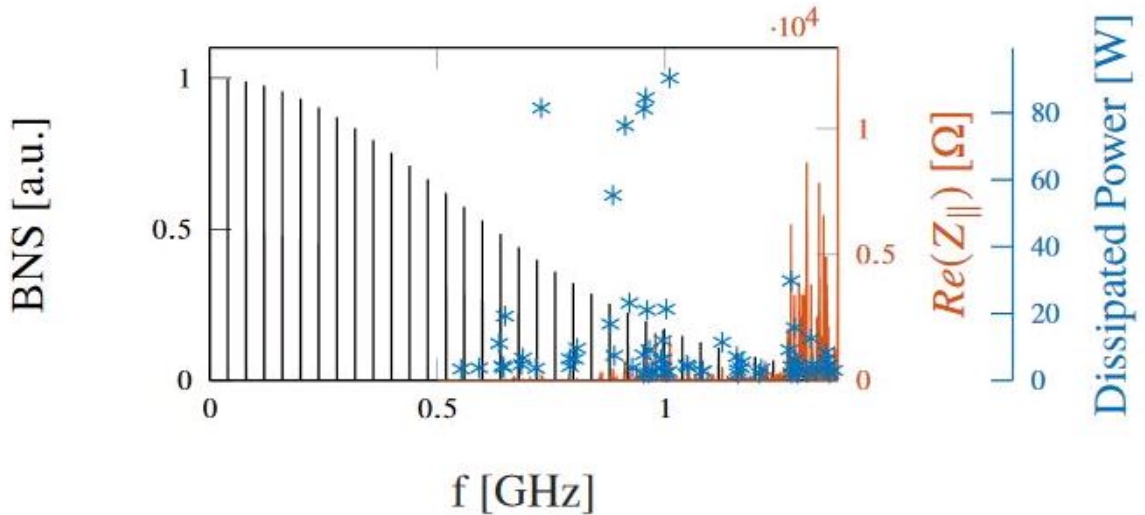


Fig. 2.4 Contribution of the HL-LHC beam normalized spectrum (BNS, in black) and the real part of the longitudinal impedance (in red) in the frequency domain to the calculation of the dissipated power in the TDIS (in blue) [72].

Before analyzing Fig. 2.4, it is worth clarifying that the beam is not continuous, but composed of particle bunches that circulate around the accelerator at a given revolution frequency. As a consequence, the beam spectrum, assuming equi-spaced, equi-populated Gaussian bunches, is plotted in the frequency domain as shown in Fig. 2.4: It is normalized to the low frequency harmonic components. It should be noted that the harmonics are predominantly due to the spacing between the bunches (25 ns).

When the beam spectrum and the real part of the longitudinal beam coupling impedance of the surrounding chamber have significant components at the same frequencies, there will be a strong coupling between them, with a corresponding power loss at each of those frequencies (blue markers). The sum of the power loss contributions, calculated at the different frequencies, will be the total power loss, P_L , indicated in Eq. (2.1).

From the above explanation it becomes clear that to reduce the power loss, it is not only important to reduce the value of the real part of the longitudinal impedance of the chamber at each frequency, but to shift the main part of its spectrum to higher frequencies where the beam harmonic lines do not have significant magnitude, hence reducing the beam induced power loss.

In the cases where the wakefields have been generated due to resistive materials, the impedance spectrum presents a broadband nature with significant components in a wide range of frequencies. In general, to reduce the beam induced power loss, the materials are shielded from the beam if possible. However, if the impedance has been generated due a cavity-like object, so that it presents a resonant behaviour with narrow bandwidth, the strategy to reduce the beam induced power loss is to shift the resonant frequencies to higher values. It must be noted that these are general guidelines, and each case needs specific study as these strategies are not always applicable.

Finally, it must be pointed out that the mechanism of beam induced heating of the ferromagnetic materials is a form of radiative heating. In particular, as the polar molecules of these materials have a magnetic dipole moment, they get aligned with the electromagnetic Radio Frequency (RF) fields generated due to the beam coupling impedance which oscillate within the vacuum chambers. The molecules rotate continuously by aligning with the oscillating fields, causing energy dissipation [63].

2.2 Literature review

Kicker magnets are in general a significant source of beam coupling impedance in the accelerator complex at CERN due to the proximity of very lossy materials to the beam. However, the MKIs, unlike most existing kicker magnets, were designed with impedance

reduction mechanisms in place, consisting of a beam screen in the MKI aperture to shield the ferrite yokes from the beam, hence reducing the beam coupling impedance. Originally, the beam screen consisted of conducting stripes painted inside a ceramic tube made of alumina. The conducting stripes provided a low resistance path for the image currents [5]. However, due to HV breakdowns, the painted stripes were substituted by 24 evenly distributed screen conductors inserted into open slots in the inner surface of the ceramic tube [6]. Even though the HV performance improved after this measure, discharges were still occurring during pulsing of the magnet [9]. Hence, it was decided not to include the 9 conductors closest to the HV busbar [33].

The benefits of including the beam screen with the conductors are shown in Fig. 2.5. Note that the impedance remains almost unaffected by the alumina tube (red curve). Indeed, the material was carefully selected so that it did not interact with the magnetic fields. Its only function was to support and provide electrical insulation to the screen conductors.

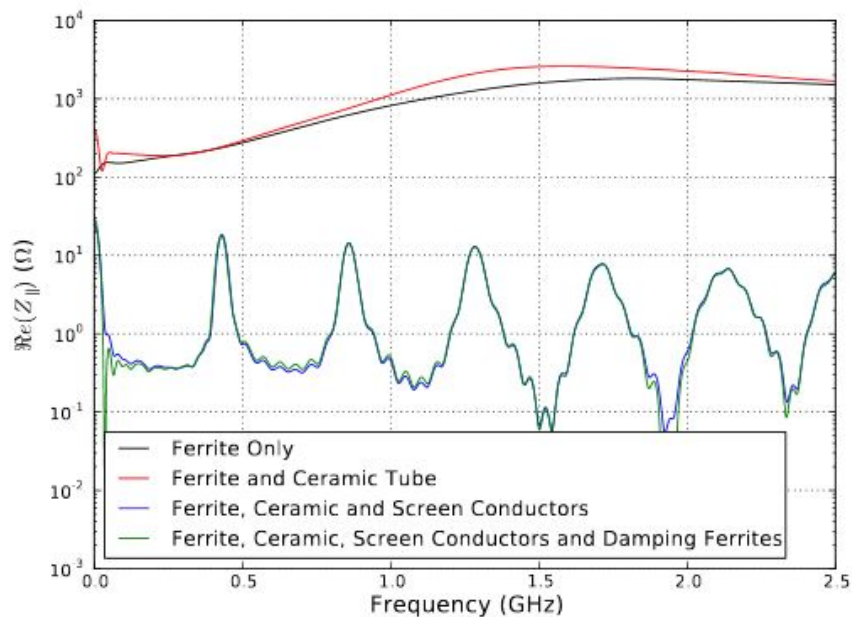


Fig. 2.5 Effect of the beam screen and the ceramic (alumina) tube on the real part of the longitudinal impedance of the MKIs.

At one end the screen conductors are connected together (Fig. 2.6) and this end is directly connected to the beam pipe. At the other end the conductors are not connected to one another (Fig. 2.7), and it is capacitively coupled to the beam pipe via an external metallization on the ceramic tube, in order to preserve the fast field rise time of the magnet. The screen conductors are staggered in length for HV reasons [4].

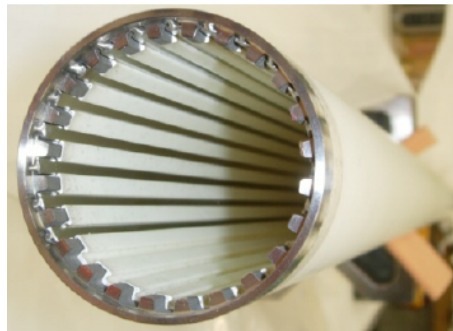


Fig. 2.6 Screen conductors connected to the beam pipe.

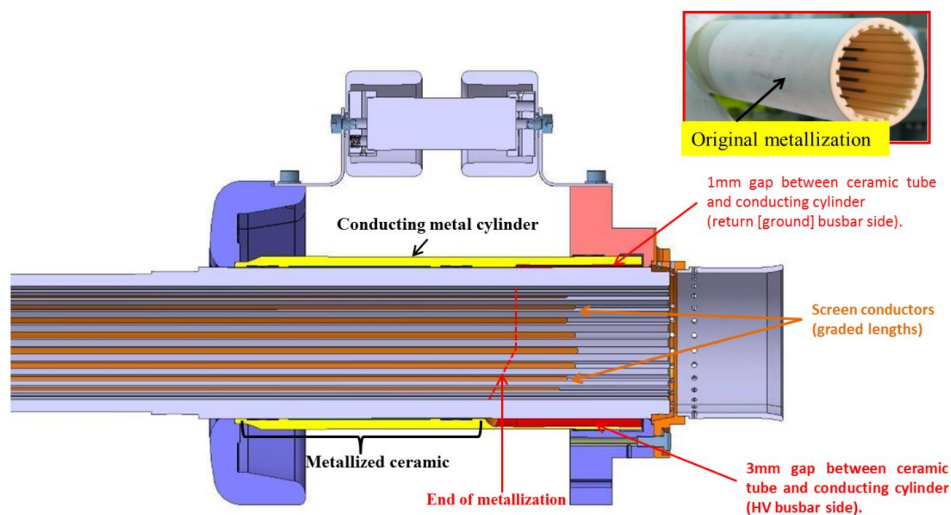


Fig. 2.7 Screen conductors at capacitively coupled end with metallization on the ceramic tube *Courtesy M. Barnes.*

During the first Run of the LHC, throughout 2011 and 2012, high temperatures were observed in one MKI, which was attributed to beam induced heating. The ferrite yoke of that MKI occasionally approached the Curie temperature during LHC operation, thereby necessitating waiting times of several hours for the ferrite to cool down before the next injection. Since then numerous studies were carried out to find a way to reduce the beam induced heating, and computational models were developed to better understand the electromagnetic and thermal behaviour of the MKIs to avoid a similar situation in the future LHC operation.

The first line of investigation consisted of finding ways to reduce the beam impedance by optimizing the design of the beam screen. Different alternatives were investigated with computational simulations using CST Particle Studio[®]. The impedance of a MKI with a beam screen with 15 conductors was measured for benchmarking. Good agreement was

found between measurements and predictions, indicating that the model was reliable for power loss estimates [38].

The validated numerical model was used to simulate beam screen configurations with different number of conductors: 15, 19 and 24. Results showed that increasing the number of conductors greatly reduced the impedance at all frequencies, with the best case being the configuration with the full complement of 24 screen conductors: Beam induced power deposition was reduced four times with respect to the case with 15 conductors, and 1.5 times with respect to 19 conductors [36], as shown in Fig. 2.8.

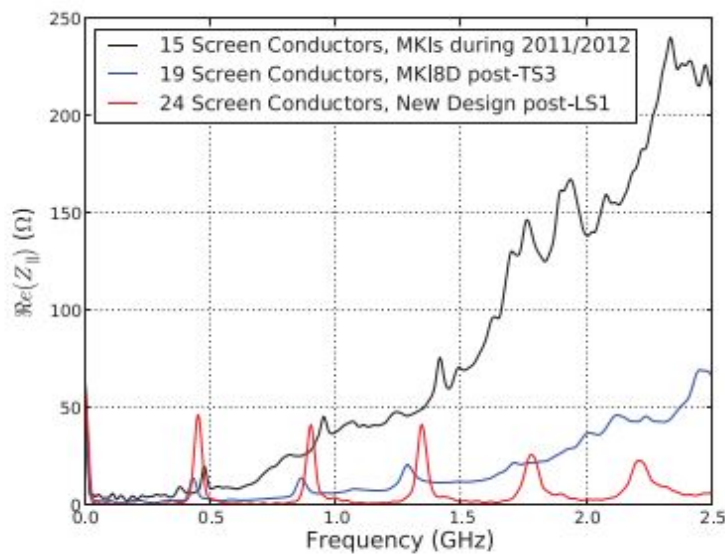


Fig. 2.8 CST results of the expected impedance for different beam screen configurations: with 12, 19 and 24 conductors.

However, as mentioned above, additional screen conductors presented higher risk of electrical breakdown during magnet pulsing. For this reason, the beam screen with 19 screen conductors was chosen for installation in a magnet to replace the MKI8D, which was the one where the Curie temperature was reached on several occasions. This beam screen with increased number of conductors also included some modifications in shape, at the capacitively coupled end, to reduce the likelihood of electrical breakdown [4]. After the implementation, during Technical Stop 3 (TS3) in September 2012, MKI8D showed the lowest temperature of all injection kickers during LHC operation [12].

Once the MKI8D was replaced, this magnet was opened and inspected to find possible causes that explained the high temperatures reached. It was found that the screen conductors were not straight but had a 90 degree twist over their length along the alumina tube. This left the ferrite yokes unshielded from the beam in the part where the conductors were twisted,

leading to an increased beam coupling impedance. In order to confirm this hypothesis, the longitudinal impedance of this non-conforming magnet was measured, resulting in 160 W/m in comparison to the 68 W/m obtained from the impedance measurements of other magnets without the twist. This value of 160 W/m was originally taken as a good indication of the power that should not be passed to avoid temperatures above the Curie point [32]. The calculation was based on the assumption of uniform power distribution along the length of the MKI ferrite yoke, which is now known not to be the case. The power was calculated assuming LHC beam parameters of Run1.

Once the successful performance of the upgraded MKI8D with 19 conductors was confirmed, investigations were focused on further reducing the high electric field at the capacitively coupled end of the screen conductors in order to allow the placement of the 24 conductors. The solution found consisted of removing the external metallization from the outside of the ceramic tube from a distance of 20 mm behind the end of the screen conductors and including a conducting metallic cylinder around the ceramic tube, leaving a vacuum gap of 1 to 3 mm between the metallic cylinder and the alumina tube, as shown in Fig. 2.7. This cylinder would be the new path for the beam image current [12]. Following HV breakdown tests, this upgraded beam screen was installed in all the MKI magnets during LS1. In the following, this upgraded design is going to be referred to as the post-LS1 design.

In order to assess the improvement of increasing the number of conductors from 15 to 24, and to determine if this would be enough to adequately reduce the beam induced heating for future LHC operation with high intensity beams, the expected power loss was calculated for both cases in different scenarios. Results are reported in Table 2.1.

Mode	Bunch separation [ns]	Number of particles per bunch [10^{11}]	Number of bunches	Bunch length [ns]	24 screen conductors [W/m]	15 screen conductors [W/m]
Pre-LS1	50	1.6	1380	1.2	20-35	68
Post-LS1	25	1.15	2808	1	34-52	117
HL-LHC	25	2.2	2808	1	125-191	432

Table 2.1 Power loss for different beam screen configurations and LHC operation scenarios [36, 32].

It can be seen that for post-LS1 operation no issues are expected, but for HL-LHC the expected power could be well above the initially assumed limit of 160 W/m. For this reason, studies to further reduce the beam coupling impedance continued with the efforts being focused on further understanding the source of the impedance. By comparing the curves of

the longitudinal impedance of the three cases mentioned above (beam screen with 15, 19 and 24 screen conductors, shown in Fig. 2.8) it can be appreciated that they are different in nature: the beam screen with 15 conductors showed a broadband impedance, which is characteristic of interactions due to materials properties, as described in the previous section. This indicates a poor screening, or the beam "seeing" the ferrite yoke. On the contrary, the beam screen with 24 conductors presents a strongly resonant-type impedance, whereas the case with 19 screen conductors showed a mixed impedance [37]. As it has been commented in the previous section, the recommended approach to reduce the beam coupling impedance in those cases that present a resonant behaviour consists of shifting the resonant frequencies to higher values whenever it is possible. To evaluate the feasibility of this approach, first it is necessary to understand the origin of the narrowband resonances [32]. For that, field monitors were placed in the CST simulation model to identify the areas where the wakefields were localized in the magnet. Results showed that they were concentrated in the region between the end of the screen conductors, at the capacitively coupled end, and the external metallic tube (see Fig. 2.7). These are $n\lambda/2$ resonances, where λ is the wavelength of the resonance and n an integer. The predicted resonant frequencies, f_{res} , are given by Eq. 2.3 :

$$f_{res} = \frac{nc}{\sqrt{\epsilon_r}2(L_{overlap} + \delta_{fringe})}, \quad (2.2)$$

where c is the speed of light, ϵ_r is the relative permittivity of the surrounding medium, $L_{overlap}$ is the length of the overlap between the screen conductors and the external metallic tube, and δ_{fringe} is a factor to take into account fringe fields, which are related to the thickness of the alumina tube as follows:

$$\delta_{fringe} = 1.25t_{tube}, \quad (2.3)$$

with t_{tube} being the thickness of the alumina tube.

From Eq. 2.3, it can be deduced that for shifting the resonant frequencies to higher values, the overlap length must be decreased. Several simulations were performed with different overlap lengths and results, shown in Fig. 2.9, confirmed this hypothesis. In order to obtain the optimal overlap length, further investigations were required [32].

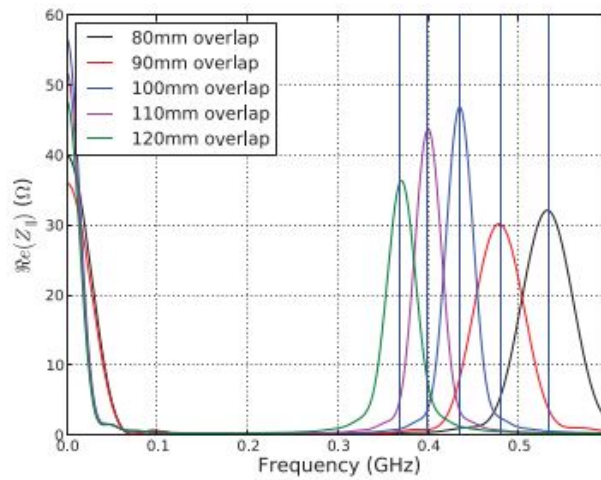


Fig. 2.9 Real longitudinal impedance of the MKIs for different overlap lengths.

In parallel, alternatives for improving the heat transfer out of the magnet yokes were investigated in order to cope with the expected power deposition of 200 W/m for HL-LHC operation (see Table 2.1). Thermal analyses were performed using ANSYS[®] Mechanical[™]. The initial model consisted of a 2D cross-section of the MKI magnet as shown in Fig. 2.10. Note that at the time a 2D model was considered adequate as the beam induced power deposition was assumed to be uniform along the length of the ferrite yoke.

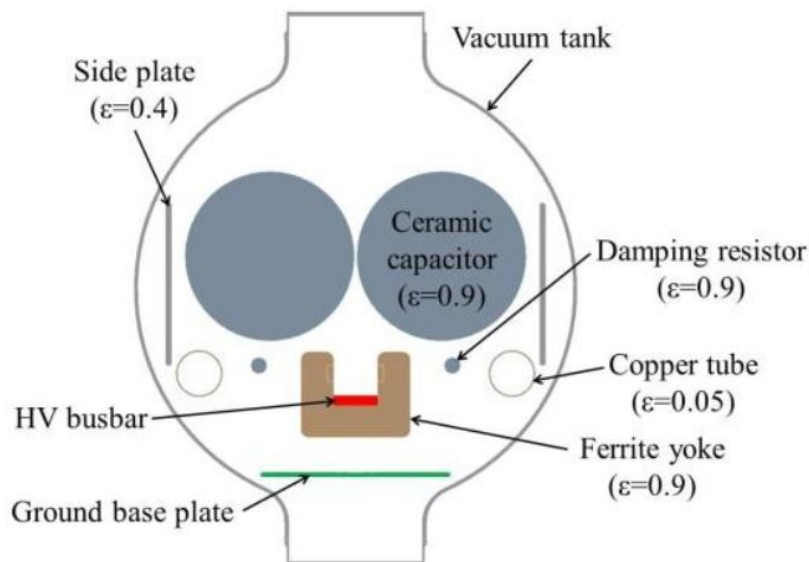


Fig. 2.10 Initial 2D model for thermal simulations with ANSYS[®] Mechanical[™]

This model was a very simplified representation of reality. Given the fact that it is a 2D section, the heat conducted to the HV plates which are in contact with the yokes (see Fig. 1.9) was not considered. Besides, the bake-out jackets that surround the tanks were not included in the model. However, as they isolate thermally the tanks, their effect upon the temperature of the ferrite yokes cannot be neglected. Hence, an equivalent convection coefficient which accounts for their contribution was defined in the external surface of the vacuum tank. For estimating the value, the thermal resistance of the jackets was measured in the lab, resulting in an equivalent convection coefficient between $1.9\text{ W}/(\text{m}^2 \cdot \text{K})$ and $2.9\text{ W}/(\text{m}^2 \cdot \text{K})$. As a pessimistic approach, $1.9\text{ W}/(\text{m}^2 \cdot \text{K})$ was the implemented value [14].

Thermal analyses were performed to predict the temperatures for different LHC operation scenarios and to understand which were the main parameters contributing to the increase of the temperature of the ferrite yokes. Steady-state simulations for a power deposition of $250\text{ W}/\text{m}$ (30% above the $191\text{ W}/\text{m}$ predicted power for the worst-case magnet for HL-LHC operation as a safety margin, see Table 2.1) showed a ferrite yoke temperature of 250°C , meaning that improved heat transfer was necessary to reduce it below the Curie point (125°C). Hence, several alternatives were investigated:

- *Use a ferrite with higher Curie temperature:*

One of the first proposals consisted of changing the type of ferrite with one of higher Curie temperature. However, a higher temperature of the ferrite results in poorer vacuum performance due to an increased outgassing rate, which could result in an increased HV breakdown rate in the magnet. For this reason, this option was not further considered [9].

- *Remove bake-out jackets:*

The possibility of removing the bake-out jackets was also considered. Its impact on the reached temperatures was assessed by comparing the results of two simulations with different values of the convection coefficient, representing the following cases [14]:

- Bake-out jackets installed: As previously commented, to simulate the effect of having the bake-out jackets installed, an equivalent value of the convection coefficient of $1.9\text{ W}/(\text{m}^2 \cdot \text{K})$ was estimated from measurements of the thermal resistance of the bake-out jackets.
- No bake-out jackets: In this case, the convection coefficient was assumed to be the one determined by the air natural convection in the LHC tunnel, estimated as $7\text{ W}/(\text{m}^2 \cdot \text{K})$.

	With jackets	Without jackets
Convection coefficient [$W/(m^2 \cdot K)$]	1.9	7
Maximum temperature [$^{\circ}C$]	250	233

Table 2.2 Effect of the bake-out jackets on the ferrite yoke temperature, calculated for a power deposition of 250 W/m (30% above the predicted power for Run1)

The results are summarized in Table 2.2. According to that, by removing the jackets, the temperature rise in the yokes is reduced by 8%. However, they are difficult to remove and practically impossible to re-install properly in the LHC tunnel due to space constraints. Without the jackets, it would be difficult to perform a proper bake-out in-situ, if required. For this reason, it was decided to only remove the bake-out jackets, during Run1, for the two hottest magnets (MKI8B and MKI8D before its change during TS3) and the measured temperatures were reduced approximately by 15% [14]. This discrepancy between predictions and measurements might be explained by the simplified way in which the effect of the bake-out jackets was introduced in the model.

- *Increase thermal emissivity of the internal surface of the vacuum tank:*

Another considered alternative was to improve the radiative heat transfer inside the tanks by increasing the thermal emissivity of their internal surface. This was thought to improve considerably the heat transfer because originally, the tanks were electro-polished (see Fig. 2.11), leading to a low thermal emissivity. This was highly limiting the absorption of heat. Note that the main mechanisms of heat transfer inside the tanks were conduction and radiation as they operate under ultra high vacuum, so convection was negligible.

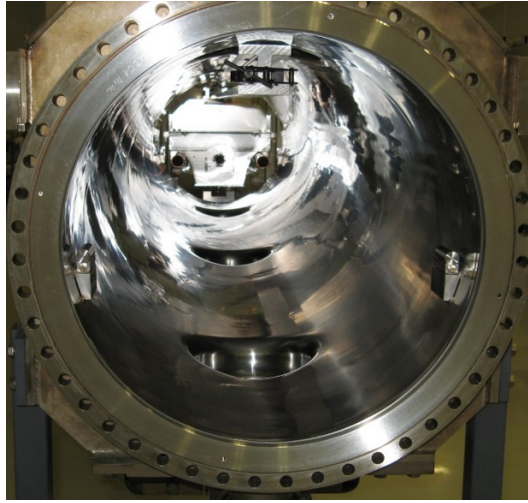


Fig. 2.11 Internal surface of vacuum tanks.

In the 2D analysis, all the heat generated in the yokes is assumed to be transferred to the adjacent components by thermal radiation. The role of heat conduction is negligible as the contact between the yokes and the other components is not modeled. Thus, defining correctly the thermal emissivity of all the components is key for the accuracy of the model. Measurements were made for various components of the MKI using an infra-red (IR) camera with a specified spectral range of $7.5 - 13 \mu m$ [9]. The results can be found in Table 2.3.

Component	Material	Measured thermal emissivity
Yoke	Ferrite	0.92
Capacitors	Alumina 96%	0.88
Beam screen	Alumina 99%	0.94-0.97
Metallic plates	SS304L	0.41-0.49

Table 2.3 Measured thermal emissivity of various components of the MKI with infrared thermography.

However, the emissivity measurements on the interior of the MKI vacuum tanks were particularly difficult to make because of the restricted access, the concave shape and the poor thermal conductivity. A method to measure the total hemispherical emissivity of the vacuum tank was developed based on a calorimetric technique. Details can be found in [7], with measured values in different tanks varying from 0.12 to 0.15.

Simulations were done for different values of the thermal emissivity of the vacuum tanks, confirming that increasing its value had a great benefit, helping not only to de-

crease the maximum temperature of the yoke, but also to reduce the cooling times [14]. By increasing the emissivity of the bottom half of the inside of the tank to 0.6 and increasing the value of the convection coefficient to $25 \text{ W}/(\text{m}^2 \cdot \text{K})$, which could be achieved installing forced air cooling, the calculated ferrite yoke temperature was reduced from 250 to 150°C for the power deposition of 250 W/m (20% above the predicted power for Run1). Those measures, combined with minimizing the surface of the side and ground plates that are located in the surroundings of the yokes (see Fig. 2.10), reduced the predicted ferrite temperature to 135°C [7].

With such results, the next step was to find a suitable method for increasing the thermal emissivity of the vacuum tanks, which was challenging due to their dimensions and shape, and the requirements imposed by the vacuum compatibility and HV performance. Some methods were directly discarded due to these constraints. In the end, ion bombardment in an atmosphere of argon and oxygen at Bodycote was the method initially chosen. This technique was first applied to small stainless steel (SS304L) pieces for testing the vacuum compatibility of the treatment and measuring the thermal emissivity. They showed the process to be vacuum compatible and had a measured emissivity of up to 0.6 [14]. Given the successful results, this technique was applied to the inner surface of some of the vacuum tanks. However, the emissivity of the treated tanks was measured with the calorimetric technique and it was in the range of 0.13-0.18, not a remarkable improvement with respect to the non-treated tanks (0.06-0.13) [14]. One of the possible causes that could explain these disappointing results was the temperature of the tanks being limited to 380°C during the treatment, to avoid damage to welds and vacuum flanges. Hence, this technique was discarded and other treatments were further investigated, such as carbon coating: tests on samples of SS304L showed an increased emissivity to over 0.6 with a carbon coating of 2.5 μm thickness [7].

The status of the project at the beginning of this thesis in 2015, during LS1, can be summed up as follows:

All the MKIs were upgraded with beam screens including 24 screen conductors. With this measure, no heating issues were expected during the next period of LHC operation (Run2). However, according to predictions the temperature of the ferrite yokes would be well above the Curie point for HL-LHC operation. Two parallel lines of investigations were followed to cope with the high power expected. On the one hand, beam impedance studies were ongoing to investigate how to further reduce the beam coupling impedance of the magnets. The main focus was the optimization of the overlap length that determined the resonant frequencies of the impedance. On the other hand, several methods to improve the heat

transfer were investigated. As none of these methods alone reduced the temperature of the ferrite yoke enough, a combination of them was under study and consisted of increasing the thermal emissivity of the vacuum tanks (carbon coating was under investigation), removing the bake-out jackets, implementing forced air convection outside the tanks and minimizing the surface area of adjacent components that were acting as radiation shields between the yokes and the tank. An active cooling system was not considered at that time given the fatal consequences of a liquid leakage in the UHV tanks and the difficulty of cooling 33 ferrite yokes, which are all pulsed to HV, making the installation very challenging. Further investigation was needed to implement the mentioned measures and find alternatives for reducing the yoke temperature below the Curie point.

Chapter 3

Methodology

In this chapter the methodology that has been followed for developing the thesis will be presented. A scheme is shown in Fig. 3.1, which compiles the main steps taken in chronological order. Following the arrows, it can be seen that iterations might have been necessary at different stages, depending on the results of the studies. Each of the points will be further explained below:

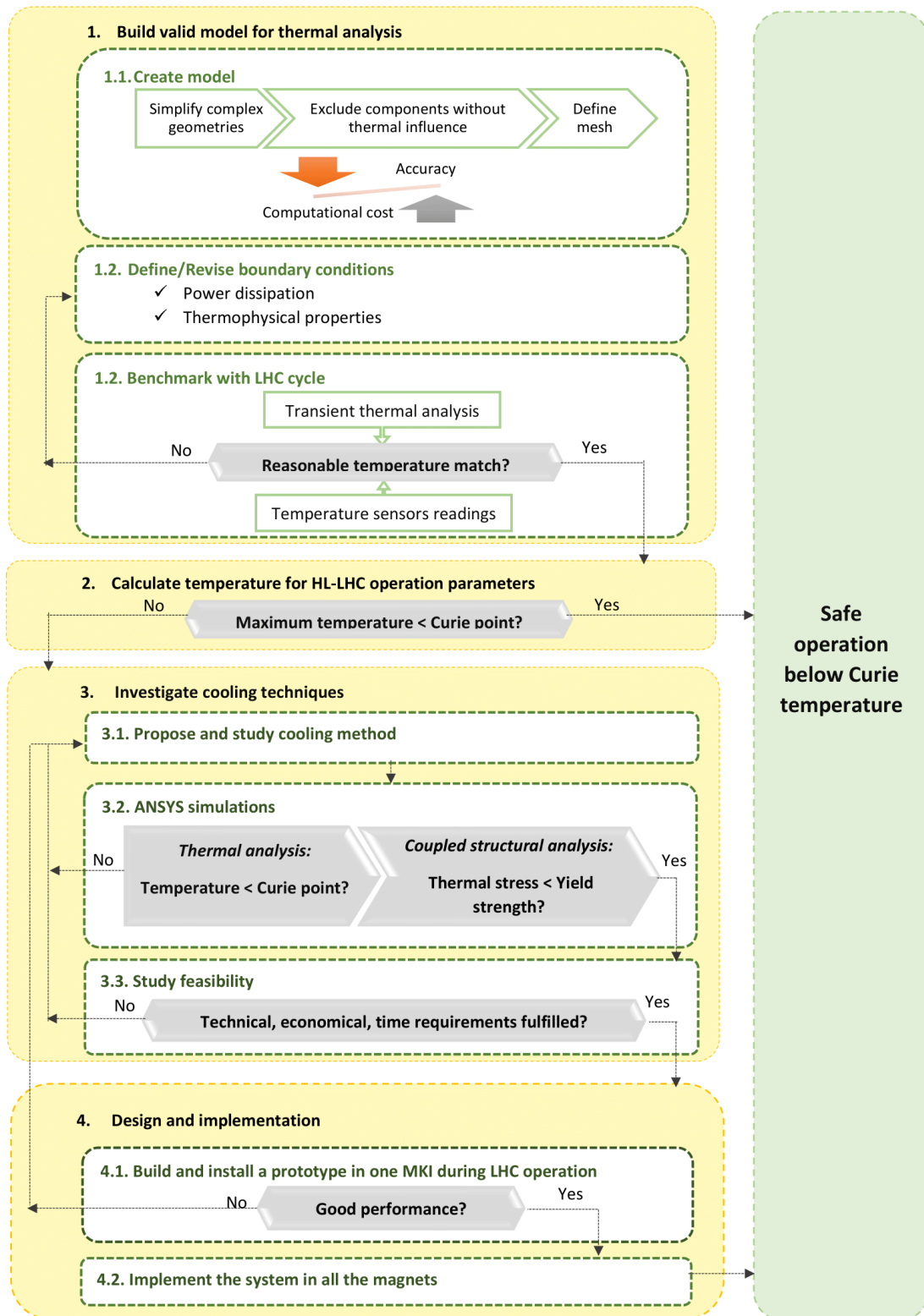


Fig. 3.1 Methodology.

1. Build a valid model for thermal analysis:

This is the first and most important step, as the veracity of the results will depend on the quality of the model created. For this reason, the models must be validated by simulating an LHC operating cycle and comparing the predicted temperatures with the ones measured in situ with PT100 sensors. If they are not in good agreement, the power dissipation and/or the ANSYS model must be revised. The mismatch could be caused by an over-simplification of the geometry, a non-precise definition of the boundary conditions or inaccurate power dissipation calculations. Experience at CERN shows that the latter are potentially a major source of error between measurements and predictions, as they are also obtained by means of computational models with the implicit uncertainties.

2. Calculate temperature for HL-LHC operation parameters:

Once the model has been validated, an analysis is performed for the heat loads expected under different LHC operating conditions to predict the maximum temperatures reached in the magnets. The motivation is to determine whether for future LHC operation, with higher intensity beams, the heat loads will be sufficient to cause an increase on the temperature of the magnets above their Curie point. If that is the case, further measures to cope with the overheating must be studied.

3. Investigate cooling techniques:

In order to determine if a proposed alternative for cooling the magnets is efficient, it is analyzed using the thermal model already created. The corresponding changes must be included in the model to properly assess its influence upon the thermal behaviour of the magnet. If the results predict temperatures below the Curie point, a coupled thermo-structural simulation must be performed to ensure that the thermal stresses generated are below the yield strength of the ferrite. This step is key as the ferrite is a brittle material, and low stress levels might lead to cracking of the yoke. Only then, it can be considered a potential solution, and its feasibility is further evaluated taking into account different aspects:

- *Technical:* First of all, it must be studied if the proposed method can be implemented considering the stringent requirements imposed by the LHC operating conditions. In particular, the main constraints are the available space in the vacuum tank and the ultra high vacuum environment, which greatly complicates the installation of a liquid cooling system, limiting also the materials that can be used to avoid a degradation of the vacuum performance. The presence of HV elements inside the tanks must be accounted during the material selection too.

Besides, given the brittleness of the ferrite, structural analysis might be necessary in case of installing components in direct contact with the yokes and rings. Even relatively low thermal stresses can lead to cracking of the ferrite if the systems are not properly designed.

- *Economical*: Even though some methods might be promising, the costs must be assessed before proceeding further with the investigation. The alternatives that imply high costs should be only considered if it is justified that they are the only solution available in terms of safe and reliable operation.
- *Time*: It must be taken into consideration that a solution must be provided before the HL-LHC operation starts, when heating issues are expected. Some methods might be promising but it is important to ensure that they will be applicable to the twelve MKI magnets by the time needed.

4. Design and implementation:

After demonstrating that a particular power dissipation and cooling method would maintain the temperature of the ferrite yokes and rings below their Curie points, a design campaign will follow. In order to test the performance of the system with beam under real conditions, a full scale prototype will be built and installed in the LHC while the operation is not critical for the temperature of the MKI magnets. If the prototype performs as expected, and no issues are encountered during operation, the system will be implemented in all the magnets, ensuring that the LHC operation is safe even when operating with high intensity beam.

In addition to the above cooling studies, alternative beam screen designs were being considered in parallel by colleagues. Thus good collaboration with these colleagues was important to ensure that the thermal studies included the predicted power deposition and the beam impedance designs considered thermal and mechanical constraints. As a result of this iterative process, the power deposition considered, and its distribution, changed throughout the studies of the thesis.

Chapter 4

Thermal modelling of the MKI magnets

This chapter discusses the modelling for the thermal aspects of the MKI kicker magnets. It starts by introducing the ANSYS software chosen for the simulations, and discusses several important settings for achieving accurate predictions in a reasonable amount of time. Subsequently the chapter considers boundary conditions, processes such as convection and the nature of the beam induced power deposition in the various regions of the MKI. Several different power distribution models are presented and predictions given and compared with temperature measurements, from the MKIs, made during operation of the LHC. Discrepancies between total power deposition resulting from CST predictions and lab based measurements are mentioned. In addition, discrepancies between ANSYS thermal predictions and temperatures measured during LHC operation, resulting from unknowns in the power deposition, are described and conclusions drawn regarding appropriate scaling factors for each model. It is concluded that the latest CST model is the most accurate and does not require any scaling factor in order that the predicted temperatures match well with those measured.

4.1 Analysis tools

In this section the procedure followed for creating an adequate model for thermal analysis, based on finite elements in ANSYS[®] Mechanical[™], is described in detail. The steps that have been followed for setting up the simulations can be divided as follows:

1. Build the geometry.
2. Create and optimize the mesh.
3. Define the boundary conditions.

A thorough description of each of the above-mentioned steps is presented hereunder.

4.1.1 Build the geometry

The first step is the creation of the geometry. On the one hand, the model should represent faithfully the reality, and for that it is important to include all the relevant details. On the other hand, a very complex geometry requires large computational resources, leading to long simulation times. An ideal model is one that presents a good compromise. The different steps that have been followed for the creation of the model are presented below.

Type of analysis: 2D or 3D

The first question raised when building the model for thermal analysis is whether a two-dimensional model can represent realistically the heat transfer processes, or a more complex 3D model must be created.

The advantage of the two-dimensional analysis is that it requires less computational resources. However, it is only applicable for models and environments that involve negligible effects from a third dimension, which is not the case for the MKIs. In this particular case, a 2D analysis would not provide a realistic representation due to the following:

- When the cross-section of a body is modelled in 2D, the software considers that it is infinite and constant in the perpendicular direction. This is only realistic in the case of bodies where the effect of the boundary conditions at both ends is negligible at the location of the section of interest. Hence, the dimensions in the perpendicular direction must be sufficiently large in comparison to the ones of the cross-section. In the case of the MKIs, the vacuum tanks have a length approximately 5.5 times larger than the diameter.

However, they do not fulfill the other necessary condition of having constant geometry along the longitudinal axis, but it varies periodically. In particular, an MKI is composed of 33 repeated cells as described in Chapter 1 (see Fig. 1.8 and Fig. 1.9). Due to this periodic structure, it could be enough by modelling just one cell, but this simplification would only be valid if the power generated in each of the cells was equal and uniformly distributed, and end effects are negligible.

- A 2D analysis considers that all the boundary conditions that define the thermal model are constant along the direction perpendicular to the cross-section. In the case of the MKIs, that implies that the power deposition should be equal in each of the cells along the beam direction, which was thought to be the case in the early stages of the

investigation. However, as the beam coupling impedance studies progressed, and based on temperature measurements on MKIs installed in the LHC, it was found that not only the power was mostly concentrated in the first yokes located at the entrance of the magnet, but also a non-negligible part of it was generated in the ferrite rings.

In conclusion, in the initial stages of the project the thermal model consisted of a 2D cross section of the magnet as it has been described in Chapter 2 (see Fig 2.10). However, for the reasons mentioned above, it was decided to develop a 3D model in order to have a more realistic representation of the heat transfer within the magnets.

Import and simplify the geometry

The MKIs are composed of a large number of components with complex geometries. For this reason, powerful Computer Aided Design (CAD) tools were used to create the 3D model. In particular, Catia V5 from Dassault Systems[®] was the one used as it is the official 3D CAD/CAM system supported at CERN. The complete model can be seen in Fig. 1.8.

Once created, the CAD model was imported into ANSYS[®] DesignModeler[™], where the geometry had to be simplified and cleaned-up in preparation for the analyses.

The simplification of the geometry is a key step for helping to improve the overall mesh quality and to reduce computational resources. This is of great interest in the case of the MKIs due to the complexity of the analysis, which leads to very expensive simulations regarding computational time and resources. This is mainly due to the highly nonlinear nature of the analyses, as the heat transfer processes are generally dominated by thermal radiation and due to the temperature dependent properties of the materials.

Several measures have been taken for simplifying the geometry, which are presented in detail:

- **Number of cells**

Although the MKIs are composed of a periodic structure of 33 cells, modeling a single cell would not be a faithful representation of reality because the power deposited in each of the cells is different. Indeed, according to CST calculations, it is mostly concentrated in the ferrite components at the entrance of the magnet: the ferrite rings and the first two ferrite yokes. However, from the 3rd to the 33rd ferrite yokes, the power deposition is close-to-uniform and of relatively low magnitude, as shown in Fig. 4.1. The power loss, averaged for a complete MKI, is $52 \text{ W}/m$.

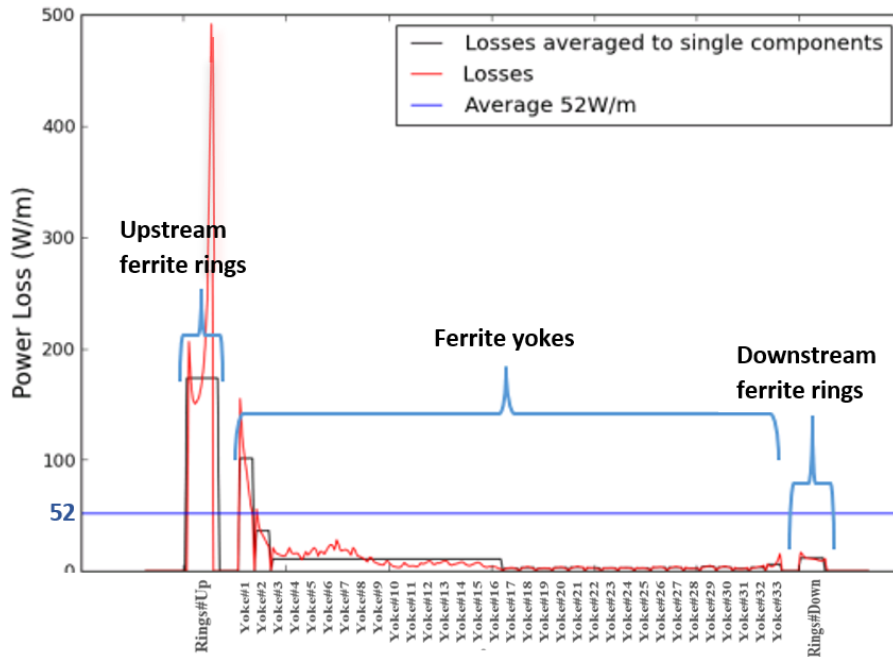


Fig. 4.1 Power distribution for Run2 nominal parameters, averaged per group of components with similar power deposition *Courtesy: H. Day*.

Hence, given the close-to-uniform power distribution in the majority of the magnet, it is not necessary to model the 33 cells, but only the first ones, up to the one from which the heat transfer between the adjacent cells can be considered adiabatic and the temperature difference is negligible. In order to determine where that happens, 3D simulations with up to 16 cells were performed, defining adiabatic conditions at the end of the last cell. Results showed a temperature difference between the 10th and the 11th ferrite yokes of less than 2%. Furthermore, the temperature drop between consecutive yokes was even further reduced in the next cells. Fig. 4.2 shows a comparison of the results obtained with the model of 16 and 10 cells. As the predicted temperatures are very similar, it can be concluded that 10 cells are sufficient for the 3D model.

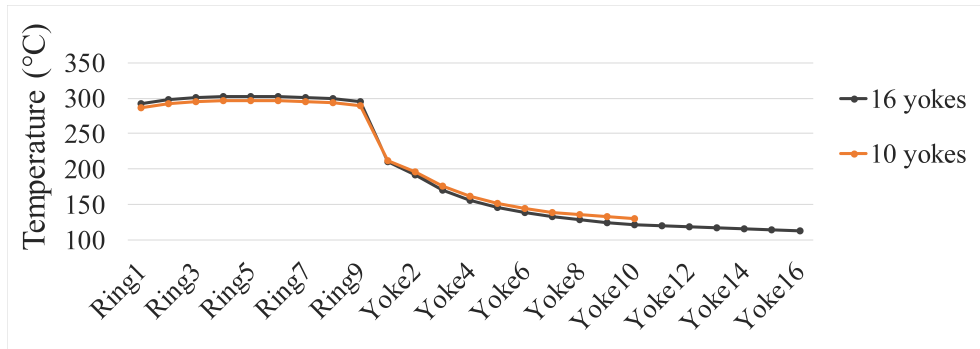


Fig. 4.2 Comparison of results with a model of 16 cells and a model with 10 cells.

- **Symmetry**

The MKIs have side-to-side symmetry, so only half of the model is included as shown in Fig. 4.9.

- **Identification of problematic components**

Some components presented complex geometries that were complicating the mesh generation. Modifications were carried out to simplify their geometries without losing accuracy in the results.

Beam screen:

The geometry of the beam screen is particularly complex due to the shape of the slots for inserting the conductors. Details of their geometry are shown in Fig. 4.3.

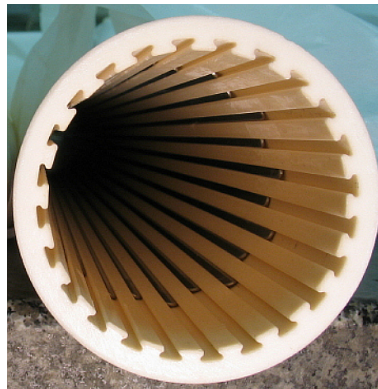


Fig. 4.3 Slots for screen conductors in the beam screen.

The presence of the slots complicates the mesh generation, making it necessary to use a high number of elements. For this reason, it is of particular interest to avoid including the slots and just modeling the beam screen as a tube. This simplification

must be first validated by assessing the influence of the screen conductors upon the heat transfer along the alumina tube. To do so, different simulations were performed to study modelling alternatives: The corresponding cross-sections of the studied models are shown in Table 4.1. All of them consisted of one meter long alumina tube with a heat load of 100 W applied at one end, radiating to the ambient at 22°C. The difference between them was the way in which the conductors were or not included in the model. The corresponding thermal emissivities and conductivities of both components are indicated in Table 4.1.





				
Alumina tube	Tube with insertion slots Volume: 8,94e-04 m ³ Ext. radius: 28 mm	Tube with insertion slots Volume: 8,94e-04 m ³ Ext. radius: 28 mm	Tube Volume: 8,94e-04 m ³ Ext. radius: 28 mm Int. radius: 22.4 mm	Tube Volume: 8,94E-04 m ³ Ext. radius: 28 mm Int. radius: 22.35 mm
Screen conductors	Rectangular wires Volume: 7,92E-05 m ³	Not included	Tube Volume: 7,92E-5 m ³ Ext. radius: 22.4mm Int. radius: 21.8 mm	Not included
Maximum temperature	349.5°C	334.1°C	348.6°C	354°C

Fig. 4.4 Modelling alternatives of the beam screen. Model *a*: Reference. Models *b*, *c*, *d*: Proposed simplifications.

On the one hand, the influence of the screen conductors upon the temperatures can be assessed by comparing the models of the alumina tube with and without them (models *a* and *b*). Results show a temperature approximately 5% higher with the conductors placed in the slots. This is due to the lower thermal conductivity and emissivity of the material of the conductors (see Table 4.1), which has a negative impact on the heat transfer along the tube. For this reason, to obtain realistic predictions, it is necessary to model the conductors.

On the other hand, it has been evaluated to what extent the shape of insertion slots in the alumina tube affects the heat transfer by comparing models *b* and *d*. Both have the same cross-sectional area and external diameter, but model *b* includes the insertion slots while model *d* is a perfect tube. The latter has 5% higher temperature. This is due to less heat being evacuated by radiation in *d* due to its smaller internal surface.

Another considered option to simplify the modelling of the screen conductors was to substitute its rectangular shape by a perfect tube, as shown in model *c*. Note that the

	Ceramic tube	Screen conductors
Material	Alumina 96%	Nichrome NiCr80/20
Thermal emissivity	0.8	0.65
Thermal conductivity ($W/m \cdot K$)	25	15

Table 4.1 Properties of the components of the beam screen.

dimensions of the tube were strategically chosen to have the same cross-sectional area as the 24 conductors. The predicted temperatures with this model are almost the same as the ones obtained with the reference model *a*.

Considering all the above, it was decided to represent the beam screen as shown in model *d*, as it is the most simple model and it gives some safety margin with respect to the most realistic model *a*.

Vacuum tank and external components:

The MKIs are surrounded by numerous components which are necessary for the conditioning and the correct operation of the magnets. They can be seen in Fig. 1.8: valves, vacuum pumps, feet, connections to the Pulse Forming Network for the HV supply... However, all those components located outside the vacuum tanks are not relevant for the study of the heat transfer within the magnets, so they have not been included in the thermal model. Instead, the vacuum tank has been represented as a perfect tubular shape, closed at both ends. In order to be able to specify a boundary condition just after the 10th yoke, a fictitious plate is introduced here (see Fig. 4.9), where adiabatic conditions are imposed.

Sharp edges and other difficult geometries:

In general, all the screws, holes and irrelevant components for the analysis have been removed. Besides, ANSYS® Workbench™ offers automatic tools to identify and solve problematic geometries such as finding gaps, small features, hard edges, sharp angles... Other components with especially complex geometries have been manually simplified. An example can be seen in Fig 4.5, where the HV plates have been simplified by removing the rounded edges and the small holes.

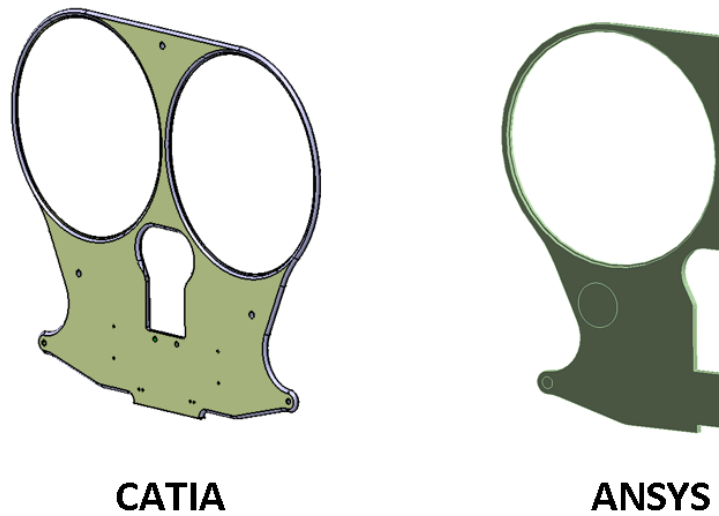


Fig. 4.5 Simplification of the geometry of the HV plate. a) CATIA model with real dimensions. b) ANSYS model after simplification of the geometry: use of symmetry and removal of rounded edges and small holes.

4.1.2 Mesh optimization

One of the advantages of ANSYS® Workbench™ is that it provides robust and easy to use meshing tools to simplify the mesh generation process. Although these tools are highly automated, they also allow for a moderate to high degree of user control. In fact, for obtaining a high quality mesh that provides physical and accurate results, the user cannot completely rely on the automatic mesh generation, but needs to assess the quality and manually adapt the settings to the analysis (see below).

In the following, the process of building the mesh for the MKI model will be explained, detailing all the settings that have been manually adapted to the specific problem under study.

Global mesh controls

First of all, the global mesh controls, to be applied to all the bodies, are configured by adjusting the settings under the “Mesh” branch, as shown in Fig. 4.6. The options that have been modified are explained below. However, these global mesh controls can be overwritten in certain components using local mesh controls (see next section).

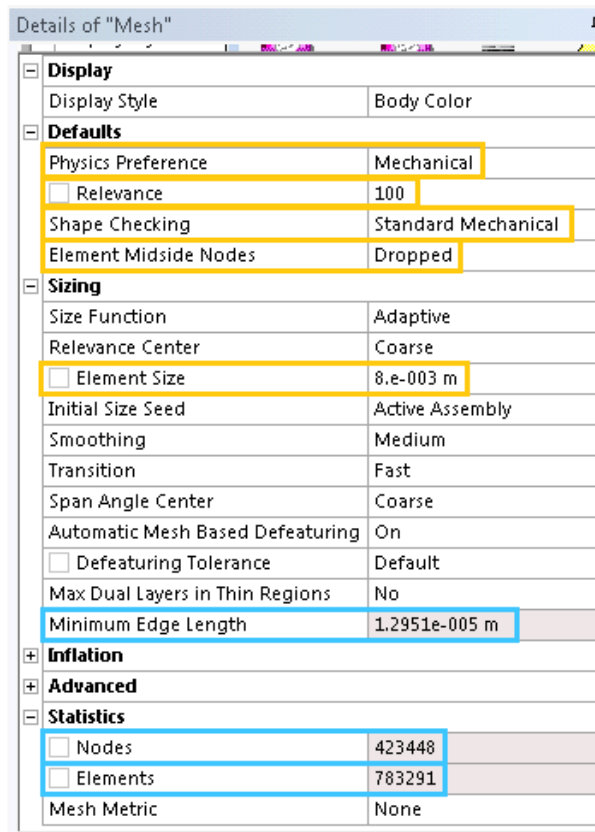


Fig. 4.6 Global Mesh controls. *Yellow: Settings that have been manually modified/ Blue: Relevant information.*

- **Physics Preference:** The available options under the *Physics Preference* are Mechanical, Electromagnetic, CFD, Explicit, and Nonlinear Mechanical. One must select the option that best adapts to the physics of the analysis type, and in accordance, the mesh will be automatically generated using different default tools for each option. For the thermal analysis of the MKIs, the Mechanical option is the one that suits best. Indeed, this is the default option when using the ANSYS Mechanical application.
- **Relevance:** The *Relevance* determines the degree of fineness of the mesh for the entire model and it can be set between -100 and 100. A low, negative value, will use a coarse mesh and it might be of interest towards high speed solutions. A high, positive value, is indicated for the cases where high accuracy is required, generating a fine mesh. For the MKIs, the relevance was set to 100 to obtain a fine mesh, in order to correctly map the non-uniform power distribution and to accurately obtain the temperature gradients within each component.

- **Shape Checking:** The software checks that the characteristics of all the generated mesh elements such as aspect ratio, jacobian ratio and element volume, among others, are below the limits imposed by the criterion selected with the *Shape Checking* tool. Otherwise, the mesh generation fails. The Standard Mechanical criterion has been selected as it has proven to be effective for linear, modal, stress, and thermal problems based on experience of many users. Indeed, this is the default option when Physics Preference is set to Mechanical.
- **Element Midside Nodes:** The *Element Midside Nodes* option allows to control whether the automatic mesh will be generated with midside nodes (quadratic/high order elements) or without them (linear/first order elements). The available options are Program Controlled, Dropped, and Kept. In general, midside nodes should be used when results can vary significantly over a single element as they increase the number of degrees of freedom, but at higher computational cost. Based on the expert knowledge of colleagues at CERN, for most non-structural analyses (thermal, magnetic, etc.), the linear elements are nearly as good as the higher order elements, and are less expensive to use. Indeed, the thermal analyses may run into thermal under/overshoot issues with high-order elements. For this reason, in the particular case of the thermal analysis of the MKIs, the Dropped option has been selected, meaning that linear elements will be used.
- **Sizing:** Even though the minimum length detected is in the order of 0.01 mm (see *Minimum Edge Length* in Fig. 4.6, marked in blue), it corresponds to corners of components which are not relevant. Instead, a minimum element size of 8 mm has been specified, which is of the order of magnitude of the thickness of the HV and ground plates, and it leads to a reasonable number of elements, approximately 800.000 (see *Elements* in Fig. 4.6, marked in blue). A detailed comparison with different minimum element size was performed and it showed that 8 mm does not lead to a loss of accuracy.

Local mesh controls

Local mesh controls have been applied to some of the components that are critical for the thermal analysis or problematic for the automatic mesh generation due to their geometry. This can be done by applying, to the geometry of interest, the different tools available below the tree object *Mesh Controls* (see Fig. 4.7).

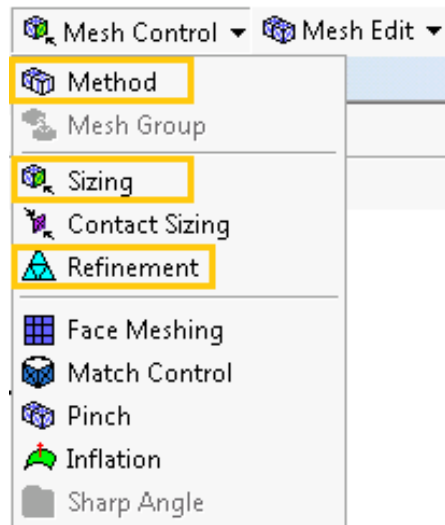


Fig. 4.7 Local Mesh Controls. *Yellow: Setting that have been modified.*

- **Refinement:** In the components of the MKIs where the heat is deposited, which are the ferrite yokes and rings, the mesh has been refined locally in the area where the heat is introduced, by means of the *Refinement* tool. This way, the size of the elements in the selected region is reduced relative to the size of the original elements. The level of refinement is modified by setting its value between 1 and 3, providing the minimum and maximum refinement respectively. In this case, it was set to 3 as high temperature gradients were expected.
- **Sizing:** The global minimum size of the elements was 8 mm, as indicated previously. However, in some regions of special interest it was necessary to obtain the temperature gradient through the thickness, e.g. in the HV plates or the HV busbar in contact with the yokes. In these regions, a smaller minimum size of the elements has been set locally with a value of half their thickness, so that the temperature drop can be properly mapped.
- **Method:** The methods available are Automatic, Tetrahedral, Hexa Dominant, Sweepable and MultiZone. The method chosen will determine the type of elements to be used. Globally, the Automatic option is the default one: It attempts to use a pure hexahedral mesh in sweepable bodies, that is, in bodies where a source mesh defined in one of the surfaces can be swept through the body, spacing it by a certain incremental dimension or by splitting the swept side faces into a desired number of divisions; otherwise, it creates an unstructured mesh, with hexahedrons and tetrahedrons.

In general, tetrahedrons can adapt better to complex geometries. However, higher number of elements are needed when a body is meshed with tetrahedrons instead of hexahedrons. For this reason, a hybrid mesh that contains hexahedrons where possible, especially in anisotropic or critical areas, is often the best option.

Once the mesh has been generated with the Automatic tool, the user must check carefully if there are bodies with sweepable regions which, due to the presence of round corners or other minor geometrical issues, have not been identified as sweepable and hence tetrahedrons are used in this whole region. In these bodies, the MultiZone tool has been used locally. It divides the geometry into sweepable and not-sweepable regions, and the user can select the type of element to be used in each of these regions by adjusting the settings below the branch *Details of "MultiZone"* (see Fig. 4.8):

Details of "MultiZone-Beam screen" - Method	
Scope	
Scoping Method	Geometry Selection
Geometry	1 Body
Definition	
Suppressed	No
Method	MultiZone
Mapped Mesh Type	Hexa
Surface Mesh Method	Program Controlled
Free Mesh Type	Hexa Dominant
Element Midside Nodes	Use Global Setting
Src/Trg Selection	Automatic
Source Scoping Method	Program Controlled
Source	Program Controlled
Sweep Size Behavior	Sweep Element Size
<input type="checkbox"/> Sweep Element Size	Default
Advanced	
Preserve Boundaries	Protected
Mesh Based Defeaturing	Off
Minimum Edge Length	1.e-003 m
Write ICEM CFD Files	No

Fig. 4.8 Settings of MultiZone method. *Yellow: Settings that have been modified.*

- * *Mapped Mesh Type*: It allows to select the type of element to be used in the sweepable regions. The Hexa option is chosen, which means that a pure hexahedral mesh will be generated.
- * *Free Mesh Type*: It allows to select the type of element to be used in the unstructured, not sweepable, regions. Hexa Dominant is the selected option, which means that the mesh will be formed mainly by hexahedrons if possible, but the most complex areas will be filled with tetrahedrons.

The mesh is pictured in Fig. 4.9. Note that the right-hand-side end plate is fictitious and was introduced to specify the adiabatic boundary conditions.:

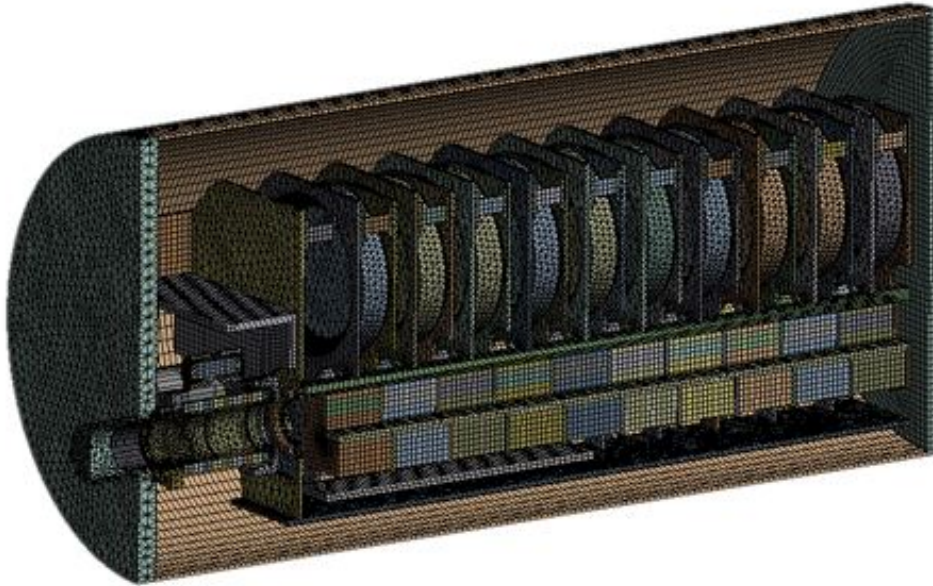


Fig. 4.9 ANSYS thermal model with mesh.

4.2 Modelling boundary conditions

Once the mesh has been generated, the boundary conditions must be properly defined. The way in which they have been obtained and implemented in the ANSYS model is detailed hereunder:

4.2.1 Convection coefficient

Revision of the estimated convection coefficient values:

As mentioned in section 2.2, originally in the 2D models the convection coefficient for the outside of the vacuum tank was defined as a constant number of $7 \text{ W/m}^2 \cdot \text{K}$ for representing the natural air convection to the ambient. This value was an approximate estimation, used to perform initial studies. However, as the project advanced, a higher level of accuracy was required. For that, the value was calculated analytically with the following formula [17]:

$$h = \frac{k_{fluid} Nu}{D}, \quad (4.1)$$

where h is the convection coefficient, k_{fluid} is the thermal conductivity of the fluid, in this case the air, D is the external diameter of the tank, and Nu_D is the Nusselt number with the diameter as characteristic length. The latter was obtained with the Churchill and Chu correlation [28]:

$$Nu_D = \left(0.6 + \frac{0.387 \cdot Ra_D^{1/6}}{(1 + (0.599/Pr)^{9/16})^{8/27}} \right)^2 \text{ for } Ra_D \leq 10^{12}, \quad (4.2)$$

where Nu_D , Ra_D and Pr are the Nusselt, Rayleigh and Prandtl adimensional numbers respectively, defined for the external diameter as characteristic length. Note that the Rayleigh and Prandtl numbers are dependent on the temperature of the film, obtained as the average between the temperature of the fluid, assumed to be a constant ambient temperature of 25°C, and the one of the external wall of the tank. For this reason, the convection coefficient obtained is dependent on the tank temperature too. The values are shown in Fig. 4.10:

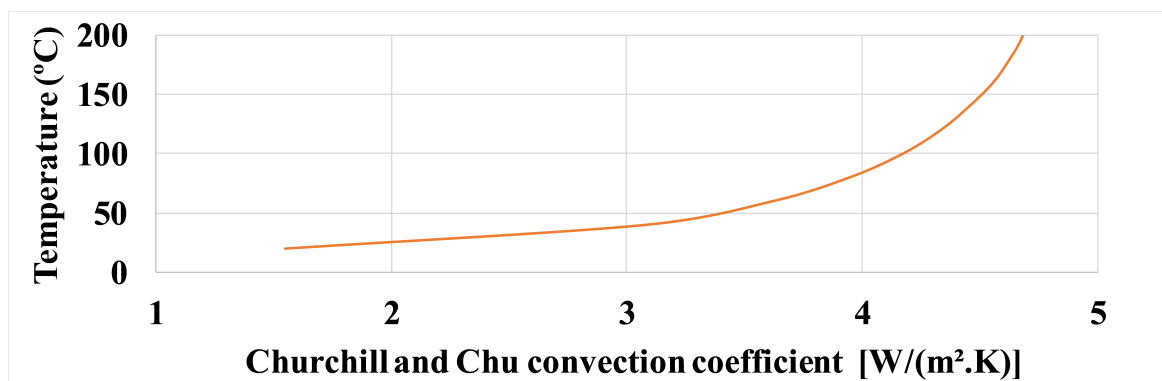


Fig. 4.10 Convection coefficient obtained from Churchill and Chu correlation.

According to those results, for the whole range of temperatures expected in the tank (from ambient to approximately 100°C), the convection coefficient is estimated to be lower than the $7 \text{ W}/(\text{m}^2 \cdot \text{K})$, assumed in the 2D model, which indicates that the assumption was optimistic. Two simulations with the same power introduced in rings and yokes, but different values of convection coefficient, have been carried out to estimate its influence on the results: One with the constant convection coefficient and the other with the temperature dependent coefficient calculated with the Churchill and Chu correlation. Results are shown in Fig. 4.11:

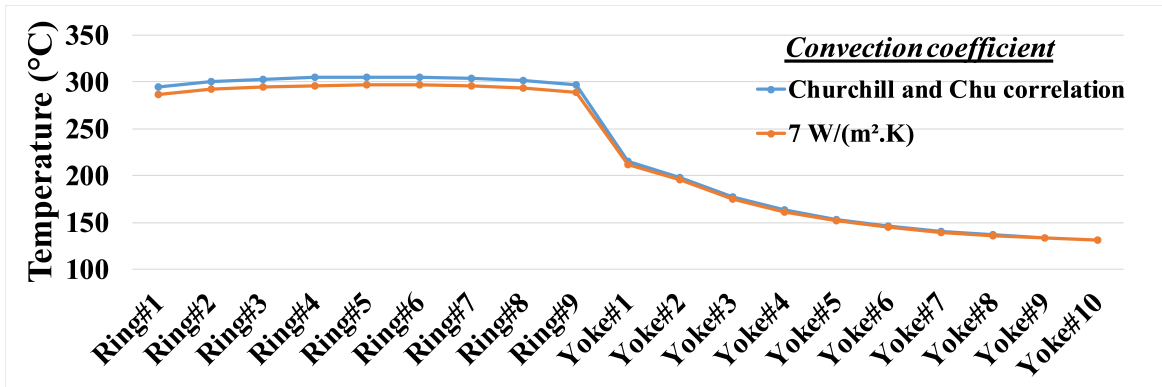


Fig. 4.11 ANSYS ferrite temperature predictions for different values of the convection coefficient.

The results are very similar, especially for the yokes. However, throughout the research, several LHC operating scenarios will be studied, leading to different temperatures of the tank. In the cases where the temperature of the tank is below 45°C , the convection coefficient is remarkably reduced as indicated in Fig. 4.10. This would lead to a bigger difference in comparison to $7\text{ W}/(\text{m}^2 \cdot \text{K})$. Besides, there was no remarkable difference in the computing times of both simulations. For those reasons, it was decided to implement the convection coefficient based on the Churchill and Chu correlation.

Modelling of the bake-out jackets

Another improvement implemented was the modelling of the bake-out jackets. As it has been mentioned in section 2.2, the jackets were not simulated in the first 2D models. Instead, to represent the effect of the thermal isolation, the convection coefficient for the external surface of the tank was reduced from $7\text{ W}/(\text{m}^2 \cdot \text{K})$ to $1.9\text{ W}/(\text{m}^2 \cdot \text{K})$ [14]. This approach is, again, very simple and valid only to obtain approximate estimations. However, to perform the simulations with a higher level of accuracy requires to include the bake-out jackets in the model.

The jackets are composed of different layers, as it is shown in the drawing of the cross-section in Fig. 4.12. The heating elements are covered with a type E glass fiber layer, and the outer surface finish is an aluminized glass fiber cloth, which reduces heat leaks by thermal radiation. The jackets are closed by means of hooks attached to the outer covering cloth. This can be appreciated in the photo of a jacket in Fig. 4.13.

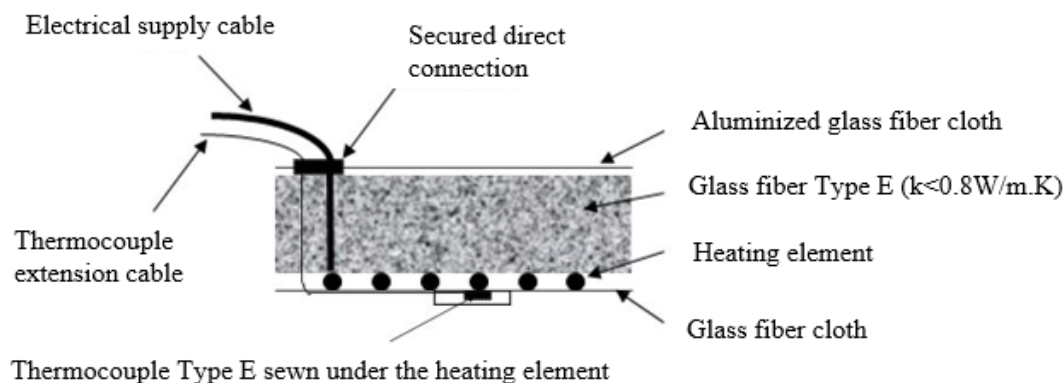


Fig. 4.12 Cross-section of bake-out jacket (Thickness 28 mm)



Fig. 4.13 Photo of a bake-out jacket.

For properly modelling of the bake-out jackets, the thermal constraints imposed by each of the layers were defined. On the one hand, the insulation given by the poor thermal conduction was represented with a cylindrical body around the tank, with the same thickness as the bake-out jackets, and the material properties of the type E glass fiber. On the other hand, the radiation shield given by the external aluminized glass fiber was represented by defining a low value of thermal emissivity (0.05) on the external surface of the cylinder. This approach was considered accurate enough because, due to the negligible thickness of the aluminized fiber, the thermal conduction does not play a significant role.

The ANSYS model including the bake-out jackets is presented in Fig. 4.14:

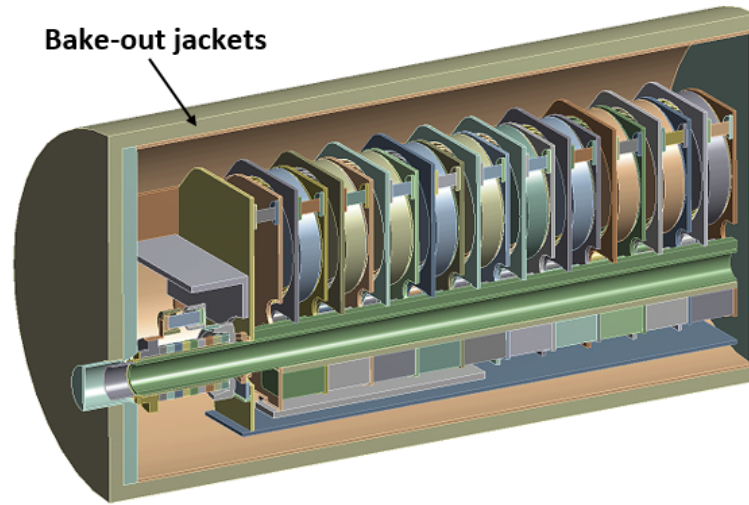


Fig. 4.14 ANSYS thermal model including the bake-out jackets.

4.2.2 Power loss

The calculation of the power loss requires several steps, which are shown schematically in Fig. 4.15.

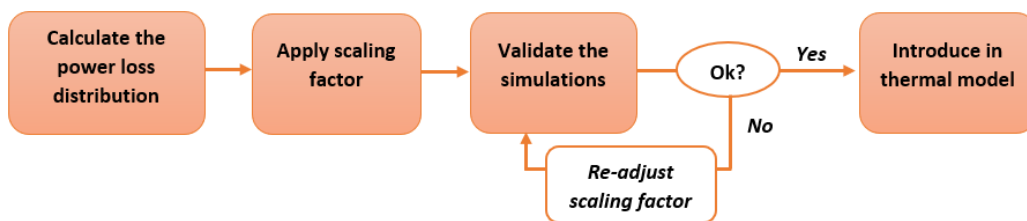


Fig. 4.15 Methodology to obtain the power loss distribution.

In the following, each of the steps is going to be described in detail:

1. Calculation of the power loss distribution

The calculation of the heat load has been thoroughly described in Chapter 2. As a summary, the steps are:

- (a) Obtain the longitudinal beam coupling impedance of the magnets using the wakefield solver of CST Particle Studio®.
- (b) Calculate the total power loss with the Equation 4.3:

$$P_L = 2I_b^2 \sum_{n=0}^{\infty} |Y(\omega_n)|^2 \Re\{Z_L(\omega_n)\}, \quad (4.3)$$

- (c) Obtain the power distribution in each of the components. It is obtained from the CST simulations by placing power loss field monitors at multiples of 40 MHz, which is the LHC's beam spectrum harmonics for 25 ns bunch spacing. This allows to obtain a map with the distribution of the dissipated power within the magnet.

The CST models evolved throughout the project by improving the mesh quality, adjusting the settings of the simulations to adapt better to the problem or modelling more accurately the components, among others.

2. Scaling factor

The need of applying a scaling factor to the heat load calculated with CST arose after benchmarking predictions against measurements of the beam coupling impedance carried out in the lab. The measurements were done for all the magnets before their installation in the LHC during LS1, so all of them had the Post-LS1 design, with the upgraded 24-screen-conductors beam screen installed. The values of the total power measured in each magnet, calculated for the nominal beam parameters of Run2, are shown in Table 4.2, emphasizing the MKI8D (in red), having the highest power of 125 W:

Magnet	Total power (W)
MKI2A	110
MKI2B	91
MKI2C	100
MKI2D	96
MKI8A	83
MKI8B	88
MKI8C	118
MKI8D	125

Table 4.2 Total power in all the magnets calculated from measured beam coupling impedance, and Run2 beam parameters (2808 bunches, 25ns spacing, $1.15E11$ ppb, 1ns bunch length)

Two conclusions could be withdrawn from these results:

- Although all the MKIs were nominally identical, the total power loss estimated for each magnet from measurements of the beam coupling impedance was different, being 51% higher for the worst-case MKI8D compared to the best-case MKI8A.

This is in line with observations during LHC operation, as different temperatures were measured in all the magnets, being always MKI8D the hottest one.

- The power loss obtained from simulations was underestimating the worst-case measurements: This discrepancy could be attributed to uncertainties in the model.

To compensate for the discrepancies between measurements and simulations, the power obtained from simulations has been historically scaled to the one measured in the worst-case MKI.

The process is shown in the following schema. Note that the 125 used in the calculation of the scaling factor corresponds to the highest power measured in MKI8D (see Table 4.2):

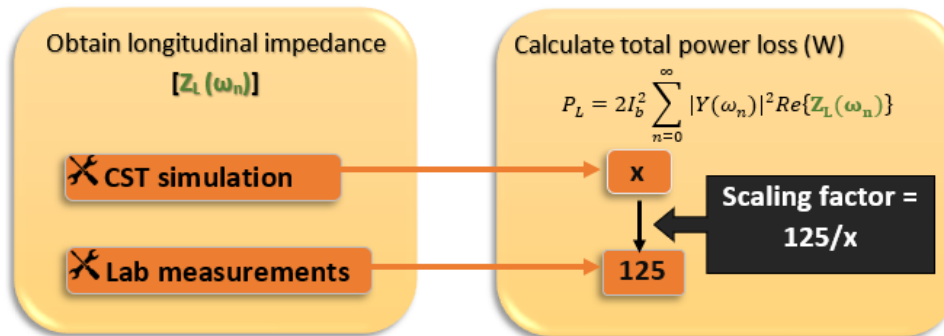


Fig. 4.16 Scaling factor calculation.

3. Introducing the power in the ANSYS model

The power distribution calculated from CST is introduced in the ANSYS model as an Internal Heat Generation (W/m^3). In general, looking at the power map obtained from the CST simulations, it was observed that the power in the yokes is mostly concentrated in the area most exposed to the beam, located at the internal surface of the legs. In the rings, the power distribution is close to uniform.

In the first 2D models, to account for the power concentration in the yokes, the heat load was introduced in the area highlighted in orange in Fig. 4.17:



Fig. 4.17 Heat load introduced in the ferrite yokes in the 2D thermal model.

In the 3D models, this approach was still applied but this time the heat load was introduced in a volume, as indicated in orange in Fig. 4.18:

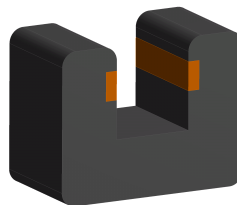


Fig. 4.18 Heat load introduced in the ferrite yokes in the 3D thermal model.

However, in the last stages of the project, thermo-structural analyses were carried out for the design of a cooling system. This was necessary to assess the stresses generated by thermal gradients between the heat sink and the hottest areas, caused by concentrated heat load [78]. Hence, the simplistic approach of introducing the power loss averaged in each component was not valid anymore, and the need of importing accurately the power distribution obtained with CST[®] to ANSYS[®] arose. To do this across the dissimilar mesh interface used in each of these softwares, the nodes of the CST[®] mesh are mapped to the local coordinates of a node/element in the ANSYS[®] mesh [2]. With this approach the heat distribution in the rings and yokes is accurately mapped in ANSYS[®], as it can be seen in Fig. 4.19 and Fig. 4.20 respectively.

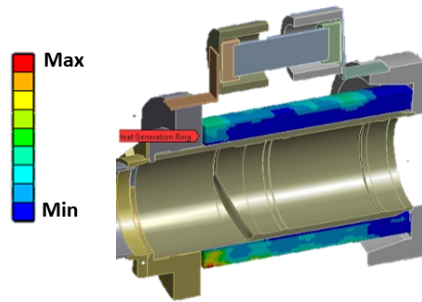


Fig. 4.19 Example heat load imported from CST introduced in the upstream ferrite rings.

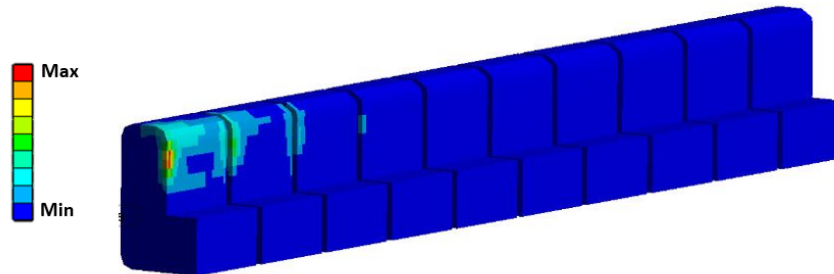


Fig. 4.20 Example heat load imported from CST introduced in the upstream ferrite yokes.

4. Validation of the models

All the proposed models of power distribution were validated using the thermal simulations. For this, the conditions during LHC operation were simulated in ANSYS and the predicted temperatures were compared to the measured ones in the hottest MKI, MKI8D, during a fill of the LHC.

The heat loads introduced in ANSYS included the initially estimated scaling factors. If the predicted temperatures did not match the measured ones, the value of the scaling factor was readjusted. This process was iterated until a good correlation between measurements and simulations was achieved, and the model could be approved.

The temperatures were measured with four PT100 per magnet, but they are not installed directly on the ferrite yoke, since it is pulsed to high voltage. Instead, two of them are located on the side plate at the position of the 3rd and the 31st yokes, and the other two are located on a clamp which is nominally in contact with each set of nine rings at both ends of the magnet, as shown in Fig. 4.21 and Fig. 4.22 respectively.

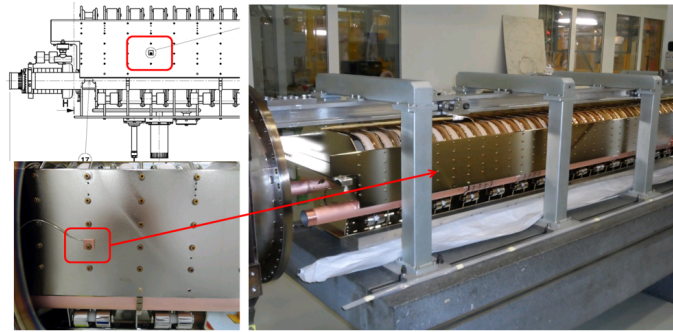


Fig. 4.21 One of the two PT100 located on the side plate.

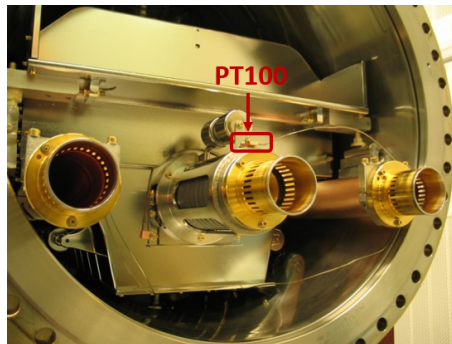


Fig. 4.22 PT100 located on the clamp next to the ferrite rings.

For clarification, the notation used for the naming of temperature measurement of the different PT100 is as follows:

MKI.Identification letter.Injection point.Beam line number:PT100 location

- *Identification letter:* A, B, C or D, corresponding to each of the four MKIs per injection point.
- *Injection point:* 5L2 for magnets at injection point 2 or 5R8 for magnets at injection point 8.
- *Beam line number:* B1 for magnets at injection point 2 or B2 for magnets at injection point 8.
- *PT100 location:* MAGNET is used for the sensors on the side plate (Fig. 4.21) and TUBE for the sensors on the clamp next to the rings (Fig. 4.22). This is followed by *_UP* if the sensor is located at the upstream end of the magnet, or *_DOWN* if it is at the downstream end.

Details on the validation of each model will be further discussed in the next section.

	Type of analysis	Yokes		Rings	
		Number	Power	Number	Power
1	2D	1 (cross-section)	Averaged per surface.	Not included	-
2	3D	8	Different, averaged per volume.	9	Same in all rings, averaged per volume.
3	3D	10	Different, averaged per volume.	9	Different in each ring, averaged per volume.
4	3D	10	3D imported from CST.	9	3D imported from CST.

Table 4.3 Summary of power distribution from different CST models.

4.3 Presentation and validation of the models

A summary of the main power distribution models that have been used at the different stages is shown in Table 4.3:

The corresponding normalized power distribution (1 W distributed along the magnet) for each of the models described in Table 4.3 are presented in Fig. 4.23. Note that Model 1 is not represented as it was only used for preliminary studies before this thesis.

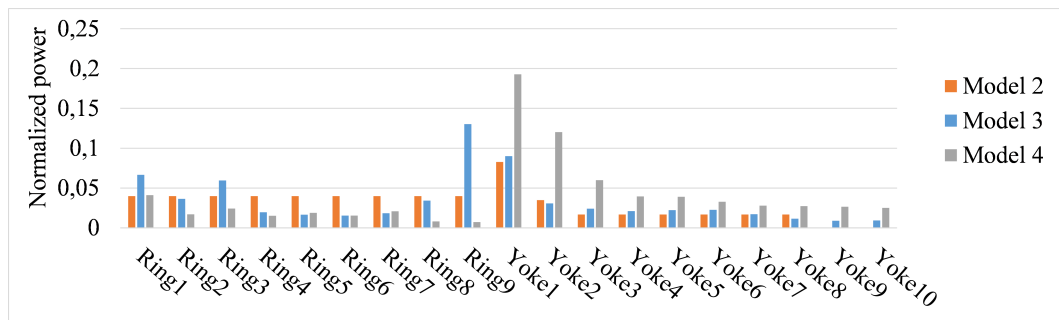


Fig. 4.23 Comparison of the normalized power distribution for the different models used.

As specified, a scaling factor was applied to the total power calculated for each CST model to match the 125 W obtained from the measurements of the beam coupling impedance (see Fig. 4.16). The values are shown in Table 4.4:

Model	Total Power Loss (W)	Scaling factor
2	42	x3
3	31	x4
4	52	x2.4

Table 4.4 Total power loss and the corresponding scaling factors applied to each power distribution model.

Each of these CST models were used as input for the thermal studies at the different stages of the thesis. As can be appreciated, the differences between them are remark-

able, especially in the 9th ring and the first few yokes. This implies that some of the cooling alternatives that were considered to be efficient enough at the beginning of the studies, were not any further considered as the power distribution models were evolving.

In the following, the validation of each of the models and the readjustment of the scaling factor is shown, except for Model 1 (2D model), as it was a very simple version for initial estimations which was used before the start of the thesis.

Validation of Model 2

To validate this model, steady-state conditions reached during long fills of the LHC were simulated. The power during a selected long fill of the LHC was first calculated, following the procedure explained in Chapter 2. Then, this power was averaged over the duration of the fill, which was then introduced in ANSYS to perform a steady-state simulation. The selected fill and the measured temperatures are shown in Fig. 4.24. For simplification, only the temperatures measured in sensors at the upstream end of the magnet have been included in the plot.

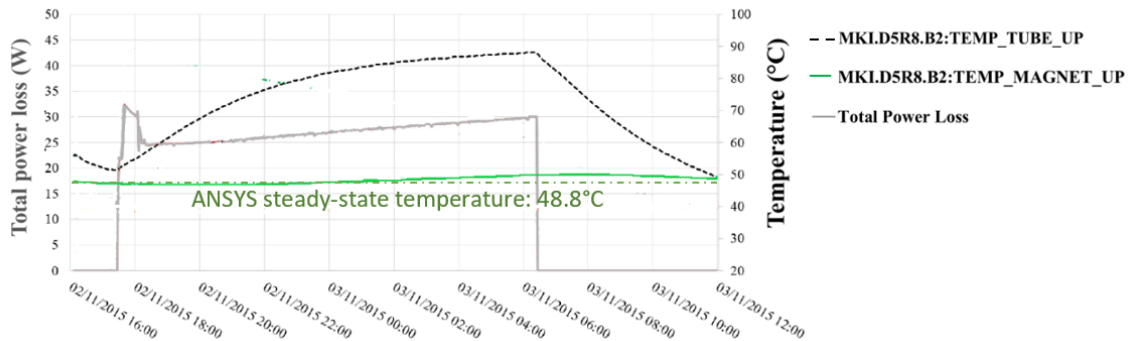


Fig. 4.24 LHC fill #4569 used for validation of Model 2, with the total power scaled by 3. 25 ns beam, 2244 bunches, $1.15e11$ protons per bunch.

It can be appreciated that MKI.B5R8.B2:TEMP_MAGNET_UP, which corresponds to the PT100 located at the side plate, measured approximately 49°C once the steady-state regime was reached during the fill. For the averaged power during the fill, the steady-state simulation resulted in a temperature of 48.8°C at the location of the mentioned PT100. This indicated good agreement between measurements and simulations.

Validation of Model 3

This model was validated with a transient analysis. In this case, the power loss calculated for each of the upstream ferrite rings and the first 10 yokes during an LHC fill was calculated and introduced in ANSYS as a function of time. The results are shown in Fig. 4.25.

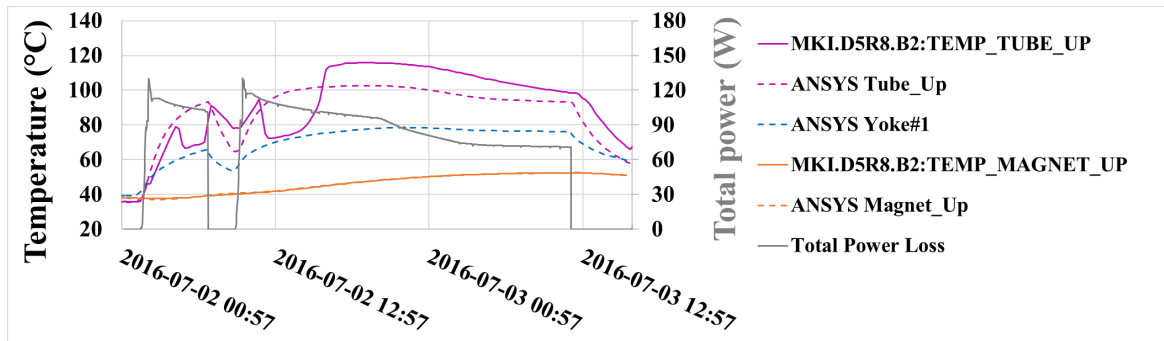


Fig. 4.25 Measurements during LHC fills #5068 and #5069 and predictions for Model 3, with the total power scaled by 4 (25 ns beam, 2064 bunches, $1.27e11$ protons per bunch).

As can be seen, the temperatures measured with the sensor located at the side plate (Magnet_Up) show very good agreement with the ones predicted with ANSYS: both curves overlap. However, for the temperature of the clamp next to the ferrite rings (Tube_Up), there is some discrepancy attributed to the uncertainty about the value of the thermal resistance at the contact between the rings and the clamp, which is very difficult to estimate.

To compensate for these discrepancies, the scaling factor was increased by a factor of 1.25, that is from 4 to 5. The predicted temperatures at the location of the sensors with this extra safety factor are shown in Fig. 4.26.

The following conclusions can be withdrawn:

- By comparing Fig. 4.25 and Fig. 4.26, it becomes evident that total power scaled by 5 leads to more accurate predictions for the Tube_Up readings, as well as a small safety margin for Magnet_Up predictions.
- Rapid changes occur in the temperature readings at Tube_Up. This behaviour has been observed in several MKI magnets, always in the PT100 located at Tube_Up, when the heating/cooling rates are high, i.e. when the beam is injected, but also after the extraction of the beam, when the magnet starts to cool down suddenly. In Fig. 4.27, temperature readings at Tube_Up in the eight MKIs are shown.

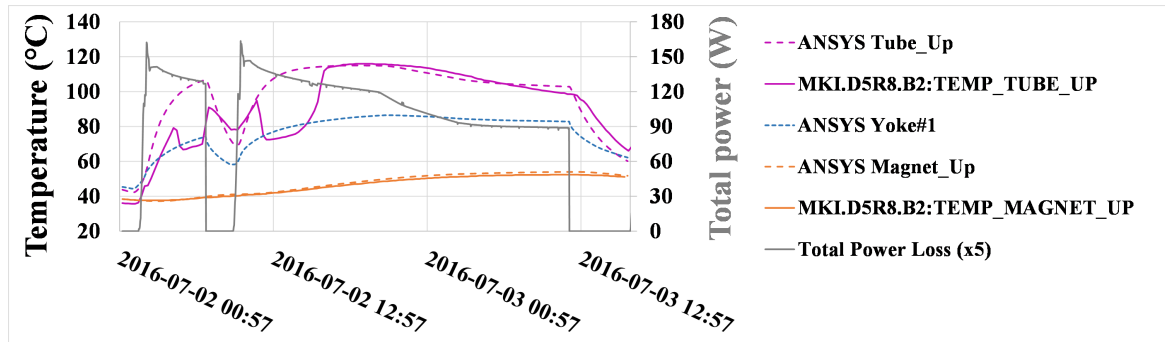


Fig. 4.26 Measurements during LHC fills #5068 and #5069 and predictions for Model 3, with total power scaled by 5 (25 ns beam, 2064 bunches, 1.27×10^{11} protons per bunch).

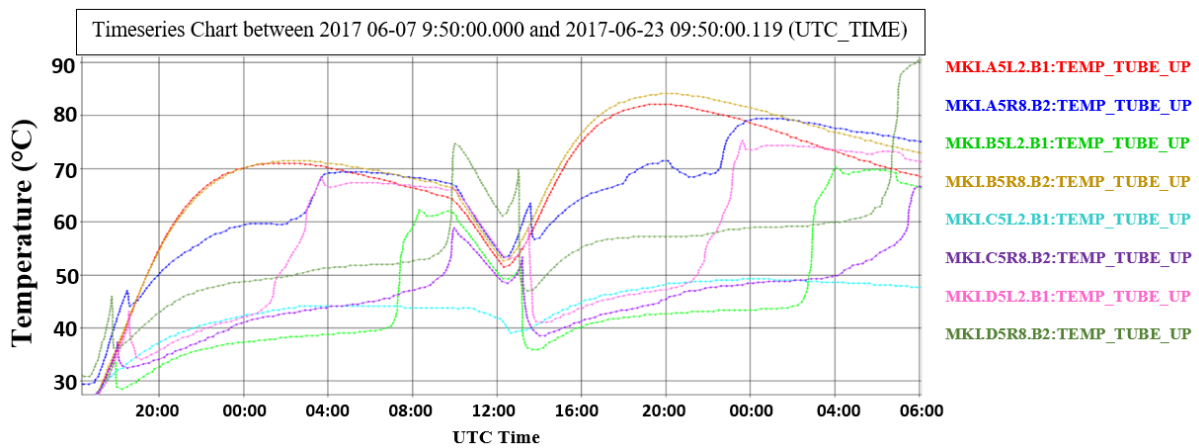


Fig. 4.27 Measured Tube_Up temperatures in the eight MKI magnets from 7/6/2017 to 26/6/2017.

This phenomenon cannot be physical as the changes in temperature are too fast to be realistic, considering the thermal inertia of the ferrite rings. One hypothesis was that the temperature drop was caused by the electromagnetic interaction of the sensors with the beam. However, the idea was discarded as the PT100 are shielded well, and the effect is relatively slow for that and also occurs after the beam has been dumped: following beam dump no electromagnetic interaction with beam is possible, and the MKIs start to cool down. The most likely reason might be the loss of contact between the PT100 and the clamp of copper that is used to hold the PT100, due to their different thermal expansion coefficients. The PT100 is positioned inside the clamp by applying pressure and it is held by tightening the clamp with a screw (see Fig. 4.28). The repeated thermal cycles of the magnets during LHC operation, as well as the bake-outs done for conditioning,

may lead to loosening of the pressure contact. That would also explain why the sudden drops in temperatures only happen in some of the magnets, and at different heating or cooling rates.

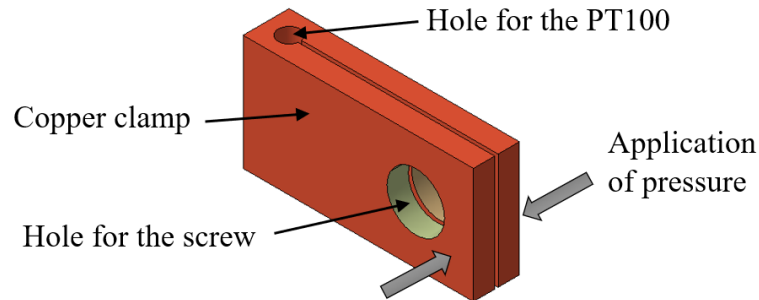


Fig. 4.28 Copper clamp for the PT100.

- This validation was also used for assessing the sensitivity to the power loss at the locations of the PT100. Ideally, they should be placed in parts of the magnet where changes in power loss results in reasonable changes in the temperature, that is a high sensitivity. In order to evaluate the quality of the present locations of the PT100, and to study potential new locations, the increase in temperature observed when the power scaling was increased from 4 to 5 was evaluated at different locations. For simplification, results will only be shown for the best alternative locations, which are indicated in Fig. 4.29.

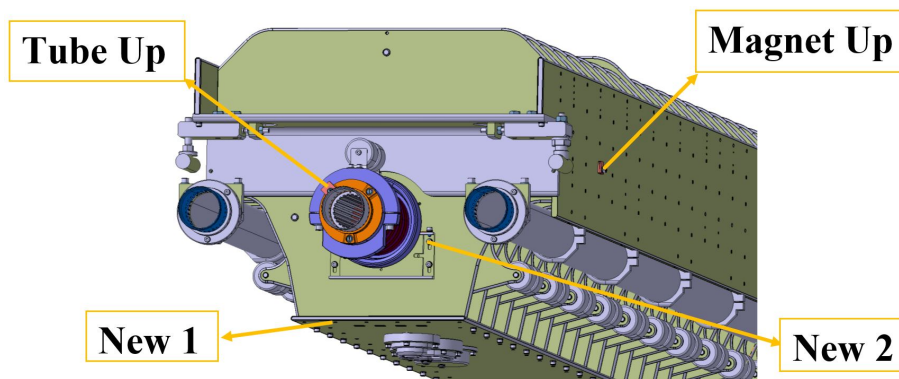


Fig. 4.29 PT100 location.

The temperatures predicted with both powers, which are shown in Fig. 4.25 and Fig. 4.26, have been plotted together in Fig. 4.30. For assessing the sensitivity at each location, the change of the maximum predicted temperature during the cycle has been calculated. A summary of the results is shown in Table 4.5.

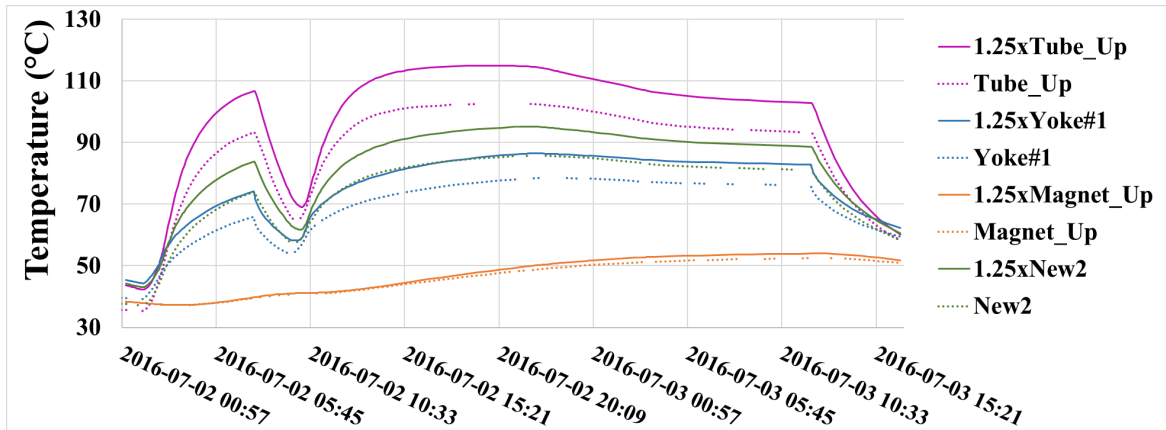


Fig. 4.30 Analysis of the suitability of the current PT100 locations and proposed alternatives (Fills #5068 and #5069).

Location	Increase of temperature with 25% more power
First ferrite yoke	11%
Tube_Up	13%
Magnet_Up	4%
New2	14%

Table 4.5 Effect of increasing the power by 25% upon the maximum predicted temperatures in actual and proposed PT100 locations.

According to these results, the temperature of the first ferrite yoke, which is the critical component of the magnet, increased by 11%. This value is taken as a reference, so that the temperatures at the locations of the PT100s should change by a similar percentage to be considered representative. In the case of the Tube_Up, this condition is fulfilled. However, the maximum temperature at the side plate (Magnet_Up) changed only a 4%, from 52.5°C to 53.9°C, so this cannot be considered as an optimum location. Results show that a better option would be to locate the PT100 on the first ground plate, close to the beam aperture, which is directly exposed to the heat radiated from the rings (see Fig. 4.29, label New2).

In the last stages of the project, one of the magnets installed in the LHC was exchanged for another with several modifications (more details will be given in the following chapters). This allowed to install two new sensors in the upgraded magnet. The locations were chosen according to the results commented above, at

the locations shown in Fig. 4.29. The original two sensors were not removed, so as not to lose the qualitative comparison with the other magnets.

Validation of Model 4

For the validation of the last and most complex model, the same approach as in Model 3 was used: a fill of the LHC was selected and the equivalent power deposited in each ring and yoke were calculated as a function of time. This was introduced in ANSYS to perform a transient simulation to compare predicted and the measured temperatures. However, in this case the analysis was more complex. While in Model 3, the calculated power dissipation in each of the nine rings and the ten yokes was averaged and introduced in a volume (as shown in Fig 4.18), in Model 4 the power was directly imported from CST, resulting in a thermal map as shown in Fig 4.20 and Fig. 4.19. This thermal map had to be generated at each time step in a transient analysis, which implied the calculation of approximately 1,375,000 power data to be introduced in the corresponding nodes of the rings and yokes in ANSYS (note that the mesh was refined in those components to obtain accurately the temperature gradients).

As mentioned before, this model was implemented in the last stages of the project for supporting the design of the cooling system, which required a more accurate representation of the power distribution to model properly the temperature gradients. By that time, the historically hottest magnet installed in the LHC, MKI8D, had been upgraded with some modifications that, according to simulations, would reduce and redistribute the deposited power (more details about this upgrade will be given in the following chapters). Thanks to the upgrades, MKI8D was not the hottest magnet anymore. However, the cooling system was going to be installed together with these modifications. Thus, the temperature readings of the new MKI8D were again used for benchmarking the thermal simulations.

Due to the complexity of the analysis, a transient simulation required approximately one week of CPU to simulate the LHC fill #6719. The results are shown in Fig. 4.31.

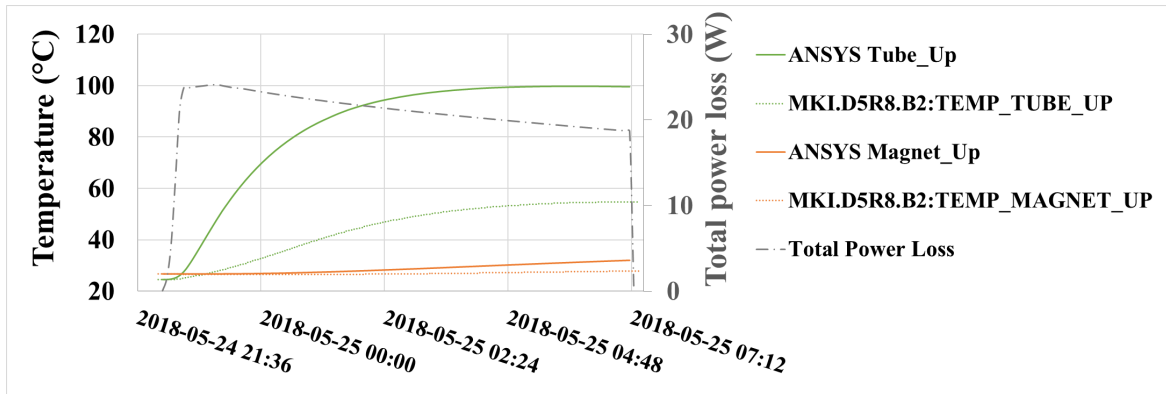


Fig. 4.31 Measurements during LHC fill #6719 and predictions for Model 4, with scaling factor of 2.4 (25 ns beam, 2544 bunches, $1.1e11$ protons per bunch).

The predictions overestimated the temperatures, which is highly remarkable in the case of the Tube_Up readings. This inconsistency led to a thorough review of the way in which the scaling factor was calculated (see Fig. 4.16). It was concluded that the lab measurements used for benchmarking might not be accurate enough due to the impracticality of reproducing the LHC conditions without beam: it is not possible to measure the impedance of the magnets at the LHC nominal frequencies with the lab measurement technique used [81]. For this reason, the approach was modified for Model 4: The calculated power would be introduced without any scaling factor, and if needed, a correction would be applied until the predicted temperatures in ANSYS matched the measured ones.

The results for the power without being scaled are shown in Fig. 4.32).

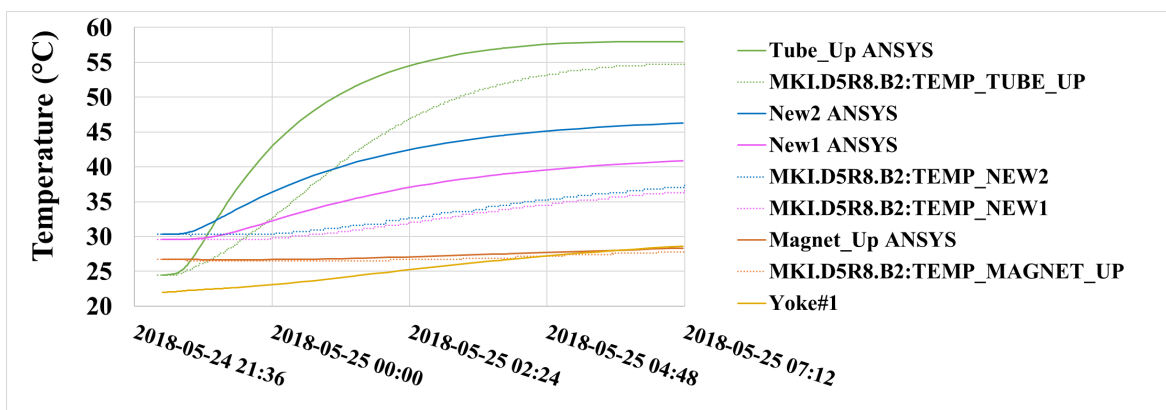


Fig. 4.32 Measurements during LHC fill #6719 and predictions for Model 4, without scaling factor (25 ns beam, 2544 bunches, $1.1e11$ protons per bunch.)

It can be seen that the predicted temperatures still overestimate the measurements but they are more consistent: The maximum temperature predicted for Tube_Up is 58°C in comparison with the 55°C measured. The readings of the two additional sensors installed in this magnet are also plotted (see Fig. 4.29), confirming that in these locations the predictions overestimate the temperatures too. It is preferable that the simulations are slightly pessimistic to have a safety margin. For this reason, it was decided not to apply any correction to the calculated power for the upgraded MKI design.

The following Table 4.6 compiles the values of the initial scaling factors used in each of the models based on lab measurements, and includes the correction applied to those factors:

Model	Power Loss for Run1 [W]	Scaling factor	Correction	Corrected scaling factor	Corrected Power Loss for HL-LHC [W]
2	42	x3	x1	x3	504
3	31	x4	x1.25	x5	616
4	52	x2.4	/2.4	x1	208

Table 4.6 Total power loss for Run1 and the corresponding correction factors applied to each power distribution model.

In the following chapters, where the studied alternatives will be presented, it will be indicated the corresponding power distribution model that was used.

Chapter 5

Studied alternatives

In this chapter, the main alternatives that were proposed and studied for limiting the temperature of the magnets below the Curie threshold are presented. The limitations encountered are discussed and conclusions are drawn taking into account the technical, economical and timing aspects for each case. Finally, the selected solution will be presented providing the corresponding justification, and the details of its design and implementation will be further explained in Chapter 6.

5.1 Increasing thermal emissivity of vacuum tanks

As was mentioned in Chapter 2, the internal surface of the vacuum tanks was very shiny as they were electropolished. This led to a very low emissivity, greatly limiting the radiative cooling of the ferrite yokes [67]. In the initial stages of the project, the investigation was oriented towards finding a suitable, vacuum compatible treatment to increase the thermal emissivity to improve the heat extraction from the yokes. The main interest of this approach resided on the fact that it was a passive cooling method, with the implicit advantage of not depending on mechanical systems, but using wisely the natural heat flow.

The initial calculations performed with the available 2D models indicated a significant reduction of the temperature in the ferrite yokes with the increase of the emissivity of the vacuum tanks. The improvement can be appreciated in Fig. 5.1: For low values of thermal emissivity, a relatively small increase significantly reduces the ferrite temperature. However, for an emissivity greater than 0.6, the benefit of the same increase in emissivity is relatively small. Note that this simulations was done for 250 W/m (total power of 616 W), which is approximately 30% higher than that calculated for the HL-LHC worst-case-scenario (191 W/m, see Table 2.1).

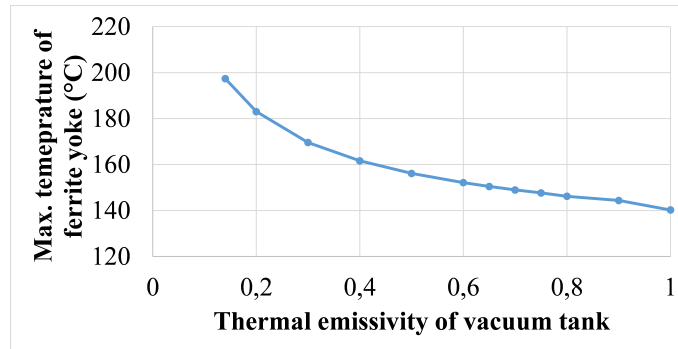


Fig. 5.1 Maximum predicted temperature of the yoke vs emissivity of the vacuum tank. Simulation performed for Model#1 of power deposition (see Table 4.3). Total power: 616 W

The promising results were encouraging to follow this line of research. As radiation heat transfer is a surface phenomenon, the emissivity can be modified by texturing the surface with a method that provides sufficient control over surface feature morphology. Ion bombardment is among these methods, which can be used to create almost any type of desired surface topography. In particular, absorption of more than 90% has been reported after treatment [30]. Some of the tanks were treated with ion bombardment in an atmosphere of argon and oxygen at Bodycote[®], but the results were not as good as expected as it has been commented in Chapter 2 [14].

As the project advanced and the new 3D models were developed for analysis, simulations were re-launched to confirm that this approach was effective enough. Results are shown in Fig. 5.2:

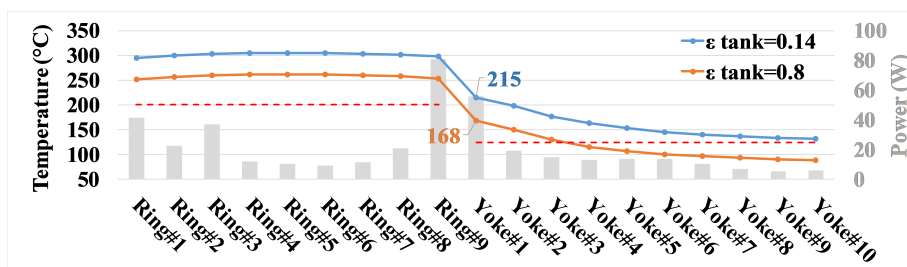


Fig. 5.2 Maximum predicted temperature per component for different thermal emissivity of the vacuum tank. Dashed red line: Curie temperature of ferrite types CMD5005/8C11 and 4M2 used in yokes and rings respectively. Model 3 of power deposition for HL-LHC. Total power: 616W.

These predictions for HL-LHC operation confirmed again that a considerable benefit for the temperatures of all the components could be gained by increasing the thermal emissivity of the tanks, but even when assuming a value of 0.8, the first three yokes would still be above their Curie temperature, with the first yoke at 168°C. However, given the fact there are no

mechanical risks associated with this passive cooling technique, it was decided to keep it as the baseline solution while investigating complementary measures to further reduce the temperature of the first yokes below their Curie point.

A test campaign was launched in collaboration with several companies to find suitable treatments. Nevertheless, due to the dimensions and shape of the vacuum tanks, this was challenging or even not possible for some techniques. Besides, considering that the MKIs will be operated in a delicate environment, any surface treatment must fulfill the following requirements:

- Sufficiently low outgassing rate to avoid the degradation of the stringent ultra high vacuum conditions (10^{-11} mbar).
- Compatibility with thermal cycles of the bake-outs up to 350°C and high voltage performance.
- Temperature during treatment limited to 380°C to avoid damage to the weldings, which occurs at >400°C.
- Any coating must present good adhesion as basis to ensure that it does not peel or flake.
- Emissivity higher than 0.6 over the range of wavelengths from 6 μ m to 11 μ m (values obtained according to Wien's Displacement Law [17], corresponding to the range of temperatures from 20 to 250°C).

The following procedure was carried out in all the investigated treatments to assess their quality and ensure the fulfilling of the above mentioned requirements:

1. Samples of SS304L were prepared at CERN, following the same cleaning and surface preparation procedures as the internal surface of the vacuum tanks, which consisted of Net Inox cleaning [25] and electropolishing. Then the samples were sent to the respective companies where the treatments were applied.
2. Once the samples were prepared, they were sent back to CERN where emissivity measurements were performed by the colleagues from the group Vacuum, Surfaces and Coatings (VSC) with FTIR spectroscopy, using an infrared light with wavelengths from 2.5 μ m to 25 μ m. Each sample was measured several times, turning it randomly to measure the reflection with different angles of the incident light. The instruments used were:

- FTIR spectroscopy Bruker Optics Vertex 70.
 - Integrating sphere BRUKER-A562.
3. The vacuum compatibility of the samples that gave promising results was further tested at CERN by the colleagues from the group Vacuum, Surfaces and Coatings (VSC). A summary of the steps that must be followed before approving the installation of a new component in the LHC beam vacuum can be found in [22]. The approval is determined by comparing the results of the test with a set of acceptance thresholds based on previous experience, which are presented in the specification [24].

In the following, the investigated treatments will be thoroughly described, explaining the techniques employed and showing the results of the emissivity and, in the cases where the emissivity is adequately high, the results of the performed vacuum compatibility test too.

5.1.1 Multilayer coating

Description

The interest in multilayer coatings resides in the possibility of reflecting or absorbing the incident electromagnetic waves more strongly over a range of specified wavelengths. In other words, it allows to control the reflectance in the range of interest. This is achieved by building a coating with successive layers of different thickness and materials, in order to control the optical interference between the layers.

For simplification, the basic operating principle will be explained for a substrate coated with a single film, in which a beam impacts, as shown in Fig. 5.3 [15]:

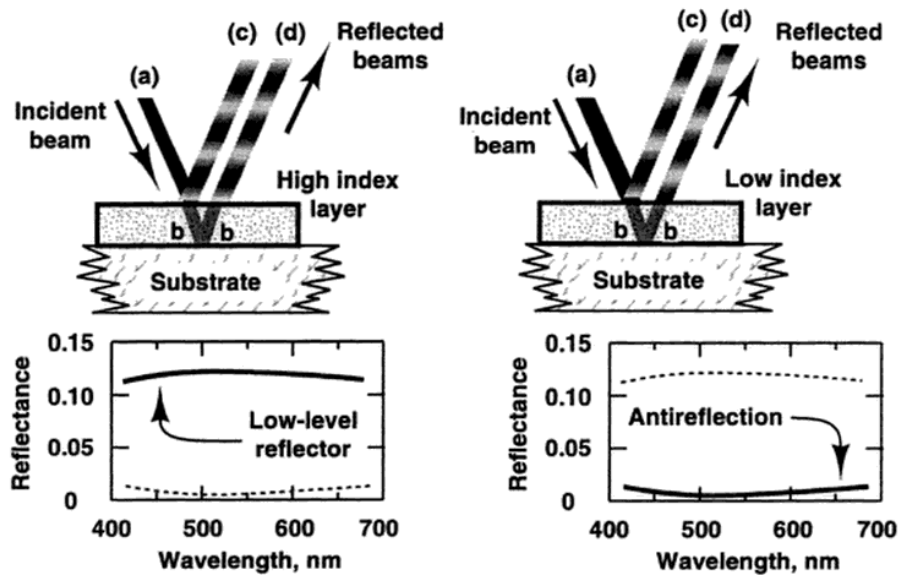


Fig. 5.3 Description of the multilayer interference in optical coatings.

- If the reflectance at a certain wavelength needs to be enhanced, the wave reflected at the vacuum-film interface and the wave reflected at the film-substrate interface must be in phase. That way a constructive interference is achieved, resulting in a higher reflectance in the film. Note that the spacing between the interfaces plays a key role in achieving both waves (reflected from the film and the substrate) to be in phase. Besides, the material of the film must be strategically selected to transmit to the substrate a certain percentage of the incident wave at the wavelength of interest.
- If the contrary effect wants to be achieved, that is reducing the reflectance, the wave reflected at the vacuum-film interface and the wave reflected at the film-substrate interface must be out of phase by 180° to create destructive interference.

The most widely used method of film deposition for multilayer coatings is the physical vapor deposition (PVD) [15]. Magnetron sputtering is a vacuum coating process that falls under the category of PVD. It allows the deposition of many types of materials, including metals and ceramics, onto different types of substrate materials [47]. Thanks to recent developments, this technique is widely applied in different sectors that require hard, corrosion-resistant, coatings, even with specific optical properties, which is of interest for this project [48].

The basic magnetron sputtering process is shown in Fig. 5.4. It consists of bombarding a target with energetic ions to strip atoms from its surface, which will be deposited onto a substrate as a thin film. The positively charged ions are generated in a glow discharge plasma of an inert gas such as argon. They are accelerated towards the target (cathode) to

strip atoms from its surface. Those atoms are ejected towards the substrate (anode), where they will condense forming a thin film. It must be highlighted that secondary electrons are also emitted from the target surface as a result of the impact of the inert gas ions, and these electrons play an important role in maintaining the plasma. Indeed, they are confined within a magnetic field created by a magnetron placed around the target to constrain them in the vicinity, which results in a dense plasma in the target region. This leads to higher sputtering rates and, therefore, more dense films deposited at the substrate [48].

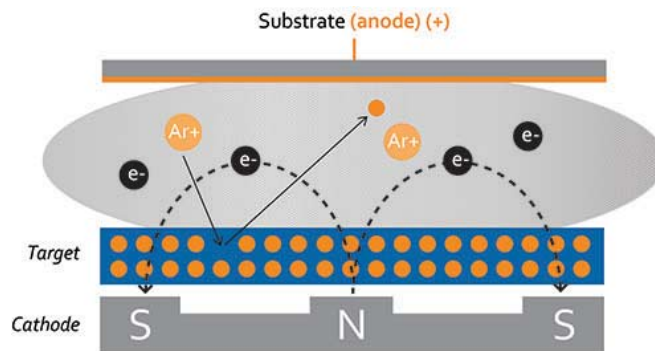


Fig. 5.4 Magnetron sputtering process [Denton Vacuum]

Investigated method

In the context of this research, companies that had expertise in the production of multilayer coatings were contacted. A special interest was raised by Polyteknik AS (<http://www.polyteknik.com>), a company based in Denmark, as they had patented the Poly CSP tubes: They consist of tubes used for concentrated solar power plants, which are coated with a pioneering multilayer structure so that an absorption of 95% in the solar spectrum and emissivity of 6% at 350°C are achieved. Thanks to this, they present extremely low heat losses due to thermal radiation [59].

Apart from that, Polyteknik AS is an international supplier of PVD systems. They perform from small scale R&D to high volume or large area depositions. For the vacuum tanks of the MKIs, they developed a multilayer coating, adapted to achieve a high emissivity over the required wavelengths (higher than 0.6 from 6 μm to 11 μm). It was a composition of Si, Al and Ti, applied in several steps to build-up layers of different refractive indexes. Dense layers were used to achieve long-term stability. They coated several samples which showed very promising results (see Fig. 5.5).

The main drawback was that, in order to apply the treatment in the vacuum tanks, the design of a suitable magnetron was needed to adapt it to the dimensions and curvature of the tanks. Their proposal consisted of mounting the tank vertically to avoid issues with

the axis alignment during the process. It would be moved into place using a fork-lift truck. The magnetron would be installed on the axis at the top of the tank, attached to a mechanism for moving it along the full length (height) of the tank. The estimated surface temperature of the stainless steel vacuum tank, during magnetron sputtering of the high emissivity coating, would be approximately 150°C , which is compatible with the temperature limitations imposed to avoid weld damage.

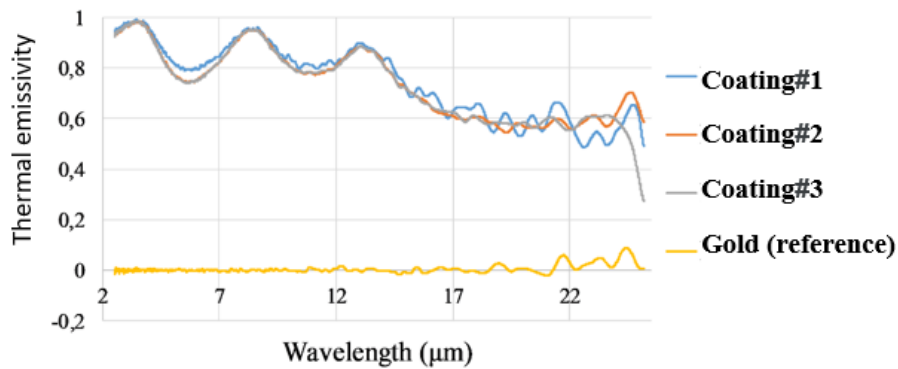


Fig. 5.5 FTIR spectroscopy of the SS304L sample with multilayer coatings.

Results of emissivity measurements

Three different samples were coated with multilayer coatings. Although all of them presented high enough emissivity (higher than 0.6 from $6\mu\text{m}$ to $11\mu\text{m}$), the design and manufacture of the complete coating system for the vacuum tank would require approximately six months of one of Polyteknik's key personnel. Apart from that, it must be taken into account that twelve tanks were to be treated, so this method was discarded for being highly time-consuming, and thus expensive.

5.1.2 Laser Engineered Surfaces

Description

The most important physical phenomena involving exchange of energy by thermal radiation takes place at a surface level. By changing the structure, particularly at a micro/nanometer scale, it is possible to obtain a desired functional performance. In [21], a summary of the functional properties that can be modified, together with the engineering technologies available to structure the surfaces is presented. With respect to the modification of the thermal characteristics, the application of laser techniques is reported for manufacturing low-cost and high-performance anti-reflection (AR) surfaces.

Indeed, it was found that by using a high-intensity femtosecond laser structuring technique, near perfectly reflective metals could be transformed to highly absorptive over an ultrabroad spectrum (from ultraviolet to terahertz) when producing an array of parallel grooves on the metallic surfaces [82, 76]. This investigation raised the interest towards the application of laser treatments to modify the highly reflecting internal surface of the MKI vacuum tanks.

Investigated method

A test campaign was started with the Materials And Photonics Systems Group (MAPS Group) of the University of Dundee. They had expertise on the use of nanosecond pulsed lasers to form homogeneously distributed, highly organized micro-structures. In particular, they had already produced large surfaces of copper substrates with absorbance of over 97% in the spectral range from 250 nm to 750 nm, and a broadband absorbance of over 80% between 750 nm and 2500 nm [69, 70]. In Fig. 5.6 the blackened part in the copper samples after the treatment can be clearly seen. The SEM images show the detail of the surface structure created at the micro/nano-scale level. The observed enhanced trapping and absorption of the electromagnetic radiation was attributed to the cumulative effect of the micro and nano-structures at the surface, micro-cavities, and oxide layer [70].

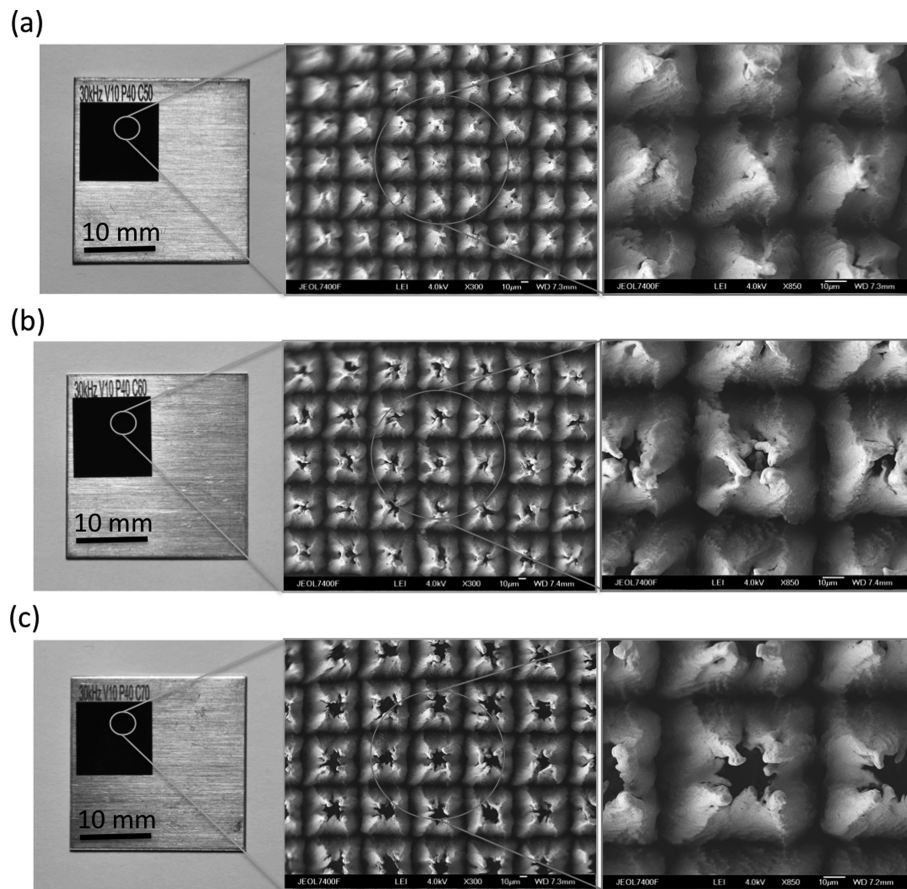


Fig. 5.6 Photographs and scanning electron microscope images of laser treated copper samples (The treated part corresponds to the black square in each sample [70])

The main advantage of this technique is that it was readily scalable and the employed laser source is industrially friendly and highly adaptable. The surface emissivity could be changed for the required range of wavelengths by controlling the following parameters of a laser:

- Laser Wavelength
- Energy and power
- Spot size and shape of beam
- Pulse length

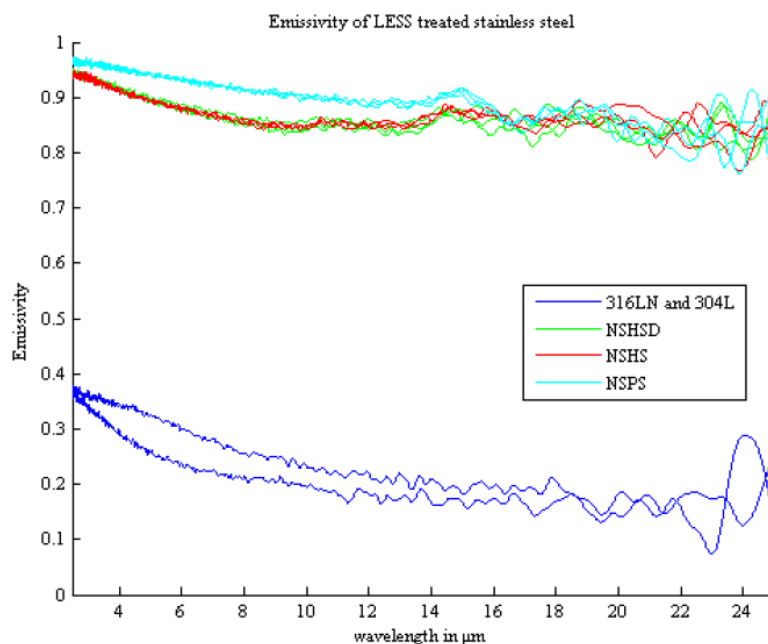


Fig. 5.7 Emissivity measurements of the LESS treated SS304L sample.

Results of emissivity measurements

A total of eight samples were LESS treated and then tested. The emissivity measurements of the latest and most promising samples are plotted in Fig. 5.7. The difference between them depends upon the laser parameters employed in each case. It can be appreciated that all the treated samples showed an emissivity higher than 0.6 in a broad range of wavelengths. The best performing samples had an emissivity exceeding 0.95 in the spectral region between $2.5\mu\text{m}$ and $15\mu\text{m}$. Furthermore, high performance stability of the LESS surface was confirmed after thermal aging studies at 320°C for 96 hours [85].

Within the tested samples, the most interesting one was NSHS because it was much faster to produce than the others. In particular, if the parameters for NSPS were used, it would take up to 9 months to treat one tank, while with the NSHS parameters this could be reduced to less than 3 months. These estimates assume that only one laser is used at a time.

Obviously, for a large operation, a number of laser systems can be used in parallel to substantially reduce the processing time. The fact that the diameter of the tanks was very large relative to the dimensions of the whole laser system, would allow for up to 3 systems to enter a tank at the same time.

Nevertheless, there were 12 tanks to be treated, so even considering the best scenario in which the NSHS was applied, with 3 lasers working in parallel, the total time to process all of them could be in the order of one year.

Another drawback was that, for adapting the laser systems to the large scale of the project, it would be necessary to purchase new equipment that would substantially increase the costs:

- A fibre laser system: £20k.
- A 3D optical scanning head and optics: £40k.
- A simple carriage system comprising a motorize stage to hold and move the 3D optical scanning head inside the tank (to be designed at CERN).

To the cost of the equipment, it had to be added the human resources (salaries+travels). All in all, the total cost would be up to £180k.

Considering all the reasons above, it was decided to discard this method and keep investigating, aiming at an alternative which is cheaper and faster.

It is worth mentioning that, although this treatment was discarded for the MKI vacuum tanks, a collaboration between CERN and the University of Dundee was established for treating the internal surface of the SPS and LHC beam pipes. In this case, the laser structuring was focused on reducing the secondary electron yield (SEY), a parameter that indicates the accumulation of electrons inside the vacuum pipes, occurring in high energy accelerators operating with positively charged particles due to the photoemission and secondary emission, leading to an exponential electron multiplication. If it is sufficiently strong, it can seriously affect the operation causing heat load on the chamber's wall, pressure rise, or even the deterioration of the beam quality due to the electromagnetic forces exerted on beam particles [61]. Thanks to the LESS treatment, the SEY has been greatly reduced [66, 62].

5.1.3 Chemical etching

Description

Chemical texturing is among the surface engineering methods mentioned in [21] to change the structure of the surfaces in order to modify the functional properties. It consists of selectively applying chemical reagents to a surface to remove material in specific regions in order to produce texturing. Normally, the way to do this is by immersing the material in a chemical etchant which, after leaving it for a controlled time, results in a microscopic electrochemical cell action, equivalent to that responsible for corrosion or chemical dissolution of a metal.

Investigated method

At CERN, within the group Vacuum, Surfaces and Coatings (VSC), which provides services related to the design, operation, and maintenance of the vacuum systems for the

accelerators and detectors of the whole complex [Vacuum and group at CERN], investigations based on chemical etching were ongoing to obtain porous and/or rough surfaces on stainless steel, aiming at reducing the SEY and decreasing the emissivity [71]. This was closely followed as it was potentially applicable to the MKIs.

Among the different approaches that were tried, one gave promising results. It was based on the investigation shown in [49]: They aimed at improving the oil retention of stainless steel 304, and for that, they diluted the samples in Aqua Regia to form hierarchically-porous surface structures. After the treatment, the surface became highly porous. The pore size was controlled over a certain range by adjusting the voltage applied during the etching process.

The same method was applied to SS304L samples in the chemistry lab at CERN. The setup is shown in Fig. 5.8.

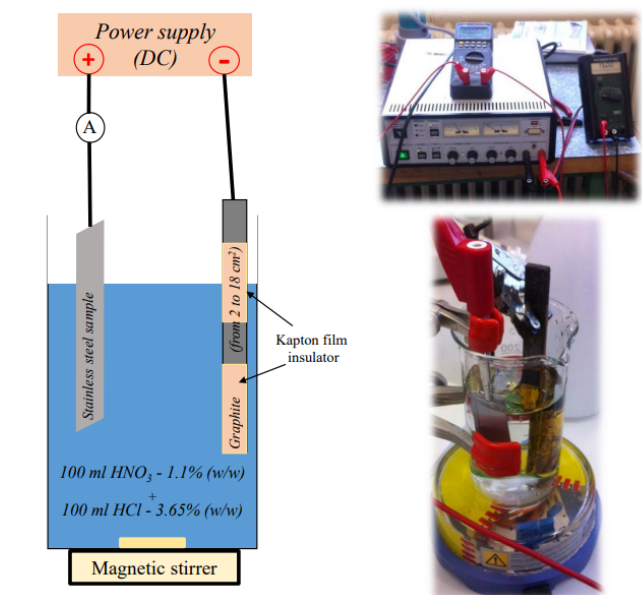


Fig. 5.8 Chemical etching process [71].

Results of emissivity measurements

After treating the samples, a homogeneous, porous and rough surface was achieved, with a significant increase of the emissivity over a wide range of wavelengths. The improvement can be seen in Fig. 5.9 by comparing the measured emissivity of the sample before and after the treatment.

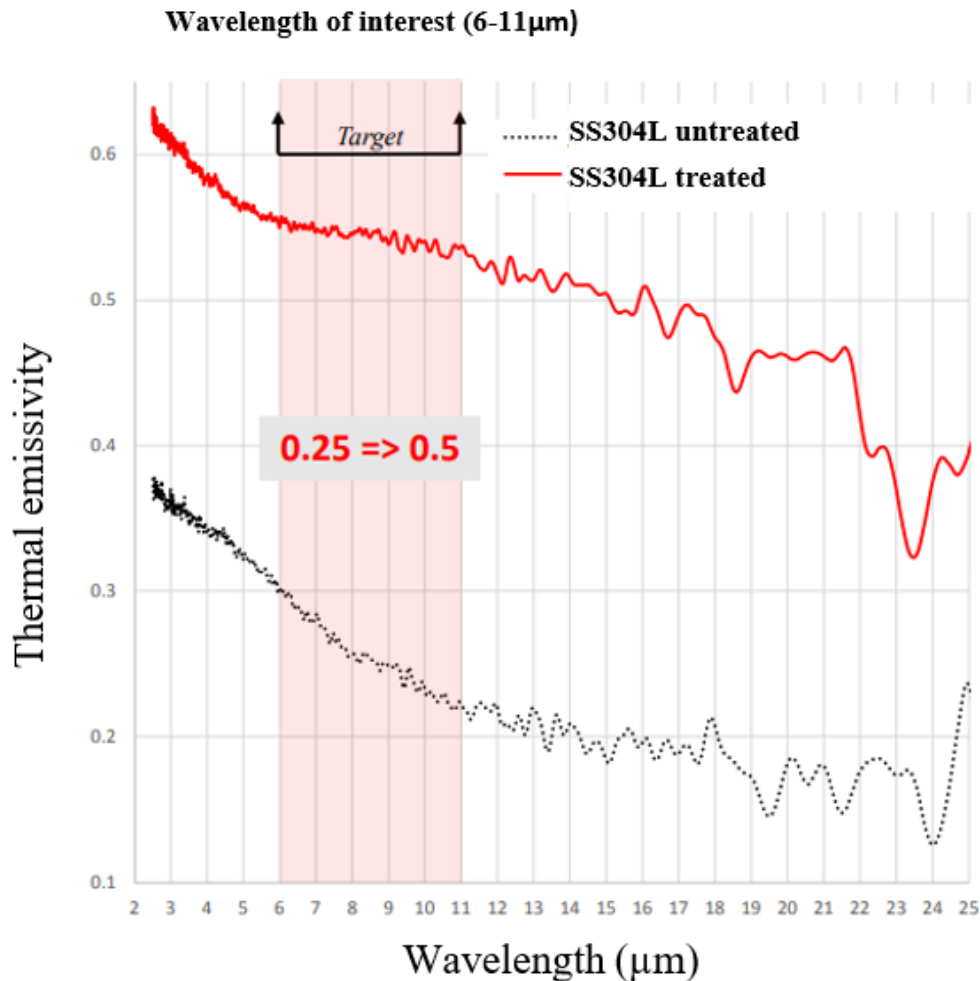


Fig. 5.9 Emissivity measurements of the SS304L with chemical etching [71].

The emissivity could be further increased over the desired wavelengths by optimizing the method. Several iterations were needed to find the optimum diameter of the pores and the roughness of the surface, which depended on the acid type and concentrations of the chemical bath, the treatment time, DC voltage, agitation, temperature, the use of pulsed currents. . . However, the high workload at that time and the priority of other ongoing projects made it difficult to continue with the investigation. Besides, although this method was a good option for treating components of reasonably small dimensions, as they could be immersed in the chemical bath, this might not be easily applicable to the MKI vacuum tanks.

5.1.4 Flame spray

Description

Thermal spray is a coating process in which a material in the form of powder, wire, or rod,

is heated to a molten or semi-molten state and then accelerated and propelled onto a surface. Upon impact, a bond forms with the surface, with subsequent particles causing thickness buildup [31].

The main interest of coating the MKI vacuum tanks with a thermal spray process resided in the easy and feasible application, as the tanks have large enough diameter for the torch or gun to fit inside. Besides, the wide range of materials that can be used (generally any material that melts without decomposing) gave good chances of finding an appropriate mixture to increase the emissivity. Last but not least, the ability of most thermal spray processes to apply coatings without significant heat input directly into the surface was important to meet the temperature limit requirement imposed by the potential weld damage of the vacuum tanks. This allows to coat, at limited temperatures, surfaces while depositing materials with very high melting points, as is the case for most ceramics, which are characterized by high thermal emissivities [31]. Depending on the energy source used for heating and propelling the coating material, the thermal spray processes can be classified into three major families [1]:

- Flame spray: Use of combustion gas as heat source to melt the coating material.
- Plasma spray: Use of electrical energy provided by a plasma or an electric arc.
- Cold spray or supersonic particle deposition: Use of the kinetic energy provided by a supersonic jet of compressed gas to accelerate the particles.

Within the different thermal spray processes, the flame spray was considered the most suitable for application to the MKI vacuum tanks. The operating principle consists of melting the coating material with the use of a combustible gas. The temperature of the flame needs to be adapted to the melting temperature of the coating materials of interest. It can be adjusted by selecting a suitable fuel gas, the oxygen-to-fuel gas ratio and pressure [74]. A representation of the flame spray process is shown in Fig. 5.10.

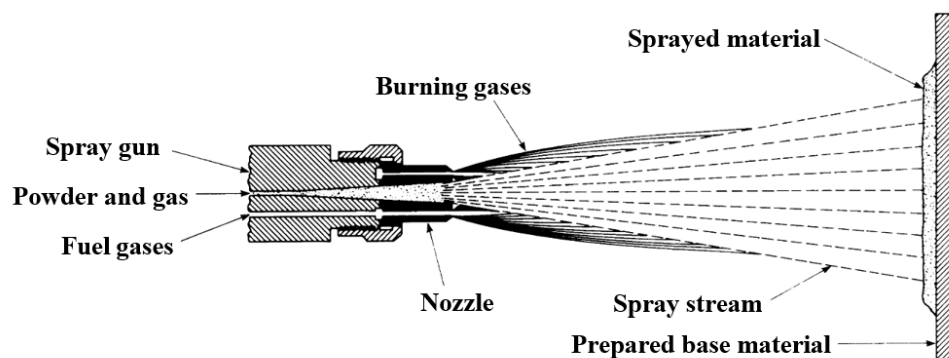


Fig. 5.10 Cross sections of typical flame spray process with powder [74].

Investigated method

2DHeat Limited (<https://www.2dheat.com>) is a research company based in the UK with expertise in electric heating elements. They patented surface coatings for their electrical heating elements based on thermal spray applications of metal oxides, which showed high emissivities and very uniform heating across long lengths. These coatings had already been used in HV/UHV applications. Due to their vast expertise in the field of thermal spray processing, they were contacted to investigate whether they could adapt their techniques for treating the MKI vacuum tanks.

Indeed, they coated three different samples with flame spray by applying short, quick bursts of oxy-acetylene spraying, seeking to keep the temperature of the test-piece below the critical temperature imposed to avoid weld-damage. The characteristics of each of the samples are the following:

- Coating A: Prepared by flame spraying a mixed metal powder, Inconel 600, onto the SS304L sample. This would be the lowest cost option.
- Coating B: Prepared by flame spraying a highly pre-oxidised sample of Inconel 600. This consisted of a double-stage process; firstly pre-oxidation of the Inconel 600 alloy, followed by isolation and drying. Finally, the flame-spraying of that pre-oxidised powder is applied to the 304L test piece. The sample was visibly 'blacker' than Sample A.
- Coating C: As with Sample B, it was produced using a 2-stage process, also consisting of flame spraying pre-oxidised Inconel 600. However, in this case the Inconel 600 was subjected to a lower degree of oxidation. This gave the visually 'blackest' deposition of all 3 samples.

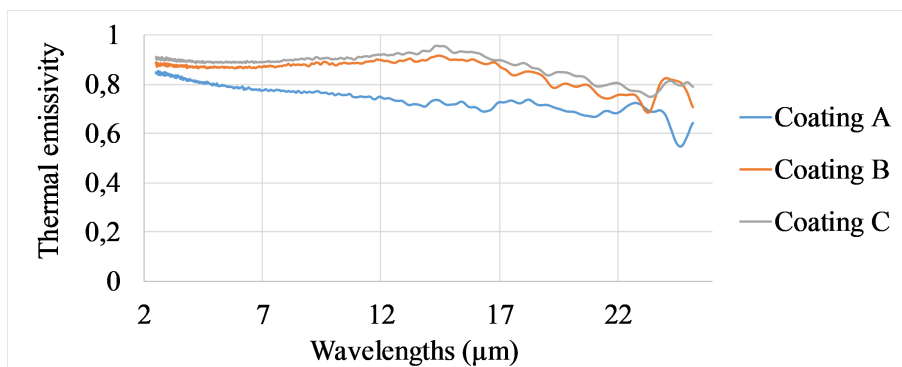


Fig. 5.11 Emissivity measurements of the SS304L samples with flame sprayed coatings.

Results of emissivity measurements

The thermal emissivity measurement of the three coated samples is shown in Fig. 5.11. As it can be appreciated, all of the flame sprayed samples have a thermal emissivity above the required 0.6 over all the measured wavelengths. Since the coating C has the highest emissivity (as it was expected from the visual inspection), it was selected for testing of the vacuum compatibility.

Results of vacuum compatibility test

The materials that will be placed in environments under ultra high vacuum conditions must have very low outgassing rate at the working pressure, and be tolerant to the thermal bake-outs.

In order to determine if the coatings are vacuum compatible, a Residual Gas Analysis (RGA) is performed to detect sources of contamination. The signs of contamination are [24]:

- Anomalous presence of hydrocarbons, which is generally attributed to errors in the cleaning procedure or post-cleaning pollution.
- Presence of materials that are not suitable for vacuum applications such as polymers, glues...
- Higher than expected CO and CO₂ outgassing indicating the presence of carbonized elements.
- Presence of any chemical element or compound usually not present in the residual gas phase, for example, F and Cl (from issues with etching and cleaning), K and Na (from manipulation), P and S (from issues with electrolytic treatments).

To determine from the RGA analysis if a material is vacuum compatible, the obtained characteristic mass peaks are first normalized to the usual dominant gas peak, being the H₂ in the case of a baked system, which corresponds to 2 amu. Then it must be ensured that the normalized values are below threshold limits based on extensive experience [53], which are the following [22]:

- The mass peaks of CH₄, H₂O, and CO, which corresponds to 16, 18, and 28 amu respectively, have to be at least 10 times lower than the mass peak at 2 amu.
- The main peak of CO₂, which is 44 amu, has to be a factor of 20 lower than the peak at 2 amu.

- The heavy-hydrocarbon mass peaks over 50 amu must have intensities 1000 times smaller than the mass peak at 2 amu.

The RGA scan of the pre-oxidised Inconel 600 flame sprayed coating is shown in Fig. 5.12, with the acceptance limits indicated in yellow. As it can be appreciated, the obtained values were within the specified limits so it can be concluded that this coating was vacuum compatible, and a potential candidate as selected treatment for the vacuum tanks.

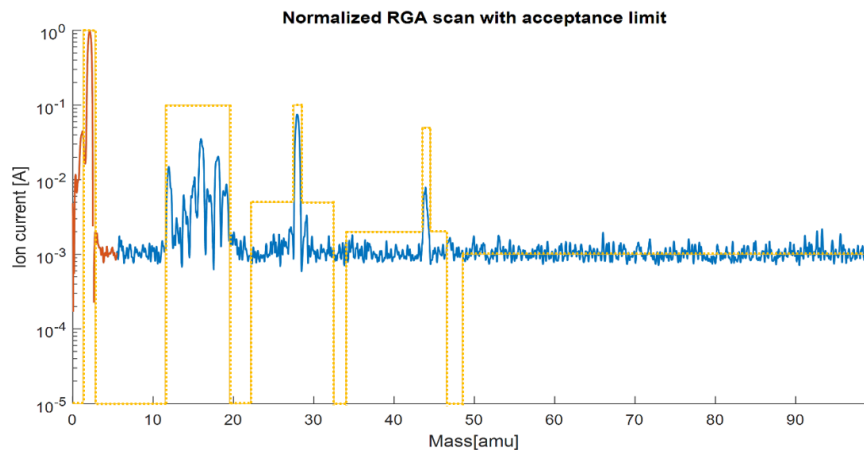


Fig. 5.12 RGA scan normalised to mass peak 2 amu (red and blue) and acceptance thresholds (yellow) of Inconel 600 flame sprayed coating of SS304L (sample C). *Courtesy: J.A. Li Hellstrom*

5.1.5 Plasma spray

Description

Apart from the flame spray, plasma spray was also considered a potential treatment for the MKI vacuum tanks. The principal difference between them is given by the melting temperature of the powder. In the flame spray, the temperature is limited by the enthalpy of the chemical reaction that leads to the combustion of gases such as acetylene, propane, butane, generally in the presence of air or oxygen, while the plasma spray is limited only by the amount of electrical energy supplied [44]. In [1], an extensive recompilation is presented of the published experimental work performed with different thermal spray processes. They include a graph of Temperature vs velocity for the different processes, where it can be seen that the temperatures achievable with flame spray are in the order of 2000-3000 K, while with plasma spray they are higher than 4000 K, going up to 24,000 K (see Fig. 5.13). The main interest in operating at high temperatures resides in the fact that it can be used for spraying materials with higher melting points.

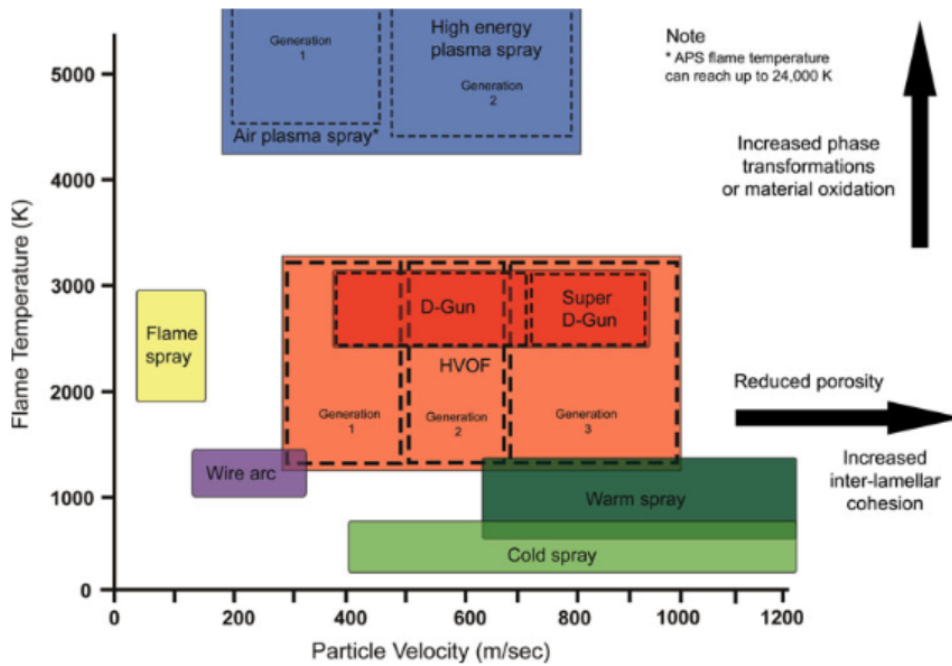


Fig. 5.13 Classification of thermal spray processes according to particle velocity and flame temperature [1].

A plasma spray torch is shown schematically in Fig 5.14 [1]. A gas, usually argon, flows between a tungsten cathode and a water-cooled copper anode. An electric arc is initiated between the two electrodes using a high-frequency discharge and then sustained using DC power. The arc ionizes the gas, creating a high-pressure gas plasma. The resulting increase in gas temperature, which may exceed $30,000^{\circ}\text{C}$, causes an increase in the volume of the gas and, hence, its pressure and velocity as it exits the nozzle. This high-temperature, high-velocity plasma gas stream heats up and accelerates the coating powder towards the surface.

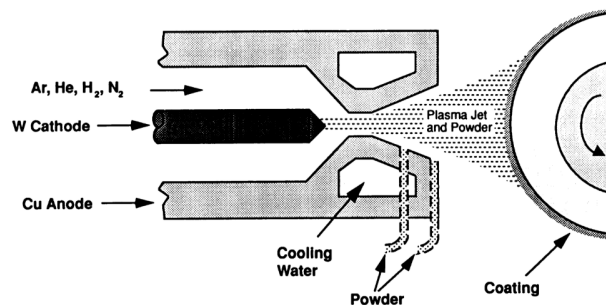


Fig. 5.14 Plasma spray process. Courtesy of Praxair Surface Technologies, Inc. [74].

Investigated method

Although 2DHeat Limited were not working with plasma sprayed coatings, they collaborated with another company, Engineered Performance Coatings Ltd (<https://www.ep-coatings.com/>), based in Cardiff, which had vast experience in the field.

They coated one of the samples with 100% fine alumina.

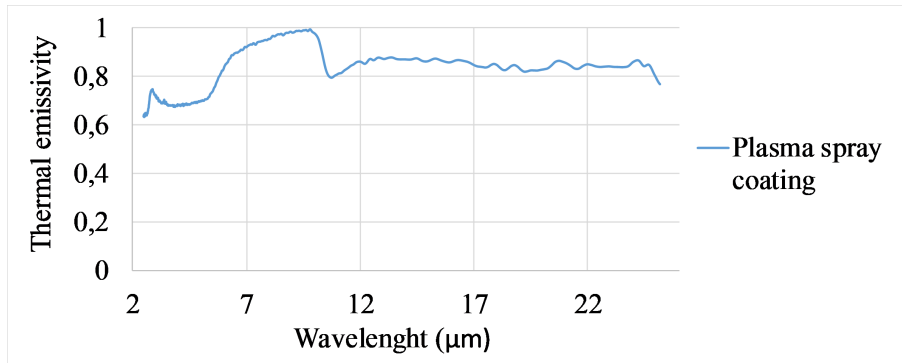


Fig. 5.15 Emissivity measurements of the SS304L with Al_2O_3 sprayed coating.

Results of emissivity measurements

The measured thermal emissivity was also significantly above 0.6 over all the measured wavelengths. Given the promising results, this coating was also further tested for the vacuum compatibility.

Results of vacuum compatibility tests

As in the case of the flame sprayed coating, an RGA scan was performed for the plasma sprayed 100% fine alumina coating. The results are shown in Fig. 5.16, with the acceptance limits indicated in red. As it can be seen, the obtained values are also within the specified limits so it can be concluded that this coating is vacuum compatible too.

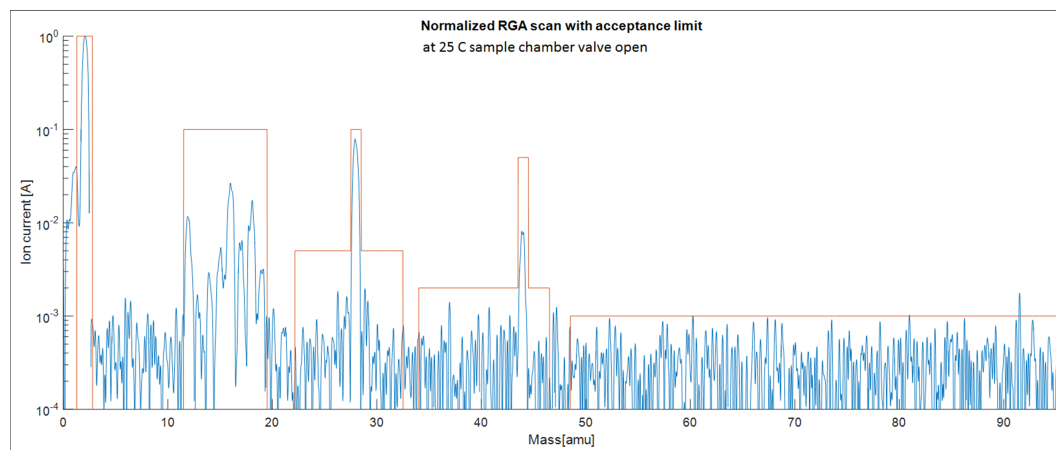


Fig. 5.16 RGA scan normalised to mass peak 2 amu (blue) and acceptance thresholds (red) of 100% fine Al_2O_3 plasma sprayed coating of SS304L sample. Courtesy: A.K. Riihimaki [60].

5.1.6 Summary of emissivity studies and conclusions

After the test campaign launched for finding a suitable technique to increase the thermal emissivity of the internal surface of the vacuum tanks, two coatings based on thermal spraying processes were found to be best. Even though the other investigated treatments showed remarkable increase of the thermal emissivity over the required range of wavelengths, their application in the tanks, given the curved shape and the big dimensions, was highly time consuming and in some cases required the design of new tools and equipment especially adapted to the dimensions of the tanks, which would remarkably increase the total cost. For those reasons, the multilayer optical coating and the LESS treatment were discarded.

The thermal spray was a suitable technique for the tanks, and the vacuum compatibility of the coated samples was confirmed with a test campaign. However, all these studies took a long time due to the high workload in the vacuum lab, summed with the fact that there were ongoing projects considered as higher priority. Not only that, but the test bench used for the vacuum compatibility test was unusable for some time as a vacuum valve had to be replaced. For all these reasons, the tests of the flame sprayed sample were only finished by May 2017, while the results of the plasma sprayed sample were not received until December 2017.

As has been commented, complementary measures were being studied in parallel to help further reduce the temperature of the yokes. Note that even with a high emissivity coating, the first three yokes would still be above the Curie temperature according to simulations (see Fig. 5.2). Hence, high Curie temperature ferrite would have been required for these three yokes. By the time the results of the vacuum test were finished, some of the alternative approaches studied were showing promising results even without the need of increasing the

emissivity. For this reason, it was decided not to start treating the tanks immediately, but keep investigating other approaches, which will be further introduced in the following sections.

5.2 Removing the bake-out jackets

The heat generated in the rings and yokes is radiated to the internal surface of the vacuum tanks, and then evacuated by convection and radiation to the natural air flow in the tunnel. However, this is considerably limited due to the bake-out jackets that surround the vacuum tanks, which are a high thermal resistance. Removing them would improve the heat extraction. To assess the improvement, a simulation was performed with and without the jackets modelled, for the nominal beam parameters of HL-LHC. The expected temperatures in both scenarios are shown in Fig .5.17:

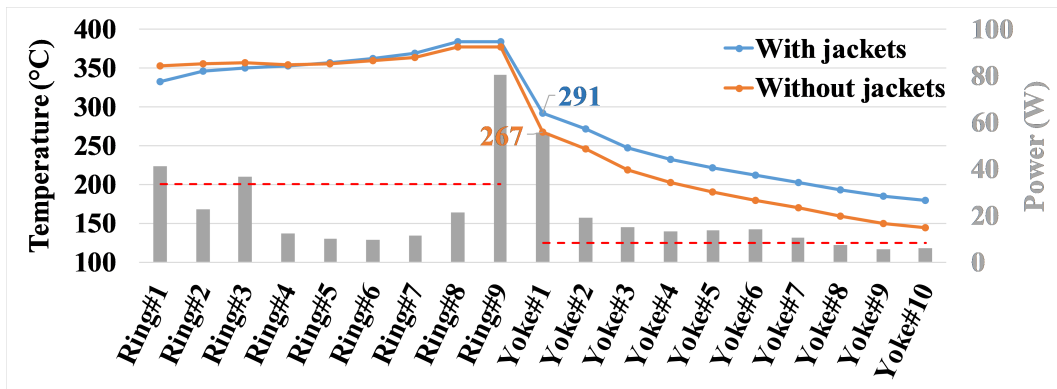


Fig. 5.17 Temperatures predicted with and without bake-out jackets. Dashed red line: Curie temperature of ferrite types CMD5005/8C11 and 4M2 used in yokes and rings respectively. Model 3 of power deposition for HL-LHC. Total power: 616W.

Without the jackets it would be difficult to perform a proper bake-out in-situ, as their installation is very complex once in the tunnel due to space constraints. However, this operation has never been required to date, so considering the limited risk that removing them implies, and the benefits that such a simple measure brings to the reduction of the temperatures, it was decided to remove them for HL-LHC operation. Note that, although the reduction of the temperature of the yokes is remarkable, they are still above the Curie point, so complementary measures are needed. Besides, while the effect upon the temperature of the yokes is evident, the rings are not remarkably affected as they are very small with regard to the dimensions of the vacuum tank, so the radiative exchange between them is negligible.

It is interesting to obtain the relation between the temperature of the first, hottest yoke, with and without the jackets, for the different LHC operating scenarios. For that, simulations

have been performed for both cases and different total power loss. Results are shown in Fig. 5.18. Each point corresponds to the maximum temperature of the first yoke for the same total power. The data have been fitted to a linear regression, being the value of R-squared very close to 1, which indicates a reliable fit.

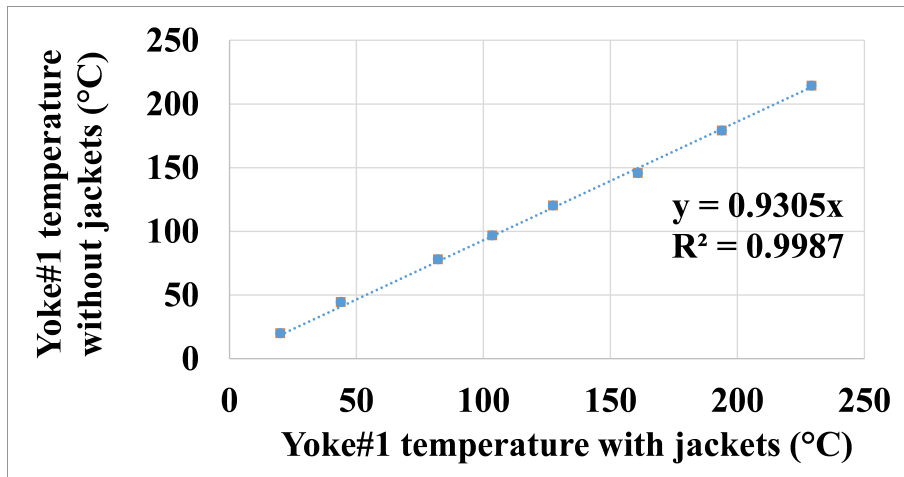


Fig. 5.18 Relation between the maximum temperature of the first yoke with and without jackets. *Model 3 of power deposition.*

As shown in Fig. 5.18, the first ferrite yoke temperature decreases by 7%, for a given power deposition, when the jackets are removed. Given this benefit, as commented, the bake-out jackets will not be installed for future HL-LHC operation, and the simulations regarding alternative cooling schemes will not include the jackets in the model. Furthermore, as a precautionary measure, they were removed from the MKIs with the highest measured temperatures for much of Run2.

5.3 Cooling down the ferrite yokes

As the kickers are operated with high voltage and high currents, a liquid cooling system was initially discarded due to the fatal consequences of a leakage in the UHV environment. In addition, direct liquid cooling of the yokes was not desirable as they are at pulsed high voltage. However, liquid cooling was found to be the most efficient option after studying the passive cooling techniques mentioned in the previous sections, as they will not reduce the temperature of the rings and all yokes below the Curie thresholds for HL-LHC operation. The investigation was then oriented to the implementation of an active cooling system, which is challenging due to the conditions already mentioned.

One proposed design was based on that implemented in the SPS extraction kicker magnets, named MKEs [73]. In that case, for preventing the overheating of the yokes, electrically insulating cold plates were placed on the top and bottom surfaces of the ferrites (note that the yokes have a C-shape), and a water-cooling circuit was attached at one of the extremes of the plates as shown in Fig. 5.19. To ensure a good heat exchange between the ferrites and the plates, a suitable mechanical pressure contact was achieved by means of a spring-loaded pad, applying a constant force of 200 N.

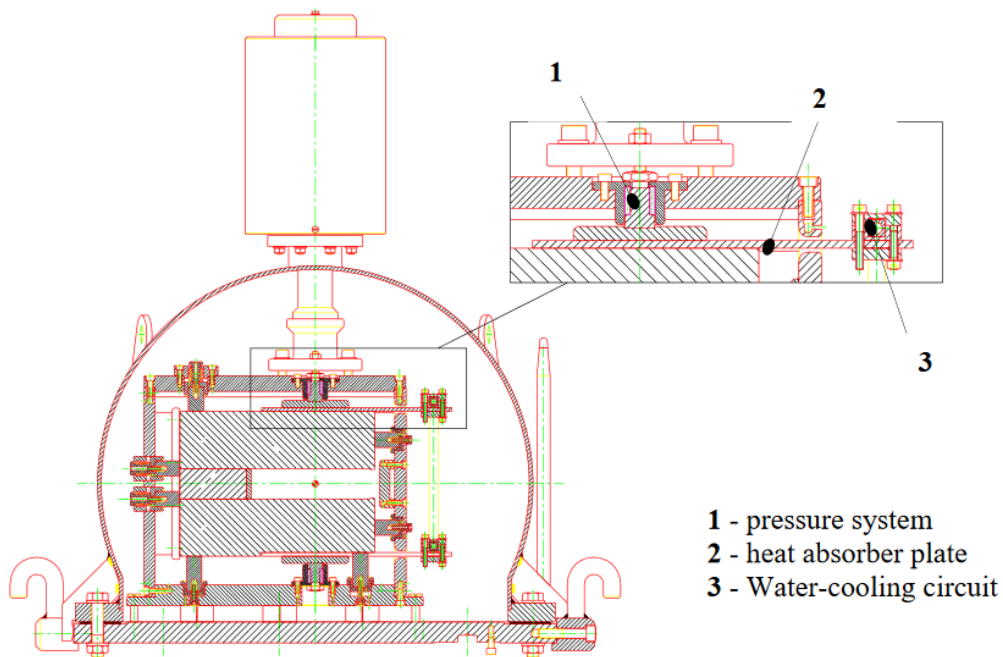


Fig. 5.19 Cross-section of an MKE magnet with details of the cooling system [73].

Based on the successful performance of this configuration, a similar design was considered in the MKIs. However, in the MKIs, the ferrite yokes of each cell are shorter (74,3 mm instead of 230 mm) and there is less space available in the surrounding tanks due to the presence of components very close to the yokes. This complicated greatly the installation of a cooling system based on cold plates.

First of all, a suitable material was selected for the MKIs cold plate. The following requirements need to be fulfilled:

- High thermal conductivity to ensure a good heat extraction.
- Electrical insulation as the ferrite yokes are pulsed at high voltage.
- Good mechanical properties to withstand the pressure applied in the contact.

- Low outgassing rate for vacuum compatibility.

This complicated the choice as metallic components are usually the best option, due to their good thermal and mechanical properties. In the end, the materials that were considered for this application were beryllium oxide, aluminium nitride and alumina, which are high thermal conductivity ceramics with good electrical insulation. Among them, although the beryllium oxide presented the highest thermal conductivity (approximately $260 \text{ W/m}\cdot\text{K}$ compared to the $170\text{-}190 \text{ W/m}\cdot\text{K}$ and $36 \text{ W/m}\cdot\text{K}$ of the AlN and Al_2O_3 respectively), it was discarded as its dust particles are toxic and their inhalation may cause inflammation of the lungs. The best choice was hence the AlN as its thermal conductivity is far superior to that of alumina [64].

Once the material was selected, preliminary decisions regarding the configuration of the cooling system needed to be further developed. Taking into consideration the mentioned space constraints, three different alternatives for providing the heat path between the cold plates and the cooling pipes were proposed. An image of each of the models is shown below, followed by a brief description:

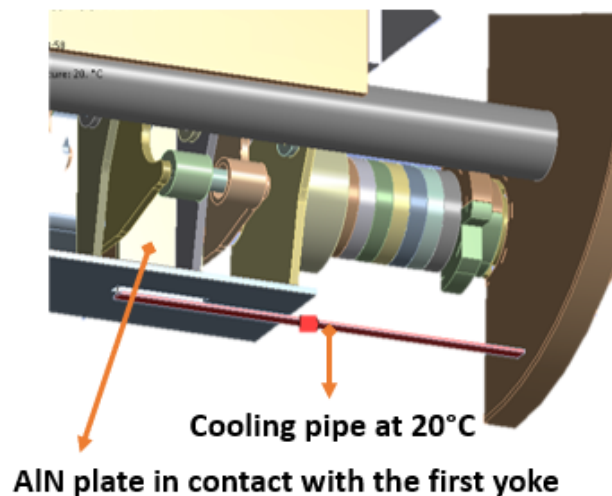


Fig. 5.20 *Case a*: Cold plate pressed against the yoke with cooling pipe connected at the bottom surface of the plate.

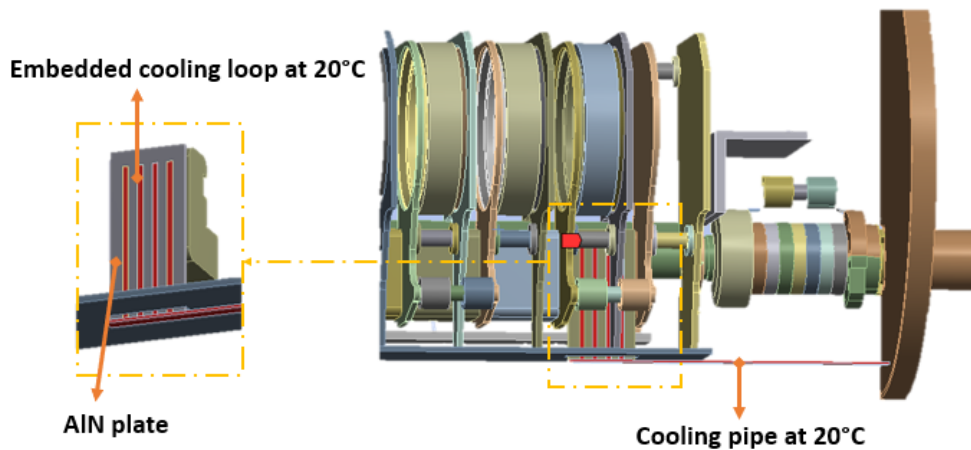


Fig. 5.21 *Case b*: Cold plate pressed against the yoke with cooling loop embedded

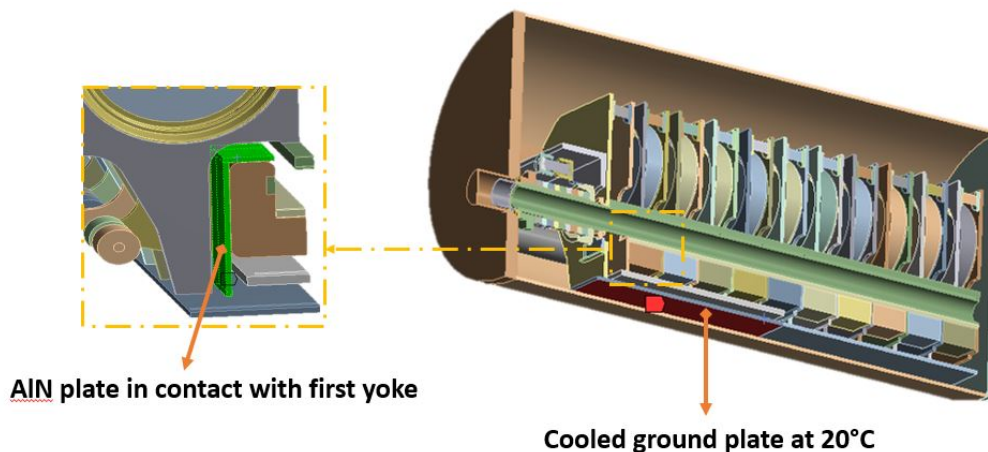


Fig. 5.22 *Case c*: Cooled horizontal ground plate.

- *Case a*: A hole is machined in the horizontal ground plate so that the AlN plate can pass through it. The plate is connected to the cooling pipe at the bottom surface. The heat transferred from the yoke to the plate is evacuated by thermal conduction to the cooling pipe. Note that for simplification, instead of modelling the water as a fluid and then introducing the convection coefficient between the wall of the pipes and the water (as it is conventionally done), they were modelled as a solid block, and a constant temperature of 20°C was imposed. This is supposed to be a good approximation, as the LHC counts on a circuit of demineralised cooled water with sufficient cooling capacity, and in case of necessity, it exists the possibility of using chilled water.

- *Case b*: It is similar to the previous case. The difference is that the cooling pipe ends in a loop embedded in the plate to ensure a lower and more uniform temperature distribution in the plate.
- *Case c*: A temperature of 20°C is defined at the bottom surface of the horizontal ground plate (highlighted in red), to simulate the effect of cooling the plate. This would be done by means of a cooling loop embedded in the ground plate. The loop has not been modelled for simplification. AlN plates are directly in contact with the ferrite yoke so that the heat can be properly extracted and conducted through them to the cooled ground plate.

Simulations were performed for the power expected in HL-LHC operation. The maximum temperature obtained in the first yoke for each case is presented in the following Table 5.1:

	Reference case (no cooling)	a) AlN plate without embedded pipes.	b) AlN with embedded pipes	c) Cool down ground plate at 20°C
Maximum Temperature Yoke#1	267	159	110	113

Table 5.1 Maximum temperature of the first yoke for different configurations of a cooling system based on cold plates attached to the first yoke. *Model 3 of power deposition. Total power: 616 W*

According to the results, the temperature of the first yoke can only be limited below the Curie threshold in cases *b* and *c*. Otherwise, the heat extraction is not efficient enough. However, it was decided to discard option *c* for the following reasons:

- It is not advisable to cool down a large surface with several components pulsed at HV nearby. This would change the capacitance of the nearby HV surfaces, which could influence the pulse shape.
- Good contact between the yokes and the AlN plates, as well as between the AlN plates and the cooled horizontal ground plate must be ensured to permit the heat to flow without significant thermal resistance. However, this can be critical during the assembly due to the brittleness of the yokes and the AlN plates.
- To ensure a low uniform temperature in the horizontal ground plate, two options were considered:
 - Embedded pipes: First of all, it would be necessary to machine the path for the pipes in the ground plate, and then ensure a good contact between them, ideally by means of diffusion bonding with a Hot Isostatic Pressing (HIP) technique [52]. Nevertheless, this would be highly time consuming because the horizontal ground

plate serves as support for all the vertical ground plates, which in turn hold the rest of the magnet structure. As a consequence, the magnets would have to be entirely disassembled, which is a critical and time consuming step due to the precision required in the alignment. In addition, as the MKIs have been in the LHC they are mildly radioactive, so it is advisable to minimize work on them.

- Cold plate contact: Even though this option would not imply the disassembly of the whole magnet, it also presents mechanical difficulties due to the lack of space and the presence of holes in the ground plate for allowing the connection of the HV feedthrough to the coaxial cables. This hole coincides with the hottest region where the first yokes are located (see Fig. 5.23), which would limit the surface to be cooled, degrading the effectiveness of heat extraction.

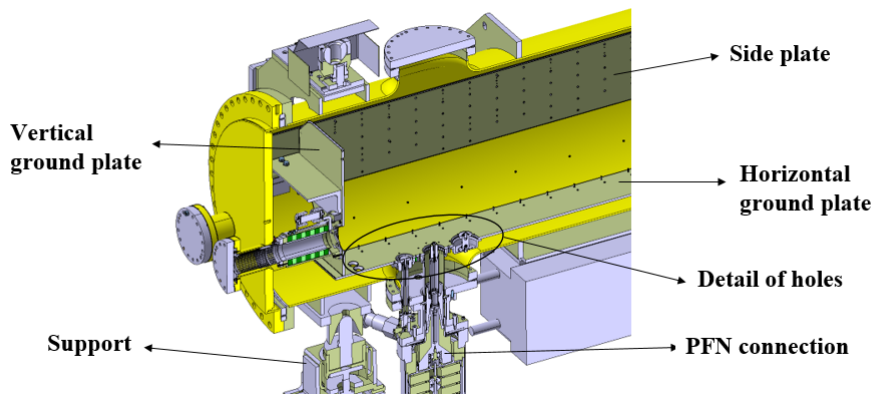


Fig. 5.23 Detail of the holes in the ground plate for the connection of the HV feedthrough to the coaxial cables.

A thorough study was performed for case *b* to optimize the design and further investigate the pros and cons of this method. In what follows, the different decisions made regarding several aspects of the design will be justified:

Contact between cold plate and cooling pipes

The predictions shown in Table 5.1 were obtained assuming a thermal conductance in the contact between the cooling pipes and the cold plate of $10,000 \text{ W/m}^2\text{K}$, which is a reasonable value in the case of applying a high conductance bonding method or high pressure. The latter could be achieved by means of spring loaded pads, as was done in the MKE magnets [73] (see Fig. 5.19). However, for the MKIs, the geometry of the cooling loop is limited by the available space, together with the brittleness of both the yokes and the AlN plates, can complicate the mechanical assembly, leading to increased chances of cracking. For this reason, a high conductance bonding method would be a better solution.

Use of chilled water

Although the implementation of an active cooling system inside the MKI tank was not considered at the beginning of the project, water cooling of the outside of the vacuum tanks was being considered, so the installation of water inlets and outlets was requested in both LHC injection regions in order to be ready. Upon approval, the following changes were implemented during LS1 [10]:

- Installation of 2 demineralised water inlets and outlets in both injection regions, named RA23 and RA87, adjacent to the injection kicker magnets MKIMA.
- Implementation of a system to reduce and stabilize the demineralised water to 20°C +/- 2°C by means of a heat exchanger on the chilled water supply.

Thanks to the installation of the heat exchanger, even though the nominal water temperature was set to 20°C, it could operate at lower temperatures. To assess the benefit of this, a simulation was also performed setting the temperature of the cooling pipes at 15°C.

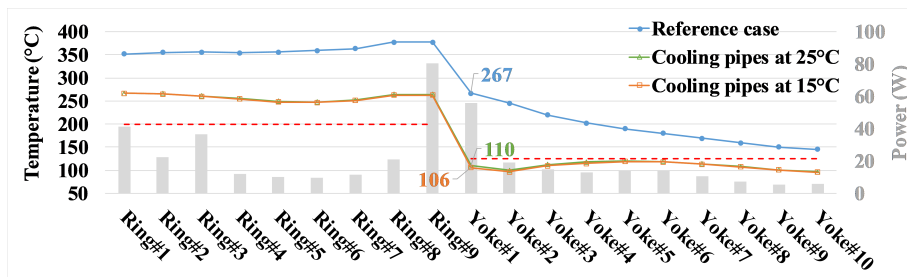


Fig. 5.24 Temperature for case *b* with embedded cooling pipes at 15°C and 25°C in contact with only the first ferrite yoke. Dashed red line: Curie temperature of ferrite types CMD5005/8C11 and 4M2 used in yokes and rings respectively. *Model 3 of power deposition for HL-LHC. Total power: 616W.*

As it can be seen, the gain obtained with chilled water versus water at 25°C is negligible: Both curves overlap.

Number of yokes to be cooled

The obtained temperatures shown in Fig 5.24 indicate that cooling down the first ferrite yoke with cooling pipes at 25°C is enough to reduce its temperature below the Curie point. However, downstream ferrite yokes would be very close to the threshold. Indeed, Yoke#5 even reaches 120°C, so it is desirable to design in a higher safety margin.

One solution would be to cool down other yokes apart from the first one. In order to obtain the best configuration, several simulations were performed with the cold plates attached to various yokes. The most promising results are plotted in the following graph:

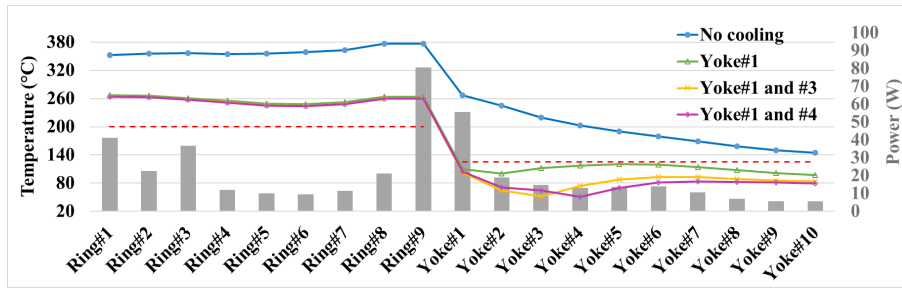


Fig. 5.25 Temperature for case *b* with cold plates attached to various yokes. Dashed red line: Curie temperature of ferrite types CMD5005/8C11 and 4M2 used in yokes and rings respectively. *Model 3 of power deposition for HL-LHC. Total power: 616W.*

By analyzing Fig. 5.25, it can be concluded that just by attaching an extra cold plate on the fourth yoke reduces the temperatures of all the yokes below the Curie temperature with a reasonable safety margin: The hottest temperatures would correspond to Yoke#1 and Yoke#7, with 104°C and 84°C respectively.

Combined cooling of the rings

Although the temperature of all the yokes would be kept below the Curie threshold by installing two cold plates in direct contact with them, the temperature of the rings would still be above the limits. Even if they are not critical for the functionality of the kicker magnets, it is very important to control their temperature as well, because once they exceed the Curie point, their permeability falls rapidly. This parameter is directly related to the electromagnetic properties of the rings, and a drop in its value would mean that the rings do not interact anymore with the beam but they become transparent to the electromagnetic fields [26]. As a consequence, the power would increase in the yokes. It should be noted that the results reported in [26] were not available until 2018. Thus both the CST and ANSYS simulations neglect the fact that the ferrite becomes electromagnetically transparent above its Curie temperature.

For this reason, it can be concluded that the direct cooling of the ferrite yokes must be combined with cooling of the rings. Nevertheless, the mechanical design and assembly of the two independent cooling systems (one for the yokes and another for the rings) would be very complicated given the lack of space in the tank and the brittleness of the materials to be cooled. Other options were considered and are presented below.

5.4 Cooling of ferrite rings

Thermal simulations of cooling of the ferrite rings alone showed that, in addition to significantly reducing the ring temperature, the temperature of the first ferrite yokes were greatly decreased [77]. However, the first yokes would still be above the Curie point unless power could be redistributed from the first yokes to the rings. Hence, in parallel to the thermal studies, electromagnetic studies with CST related to the beam coupling impedance of the magnets were launched to study the possibility of relocate a significant portion of the power deposition from the yokes to the upstream ferrite rings [81].

In Chapter 2, the line of research of the impedance studies was already introduced. As a summary, the beam coupling impedance of the MKIs with the 24 conductor-beam screen presented a strong resonant behavior. According to Eq. 4.3, a way of reducing the power loss is to modify the impedance of the magnet, in particular its coupling to the beam spectrum, by shifting the resonant frequencies of the impedance to higher frequencies where the beam power spectrum is reduced. It must be recalled that these resonant frequencies, given by Eq. 2.3, are a function of the overlap distance between the end of the screen conductors and the external metallic tube [36] (see Fig. 2.7). Advantage can be taken of this: by reducing the overlap length, the resonant frequencies are shifted to higher frequencies as desired.

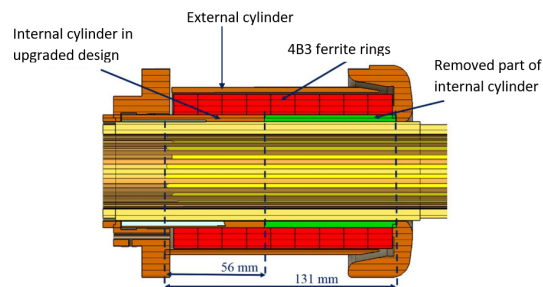


Fig. 5.26 Detail of the upstream ferrite rings with shorter metallic cylinder.

At the beginning of the studies, decreasing the length of the screen conductors was proposed for reducing the overlap distance [35]. However, this approach was replaced by reducing the length of the metallic cylinder, as it is more effective: when part of the metallic cylinder is removed, some of the ferrite rings are exposed to the beam. A parametric analysis for different overlap lengths was performed to obtain the optimum value. Using minimum total power loss as a criterion, 40 mm was the chosen value for initial studies. With such a change, the following benefits are achieved [80]:

1. A reduction in the estimated total power loss of more than 30%, from 616W to 450W thanks to the upshift of the impedance resonant frequencies.

2. A relocation of the power loss from the yokes to the rings, which can be cooled more easily, as they are not at pulsed high voltage. With 40 mm overlap, the predicted power in the first yoke is reduced by a factor of 13, while it is increased by a factor of 15 in the hottest ring, Ring#5.

Both effects are clearly appreciated in Fig. 5.27, where the average power loss per component is plotted for both overlap lengths. The predicted temperatures for each case are shown in Fig. 5.28.

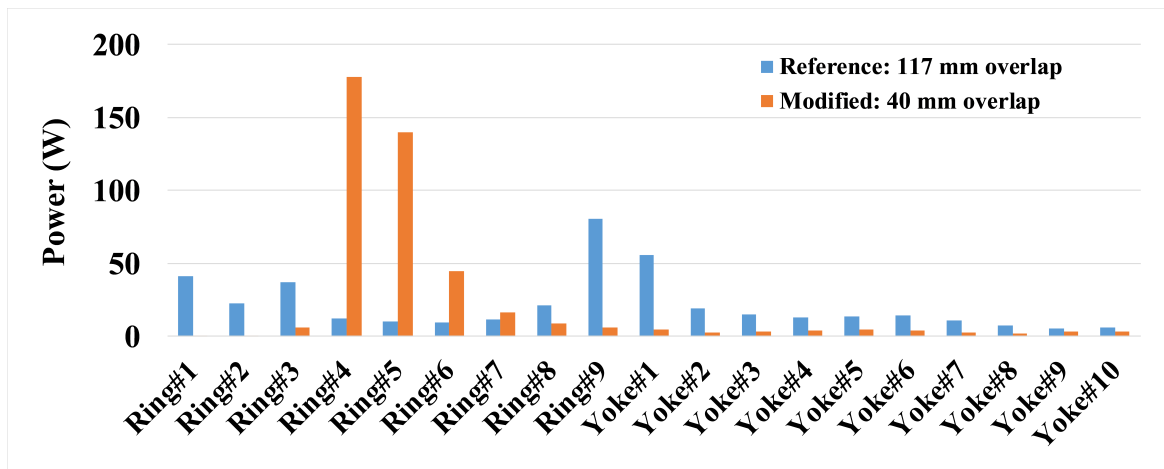


Fig. 5.27 Power distribution for overlap lengths of 40 mm and 117 mm. Model 3 of power deposition.

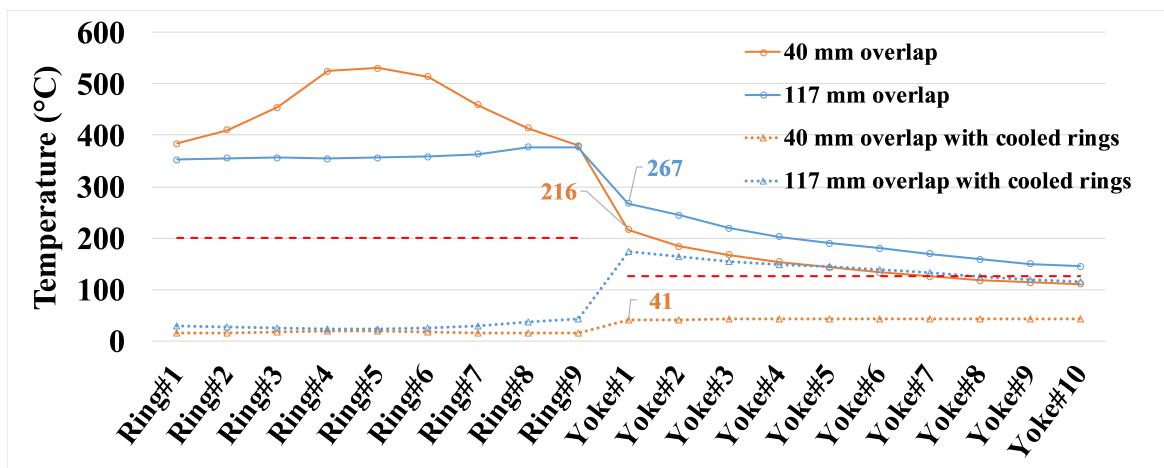


Fig. 5.28 Temperatures for overlap lengths of 40 mm and 117 mm, with (dotted lines) and without (continuous lines) cooling of the rings. Dashed red line: Curie temperature of ferrite types CMD5005/8C11 and 4M2 used in yokes and rings respectively. Model 3 of power deposition for HL-LHC. Total power: 616W (reference) and 450W (modified).

From the analysis of Fig. 5.28, the following conclusions can be drawn:

1. The continuous lines are the results for the models without cooling. By comparing the results, it can be seen the benefit of the modified design upon the temperature of the yokes. In particular, the first yoke temperature is reduced from 267°C to 216°C. However, this is still a high temperature considering that the power generated has been reduced to 4 W. This can be explained by the increased temperature of the rings, higher than 500°C, which causes significant thermal conduction via the alumina tube, and radiation to the yokes.
2. The dotted lines are the results for the models with cooling in the rings. As this was a preliminary study, for simplification purposes the cooling was represented in the thermal model by setting the external surface of the rings at 20°C. For the reference case (117 mm overlap), it can be seen that, even if the rings are cooled, the ferrite yokes are still above the Curie temperature. However, combining the cooling of the rings with the reduced overlap design leads to a drastic reduction of the temperature of all the yokes, the first yoke being at only 41°C.

From the above-mentioned conclusions, it was decided to go for the combined solution of relocating a significant portion of the heat deposition from the yokes to the ferrite rings, plus installing a cooling system around the rings. For the implementation of these changes, the following steps were taken:

1. *Verify the predicted redistribution of power:* One of the MKI magnets was installed with a reduced overlap length in the LHC during the 2017-18 Year End Technical Stop (YETS) to verify that the predictions with reduced overlap and relocated power predictions were correct. The success of the change was assessed by comparing the measured temperatures in this magnet with the temperatures measured in the other MKIs, which were not modified. Further details will be given in the following subsection.
2. *Design the cooling system:* All the steps covered for the design of the cooling system will be thoroughly explained in Chapter 6.
3. *Test the cooling system during Run 3 LHC operation:* To evaluate the efficiency of the cooling system, a full-scale prototype will be installed in an MKI magnet during LS2 to test it with beam during Run3 operation.
4. *Upgrade all the magnets:* If the design is validated during Run3, the production, assembly and commissioning of the cooling system will be performed in all the MKI magnets for HL-LHC operation.

5.4.1 Upgraded magnet

Modifications were implemented in the hottest magnet, MKI8D (see Table 4.2), during YETS17-18, to test its performance with real beam during LHC operation in order to benchmark the simulations. The changes applied were the following [8]:

- *Reduction of the overlap length:* Although the optimum overlap was 40 mm, the metallic cylinder could not be reduced to less than 56 mm due to the presence of mechanical components placed for ensuring a good RF electrical contact between the metallic cylinder and the outside of the alumina tube, which is silver painted where it is in contact with the cylinder (see Fig. 5.26). The total power expected in the magnet was practically the same as with 40 mm overlap, but with 56 mm the first ring fully exposed to the beam was the 5th instead of the 4th. As a consequence, the 5th ring absorbed the maximum power. This influence can be better appreciated in the normalized power distribution (1 W distributed along the whole magnet) shown in Fig. 5.29.

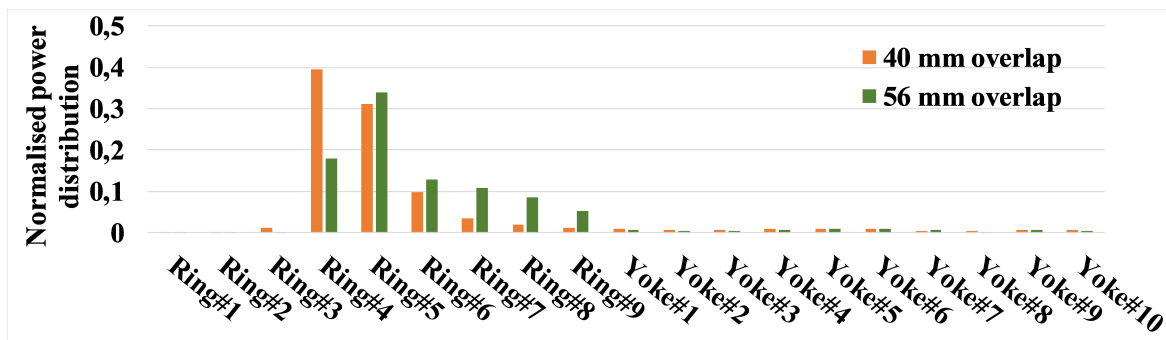


Fig. 5.29 Normalised power distribution for 40 mm and 56 mm overlap lengths.

The power map in the rings is plotted in Fig. 5.30:

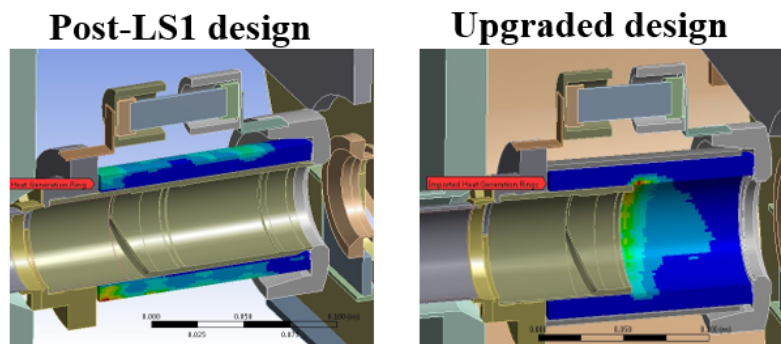


Fig. 5.30 Power distribution map in the upstream rings for the Post-LS1 and upgraded designs.

- *Installation of an external cylinder around the rings:* This was introduced to provide mechanical support to the ferrite rings, which can be seen in Fig. 5.26. As this cylinder was surrounding the rings, it was oxidized in an oven at 800°C in air before its installation in order to improve the heat extraction by thermal radiation.
- *Substitute the type of ferrite for the rings with one of higher Curie point:* In the post-LS1 design, two different type of ferrites are used alternately within the nine rings: Ferroxcube 4B3 and 4M2 types with Curie temperatures of 250°C and 200°C, respectively. However, given the higher power deposition expected in the rings with the implemented changes in the overlap, it was decided to use only type 4B3 in all the rings, which gives more margin before reaching the Curie point.
- *Installation of two additional sensors:* To provide more information about the thermal behaviour of the magnets, two more PT100 temperature sensors were included in the locations indicated in Fig. 4.29. The other sensors already present were not removed as they are useful for comparing the readings with the ones obtained in the other magnets at the same location.
- *Application of a surface coating inside of the alumina tube:* A film of Cr_2O_3 was applied by magnetron sputtering in the internal surface of the alumina tube for reducing the SEY [8].

Before the installation of this magnet in the LHC, a thermal simulation including in the model the implemented changes above mentioned was performed for the maximum power expected during 2018 LHC operation. The objective was to verify that the temperature of all the components was below the Curie point, as there was major concern about the rings due to their increased power. Results are presented in Fig. 5.31.

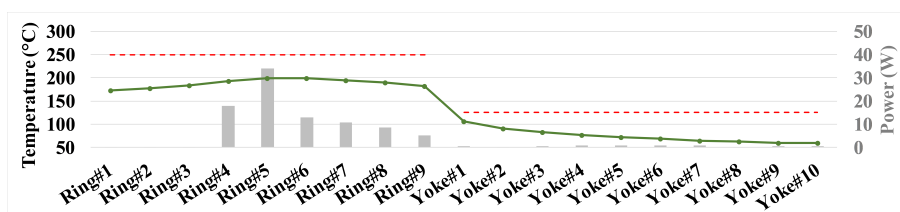


Fig. 5.31 Predicted temperatures for maximum power expected in the upgraded magnet. Dashed red line: Curie temperature of ferrite types CMD5005/8C11 and 4M2 used in yokes and rings respectively. *Model 4 of power deposition. Total power: 100 W*

Thanks to the extra safety margin of 50°C provided by the use of 4B3 type of ferrite in all the rings, no issues were expected for Run2 operation. This led to the approval of the installation of this upgraded magnet in the LHC.

To validate its performance, the measured temperatures at the upstream end of the side plates during LHC operation were compared to the ones obtained in the other magnets. As can be seen in Fig. 5.32, the upgraded MKI shows the lowest temperatures so the reduction of the power in the yokes is evident, especially considering that this one was historically the hottest.

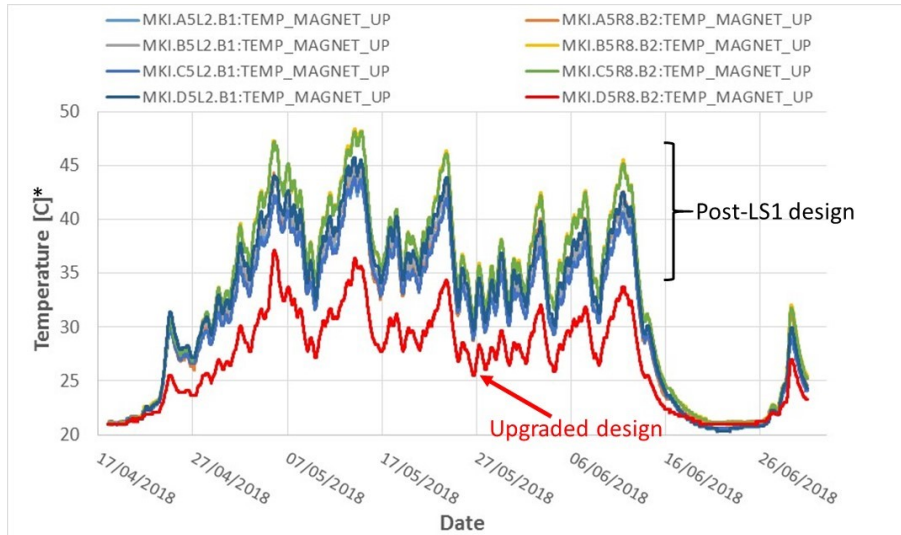


Fig. 5.32 Comparison of the measured temperatures in all the magnets at the sensor located in the upstream end of the side plates during mid-2018.

It can be concluded that this successful implementation makes possible to decrease the power deposition in the yokes, and thus validates the proposal to combine this with active cooling of the ferrite rings.

Chapter 6

Design of the water cooling system

In this chapter, the steps followed for the conception and design of the cooling system will be presented. Particular challenges were faced due to the difficulties imposed by installing a liquid cooling system in an ultra high vacuum environment, summed to the fact that the ferrites are extremely difficult materials for heat extraction due to the intrinsic poor mechanical properties and limited thermal conduction. For those reasons, a particular methodology was followed and each of the steps will be thoroughly described.

6.1 Methodology

The methodology followed for the design of the cooling system is represented schematically in Fig. 6.1 and details of each step are further explained below:

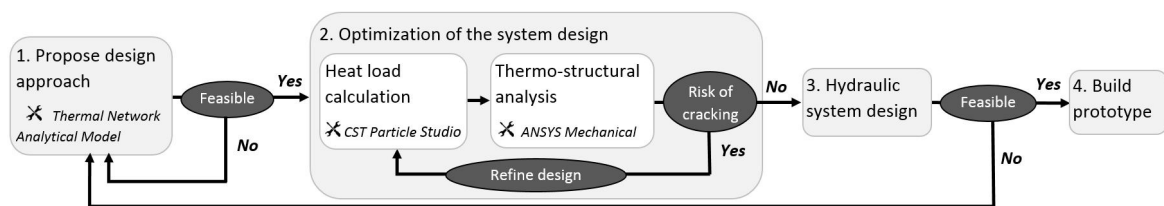


Fig. 6.1 Scheme of the methodology of the process.

1. Propose design approach:

A simplified thermal network model is used to identify analytically the parameters that are key to achieving a good heat extraction from the ferrite rings. On the basis of the conclusions, design guidelines are provided for choosing the configuration and dimensions of the cooling system. The selected approach is presented, together

with a preliminary mechanical feasibility study to confirm its feasibility before the optimization.

2. Optimization of the system design:

Design and dimensions are optimized by iterating the heat load calculations and the thermo-structural analysis for each case under study, aiming not only at reducing the total heat deposited but also avoiding areas of high power density, to prevent cracking of the ferrite rings.

Import heat loss from CST to ANSYS:

As commented in Chapter 4, this step was key for the design of the cooling system to properly assess the thermal stresses generated in the ferrite ring due to temperature gradients between the cooled surface and the hot spots caused by concentrated heat load. Hence, the thermal model was improved so that the power distribution obtained with CST[®] was imported accurately to ANSYS[®]. This corresponds to Model 4 described in Chapter 4. As a reminder, it was concluded from its validation that the scaling factor, historically applied to the obtained power to match the lab measurements, was not needed for the upgraded design, and the predicted temperatures using as input the power without scaling were in good agreement with temperature readings during LHC operation (see Fig. 4.4). Nevertheless, it was decided to keep applying a factor of 2.5 to the power to give a safety margin.

Simplify the thermal model:

Instead of modelling the whole system, only the main components relevant to the cooling system were included for reducing the computation times. In particular, the yokes were not included as their influence upon the tube temperature is negligible due to the low power deposition in the yokes. Moreover, radiation is not considered as heat is assumed to be transferred from the ferrite tube to the water cooling circuit only by conduction. This simplified approach has been validated by comparing the maximum temperature in the tube obtained with both models (simplified and complete), and they only differ by 2% with respect to room temperature [78].

Coupled thermo-structural analysis:

The thermal results are coupled to a structural analysis in order to evaluate a potential risk of cracking of the ferrite tube. Two different failure criteria are used: Christensen and Mohr-Coulomb criteria.

- The Christensen criterion is applicable for a wide range of isotropic materials, both ductile and brittle [27]. The following condition must be fulfilled [27]:

$$\left(\frac{1}{\sigma_t} - \frac{1}{\sigma_c}\right)(\sigma_1 + \sigma_2 + \sigma_3) + \frac{[(\sigma_1 - \sigma_2)^2 + (\sigma_2 - \sigma_3)^2 + (\sigma_3 - \sigma_1)^2]}{2\sigma_t\sigma_c} \leq 1, \quad (6.1)$$

where σ_t and σ_c are the ultimate tensile and compressive strength, respectively, and σ_1 , σ_2 and σ_3 are the values of the principal stresses. It must also be verified that none of the principal stresses exceed the tensile strength. This criterion is introduced manually in the ANSYS® code and Eq. 6.1 is solved using the stress-strain data during the post-processing. It must be verified whether the obtained stresses are within the range -1 and 1 to avoid cracking.

- The Mohr-Coulomb criterion is widely applied for brittle materials. It states that failure occurs when the combination of the Maximum, Middle, and Minimum Principal stresses equal or exceed their respective stress limits [65]. In ANSYS® Mechanical™, a Mohr-Coulomb Stress Safety Tool is already implemented [2].

3. Hydraulic system calculations:

The dimensions of the cooling pipe and flow conditions are obtained analytically. It must be verified that the thickness of the cooling pipe is above the minimum required to withstand a certain pressure, which is calculated following the guidelines presented in [42]. This technical specification is based on the European Norm EN13480-5 for metallic industrial piping: "Inspection and Testing". A coupled thermo-structural analysis is also done to verify that the stresses generated in the pipe, due to thermal expansion combined with the fluid pressure, do not cause plastic deformation according to Von Mises failure criterion, widely used for ductile materials [65].

4. Build the prototype:

A prototype of the cooling circuit will be built for studying its feasibility and efficiency before its implementation in a kicker magnet during Long Shutdown 2 (LS2), from 2019 to 2021, so that it can be tested with beam during Run3 (from 2021 to 2024) before upgrading all magnets for the HL-LHC before and during LS3 (from 2024 to 2026) [3].

6.2 Results of studies

In this section the results of the studies from the conception of the cooling system to the building of the prototype are reported, following the methodology described above.

6.2.1 Proposal of design approach

Preliminary decisions on the configuration of the cooling system are:

- A single ferrite tube will be used instead of the nine rings to improve the longitudinal heat transfer and facilitate the mechanical assembly of the cooling system.
- The heat sink will consist of a cold plate with attached water pipes.

The thermal network model created for identifying the most critical parameters for the heat extraction from the ferrite tube to the cooling circuit is presented in Fig. 6.2. Steady-state conditions are assumed and, as a worst case, all the heat deposited on the surface of the tube opposite to the cooling circuit, i.e. the internal surface. Radiation is not considered. The conclusions are summarized in Table 6.1.

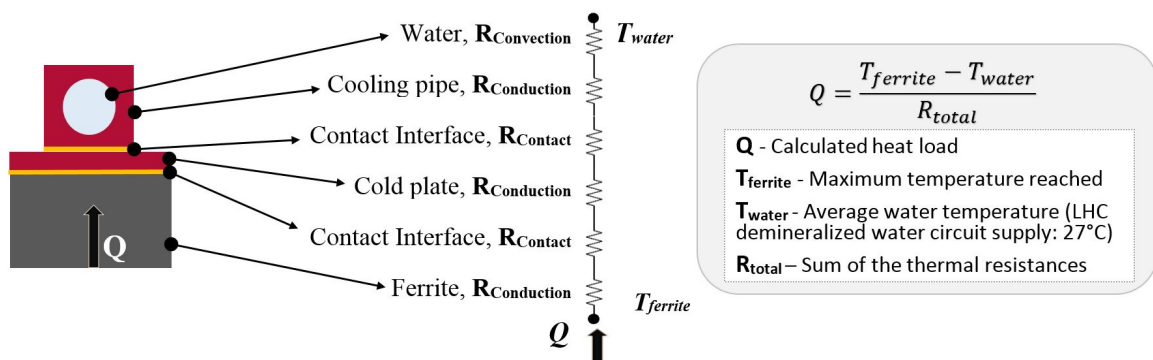


Fig. 6.2 Thermal network model for heat transfer.

Resistance	Components affected	Guidelines for reducing the resistance	Expected contribution to total resistance
$R_{Convection}$	Cooling pipe	Optimize pipe dimensions to achieve a high convection coefficient.	Low: High flexibility to choose dimensions.
$R_{Conduction}$	Cooling pipe	* Use materials with high thermal conductivity (and vacuum compatibility).	Low: Copper OFE is used for its high thermal conductivity.
	Cold plate	* Minimize the dimension parallel to the direction of the heat flow.	Low: A very thin plate of copper OFE will be used.
	Ferrite	* Maximize the area of the surface perpendicular to the direction of the heat flow.	High: The heat conduction through the ferrite is limited due to its low thermal conductivity ($4.2 W/(m \cdot K)$) and the dimensions of the tube are also limited by the manufacturing process and the available space, imposing a maximum length and a minimum thickness.
$R_{Contact}$	Interface cooling pipe/cold plate	* Maximize the area of the surfaces in contact. * Obtain a high thermal contact conductance (TCC) in the joint ($W/(m^2 \cdot K)$).	Low: Using same material for both components allows a highly effective brazing that ensures a sound joint.
	Interface cold plate/ferrite		Very high: Due to the low thermal conductivity and poor mechanical properties of the ferrite, and the different coefficients of thermal expansion of copper and ferrite, achieving a good thermal contact is very challenging.

Table 6.1 Design guidelines deduced from thermal network model.

The resistances mentioned in Table 6.1 are defined as follows:

- $R_{conduction}$: Solving Fourier's law of heat conduction for cylindrical systems [17], the thermal conduction resistance is defined by:

$$R_{conduction} = \frac{Ln \frac{R_{external}}{R_{internal}}}{2\pi Lk} \quad (6.2)$$

Where $R_{external}$ and $R_{internal}$ are the external and internal radius of the cylinder, k is the thermal conductivity of the material ($W/m \cdot K$) and L is the longitudinal length of the cylinder.

- $R_{convection}$: It is defined by:

$$R_{convection} = \frac{1}{Ah} \quad (6.3)$$

Where A is the area of the internal surface of the cooling pipes (m^2) and h is the convection coefficient ($W/m^2 \cdot K$). This value is given by iteration with the hydraulic calculations.

- $R_{Contact}$: It is defined by:

$$R_{Contact} = \frac{1}{A TCC} \quad (6.4)$$

Where A is the area of the surfaces in contact and TCC is the thermal contact conductance across the joints ($W/m^2 \cdot K$).

On the basis of the conclusions of the thermal network model, the main challenge was to achieve an acceptable thermal contact between the ferrite tube and the cold plate. To that end, two major approaches were studied.

Pressure contact

The first one was based on pressing a cold plate against the flat surface of the ferrite cylinder as shown in Fig. 6.3. A ferrite tube of 10 mm length and internal and external radius of 40 and 70 mm, respectively, was proposed for preliminary feasibility studies before optimizing the dimensions. The small thickness was chosen for reducing the dimension parallel to the direction of the heat flow, and the large external radius, for increasing the surface in the perpendicular direction, as advised in the design guidelines.

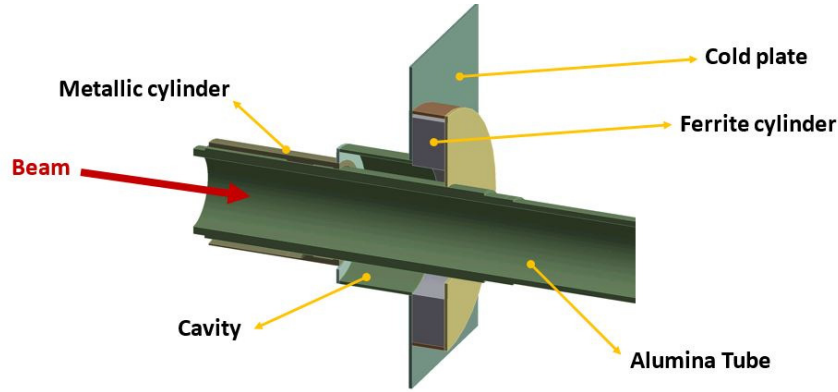


Fig. 6.3 Cold plate pressed to the flat surface of the ferrite tube.

The minimum pressure needed to create a sufficiently good thermal contact between the ferrite tube and the cold plate is related to the value of the Thermal Contact Conductance (TCC) required. The necessary TCC was first calculated using an ANSYS thermo-structural analysis, iterating for different values of the TCC to determine for which cracking occurs due to thermal stress. This is evaluated according to the Christensen failure criterion. For a heat load of 350 W in the ferrite cylinder, predictions show that a minimum TCC of 600 W/(m²·K) is required. Two models widely used in vacuum environments have been considered to obtain the corresponding pressure [51]. The first model assumes plastic deformation on the contacting asperities, and the TCC is evaluated according to [83]:

$$TCC = \frac{1.25 \cdot m \cdot k_s}{\sigma} \left(\frac{p}{H_c} \right)^{0.95}, \quad (6.5)$$

Where σ is the RMS of the roughness of surfaces in contact,

$$\sigma = \sqrt{\sigma_1^2 + \sigma_2^2} \quad (6.6)$$

m is the RMS of surface slopes of both components,

$$m = \sqrt{m_1^2 + m_2^2} \quad (6.7)$$

being m_1 and m_2 ,

$$m_1 = 0.125(1.11\sigma_1)^{0.402} \quad (6.8)$$

$$m_2 = 0.125(1.11\sigma_2)^{0.402} \quad (6.9)$$

k_s is the effective thermal conductivity of the materials in contact,

$$k_s = \frac{2k_1k_2}{k_1 + k_2} \quad (6.10)$$

finally p is the applied pressure and H_c is the micro-hardness of the softer material.

The second model assumes elastic deformation, for which the TCC is estimated as [54]:

$$TCC = \frac{1.55 \cdot m \cdot k_s}{\sigma} \left(\frac{\sqrt{2}p}{E \cdot m} \right)^{0.94}, \quad (6.11)$$

where:

$$E = \frac{E_1 \cdot E_2}{E_2(1 - (\nu_1)^2) + E_1(1 - (\nu_2)^2)}, \quad (6.12)$$

with E being the Young modulus and ν the Poisson ratio of the materials in contact.

The level of validity of each model depends upon whether the contacting asperities present elastic or plastic deformation, which is very difficult to determine a priori [51]. In this case, the elastic deformation model is used because, for the plastic model, the micro hardness is not readily found in literature. To calculate it analytically, an iterative model using the Vickers hardness is proposed by [84], but still empirical data is missing for the calculation.

Solving Eq. 6.11 for a TCC of 600 W/(m²·K), the pressure needed is approximately 3 MPa, which corresponds to 3.2 tonnes of force to be applied. Considering the poor mechanical properties of the ferrite, this approach can lead to cracks, so it was discarded and another method for creating a good thermal contact was investigated.

High contact conductance bonding

Soldering, bonding by hot isostatic pressing, and vacuum brazing were studied in the past at KEK [68]. Some successful test results were achieved for joining ferrite and copper on a flat surface with a cross section of 20×20 mm² with vacuum brazing. However, due to the considerable mismatch of coefficients of thermal expansion between copper and ferrite, brazing of flat surfaces is very limited with respect to dimensions as larger surfaces create higher thermal stresses, resulting in cracking of the brazed interface. A circumferential joint, with copper outside and the ferrite tube inside, results in mainly compressive stress in the joint and the ferrite cylinder, which is much more favourable for brittle materials such as ferrite. For this reason, this new design approach was selected for study.

With this method, a high value of the TCC can be achieved, in the order of magnitude of 10,000-100,000 W/(m²·K) (values between 54,000 and 143,000 W/(m²·K) have been measured after brazing ceramics to metal (SiC to a molybdenum alloy) at CERN [50]). However, in the following studies a TCC of 5,000 W/(m²·K) is used as a worst case assumption to take into consideration the possibility of not achieving a good brazing interface over the whole contact area, as some defects might occur.

6.2.2 Optimization of the system dimensions

The cold plate consists of a copper tube, up to 2 mm thick, placed around the external surface of the ferrite cylinder. A long length and small thickness ferrite cylinder is desirable according to the guidelines for improving the heat extraction shown in Table 6.1. Regarding the ferrite cylinder, an internal and external radii of 38 mm and 48 mm respectively are proposed based on available space and CST simulations. Although a thinner ferrite cylinder would reduce its thermal resistance, it would also increase the chances of cracking due to its brittleness. The length of the ferrite cylinder and the dimensions and the configuration of the components in the surroundings need further optimization:

Radial thickness:

The radial thickness of the ferrite cylinder plays a key role in the effectiveness of the heat extraction. From a thermal point of view, it was desirable to minimize the thickness, because the heat is generated in its inner side, where it first interacts with the coupled RF field, and then it is transferred to the water cooling system on its outer surface via thermal conduction through the thickness of the ferrite cylinder. Due to the low thermal conductivity of ferrites, it was highly desirable to minimize the thickness so that the thermal resistance is reduced. A parametric study was done in CST for different thicknesses. The real longitudinal beam impedance obtained for each value is shown in Fig. 6.4 [79]:

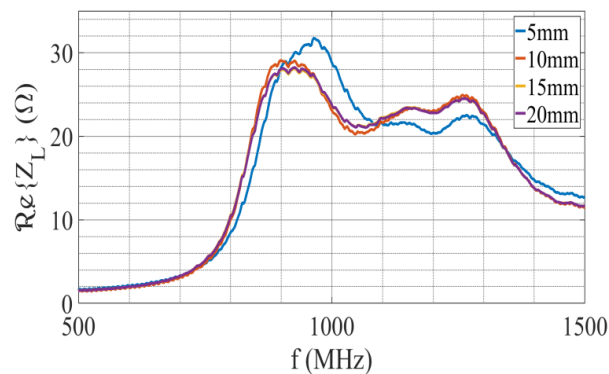


Fig. 6.4 Effect of the radial thickness of the ferrite on the real longitudinal beam impedance of the magnet [?]

Although a thickness of 5 mm would move the peak of the real longitudinal beam impedance of the MKI to higher frequencies, where the coupling to the beam spectrum is weaker, it was discarded as it would offer limited mechanical strength. For thicknesses above 10 mm there was no significant improvement, so it was decided to choose 10 mm.

At the same time, the value of the internal radius was carefully selected, in order to avoid thermal energy being transferred to the alumina tube and avoiding close proximity to surfaces that could damage the ferrite.

All in all, the selected dimensions were 38 mm for the internal radius and 10 mm for the radial thickness, which were considered a good compromise for low total dissipated power, sufficient heat extraction efficiency, good mechanical stability as well as manufacturing feasibility [79].

Longitudinal length:

For optimizing the length of the ferrite cylinder, beam impedance simulations were performed by the team expert for different lengths. A tendency to decrease the total power induced in the ferrite cylinder with longer tubes was observed (see Fig. 6.5).

A corresponding coupled thermo-structural analysis was done for different values of the tube length. In particular, for 60 mm length, no failure was predicted according to the Christensen criterion, as the obtained stresses were within the limits of -1 and 1 (-0.5 and 0.98) for the calculations with the 2.5 safety factor included in the power. For smaller lengths failure was predicted (a tube of 45 mm length presents stresses of -1.6 and 2.3), whereas no additional benefits are obtained with a tube longer than 60 mm. In addition, larger values for the length would add complexity to the manufacturing process (sintering), and the available space in the vacuum tank is quite limited. For those reasons, a tube length of 60 mm was selected [29].

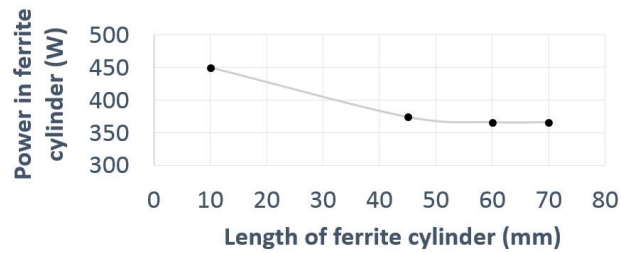


Fig. 6.5 Total power in ferrite cylinder as a function of the longitudinal length.

Configuration of the beam screen:

A second set of iterations for optimizing the design configuration was carried out for the aforementioned selected dimensions of 60 mm length, internal radius of 38 mm and external radius of 48 mm. The goal was to achieve a reasonably uniform heat distribution for a more efficient extraction to the cold plate, reducing the risk of cracking of the ferrite due to temperature differences. For this, different configurations of the surrounding components, which play a role in the longitudinal beam impedance, were studied to further reduce the power deposition in the tube and to avoid areas with high density power [79]. As a reference, those components are highlighted in Fig. 6.6. Note that the configuration of the vacuum gap and the end of the screen conductors is the same as the one used in the post-LS1 design [35]:

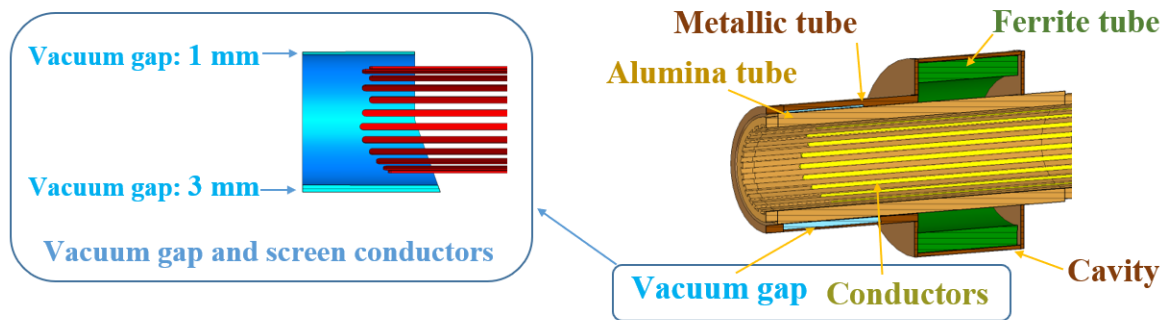


Fig. 6.6 Original configuration of the vacuum gap and the upstream end of the screen conductors [35].

Initially, modifications in the transition from the metallic tube to the housing of the ferrite cylinder were investigated, shown in Fig. 6.7:

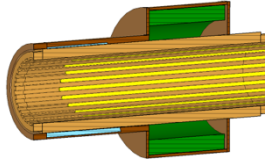
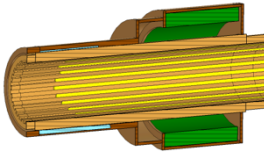
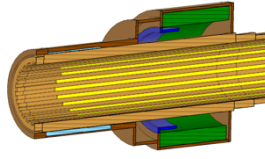
	Reference	Additional cavity	Additional cavity with insert
			
Total power	348 W	366 W	364 W
Max. temperature	106 °C	88.4 °C	80.6 °C

Fig. 6.7 Studied modifications of the transition between the metallic tube and the cooper tube to optimize the heat distribution [29].

Impedance simulation studies indicated that an additional cavity (shown in second and third designs in Fig. 6.7), reduced the quality factor (Q) of the first high frequency mode of the structure, as shown in Fig. 6.12, red and yellow curves respectively. This was considered beneficial to avoid strong resonances, as losses may increase considerably in case they hit a beam harmonic. Its effect upon the maximum temperature of the ferrite cylinder is shown in Fig. 6.7. The lowest temperature is obtained with the extended additional cavity. Details of this configuration are shown in Fig. 6.8.

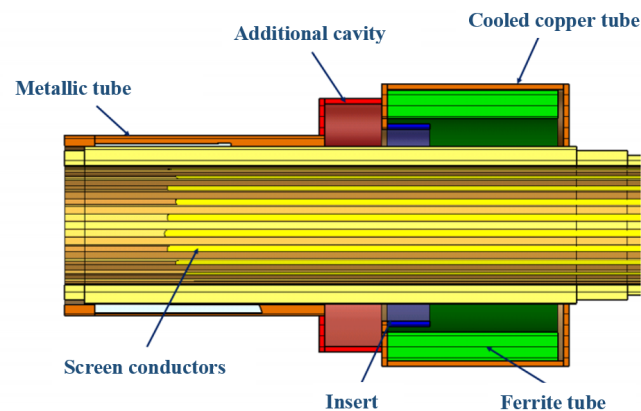


Fig. 6.8 Modified MKI beam screen configuration.

A 15 mm metallic cylindrical insert inside the ferrite cylinder, highlighted in blue in Fig. 6.8, was introduced to further reduce the high concentrations of dissipated power at one end of the ferrite cylinder. Thanks to this, a smoother distribution of the dissipated power along the length was achieved as shown in Fig. 6.9.

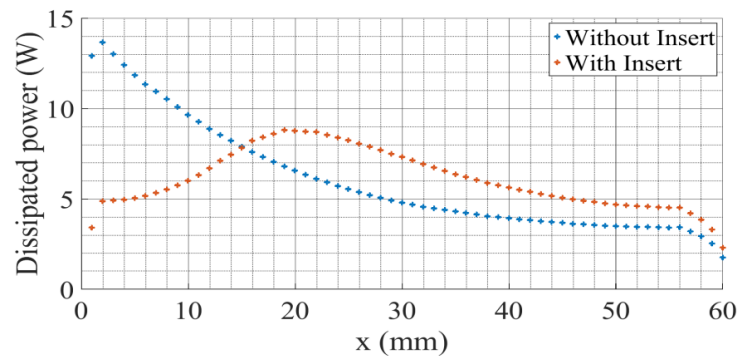


Fig. 6.9 Expected power distribution along the longitudinal length of the ferrite cylinder with and without the insert.

It is important to highlight that, although the model without the additional cavity (shown in first design in Fig. 6.7) gives the lowest total power deposition, the maximum temperature reached in the ferrite cylinder is notably higher than in the other cases due to a more concentrated power distribution. This emphasizes the importance of not just focusing on reducing the total power, but on achieving an adequately smooth and not strongly concentrated distribution of the power deposition.

For the selected beam screen configuration, the effects of modifying the geometry and dimensions of the vacuum gap between the metallic cylinder and the alumina tube, and the length and disposal of the screen conductors were also studied [79]. The goal of this study was to investigate the possibility of achieving a less localized power deposition in the ferrite cylinder in the azimuthal direction. The first image in Fig. 6.10 shows the Post-LS1 configuration, that in principle was kept as baseline design. For HV reasons the screen conductors are reduced in length towards the HV busbar at the bottom, and adjacent conductors are staggered in length. The overlap length between the screen conductors and the vacuum gap is approximately 20 mm. The vacuum gap is 3 mm adjacent to the HV busbar and 1 mm at the top.

The modifications proposed are shown in Fig. 6.10:

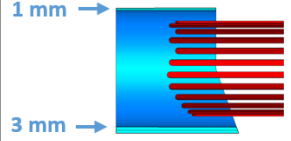
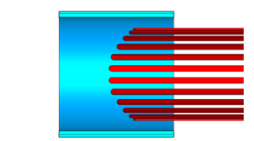
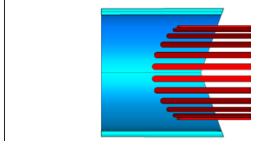
	Reference (Post-LS1 configuration)	3 mm symmetric vacuum gap and conductors	V-shape, 3mm symmetric vacuum gap and conductors
			
Total power	364 W	400 W	356 W
Max. temperature	80.6°C	87.3°C	82.3°C

Fig. 6.10 Studied modifications of the vacuum gap and screen conductors to optimize the heat distribution.

The first proposed design consisted of extending the length of the vacuum gap to 59 mm and having 3 mm constant thickness, as shown in the second image of Fig. 6.10. The other design considered was based on the previous, with the difference of ending with a V-shape as shown in the third image of Fig. 6.10. In both cases, the upper part of the screen conductors was a mirror image of the lower part. The real longitudinal beam impedance of each case is shown in Fig. 6.12, and the azimuthal distribution of the power in Fig. 6.11.

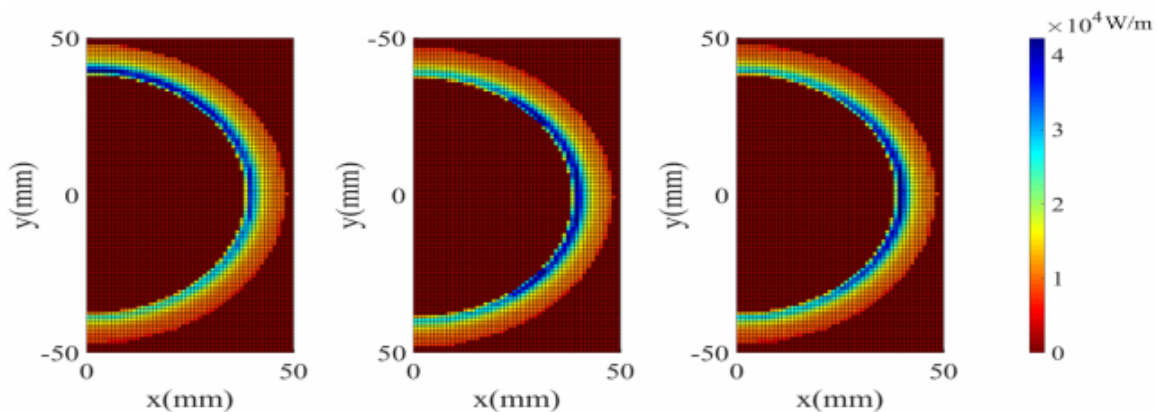


Fig. 6.11 Azimuthal distribution of power in the ferrite cylinder with different beam screen configurations [79].

Due to HV considerations, limited options were realistically available. Besides, thermal simulations indicated that the temperature reached with the modified designs would be higher than the one reached with the Post-LS1 configuration (see Fig. 6.10). Hence these modifications were not pursued any further.

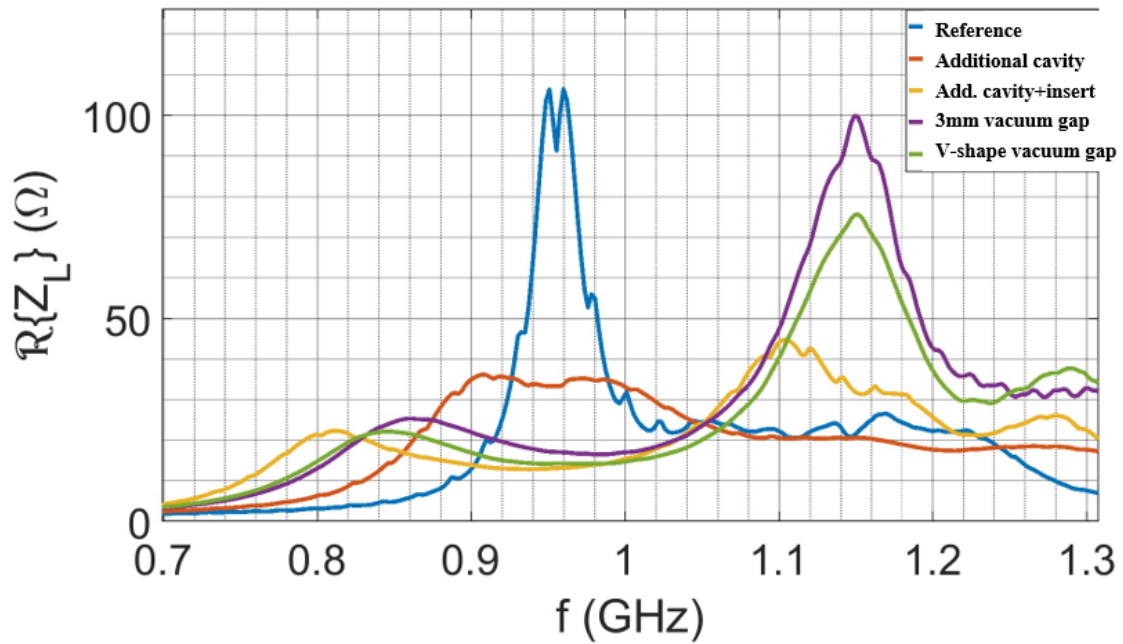


Fig. 6.12 Real part of longitudinal beam coupling impedance for different configurations of the beam screen design [79].

Minimum required thermal contact conductance (TCC) between ferrite and copper tube:

As it has been mentioned, a high conductance bonding between the ferrite cylinder and the surrounding copper tube is critical for ensuring a good heat extraction. Coupled thermo-structural analyses were carried out to estimate the minimum value of the TCC for which the ferrite showed risk of cracking. A parametric study was done for different values of the TCC, and its effect upon the maximum temperature predicted in the ferrite cylinder is shown in Fig. 6.13.

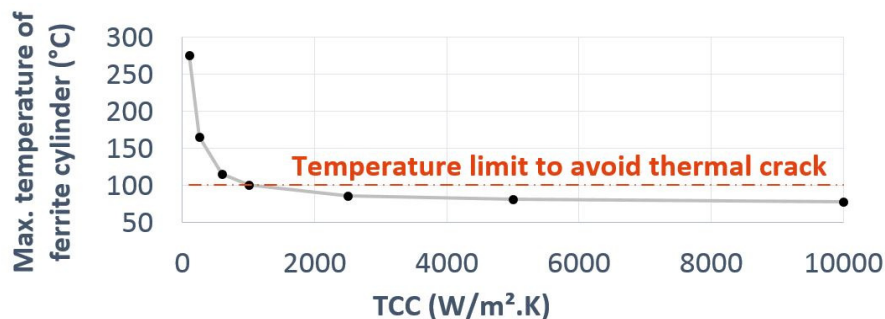


Fig. 6.13 Maximum temperature in ferrite cylinder versus thermal contact conductance at the joint between the ferrite and copper tube. *Safety factor of 2.5 included in the power.*

The temperatures reached in the ferrite cylinder are highly dependant on the TCC for low values. However, for higher TCC, the maximum temperatures predicted in the tube are close to constant. The thermo-structural analyses showed that the stresses generated in the ferrite would exceed the limits, according to the Christensen criterion, for a TCC of $1,000 \text{ W}/(\text{m}^2 \cdot \text{K})$. This corresponds to a maximum temperature just under 100°C (see red dot in Fig. 6.13), which was set as a design threshold. For the next studied value of TCC, which is $2,500 \text{ W}/(\text{m}^2 \cdot \text{K})$, the maximum predicted temperature was 85.6°C , and obtained stresses were -0.95 and 0.69 .

The selected bonding method was brazing as it should ensure a TCC higher than $10,000 \text{ W}/(\text{m}^2 \cdot \text{K})$. According to Fig. 6.13, for this value the maximum temperature of the ferrite cylinder would be approximately 80°C . Note that the previous results given in Fig 6.7 and Fig 6.10 were done for a value of $5,000 \text{ W}/(\text{m}^2 \cdot \text{K})$ to give a safety margin.

A simulation of the cooling system with the modified beam screen configuration that included the first 10 yokes was performed in order to ensure that the analysis done with simplified model was giving similar results. Besides, it was of interest to have an estimation of the temperatures that will be expected in the yokes for HL-LHC operation. Two simulations were performed, with and without the cooling system, to evaluate its impact on the temperature of the yokes. For the modelling of the cooling system, a temperature of 30°C was set on the external surface of the copper tube. Note that, in both cases, the power distribution was imported from CST after applying the safety factor of 2.5. The TCC in the contact between the ferrite and the copper tube was set to $5,000 \text{ W}/(\text{m}^2 \cdot \text{K})$. Results can be found in Fig. 6.14.

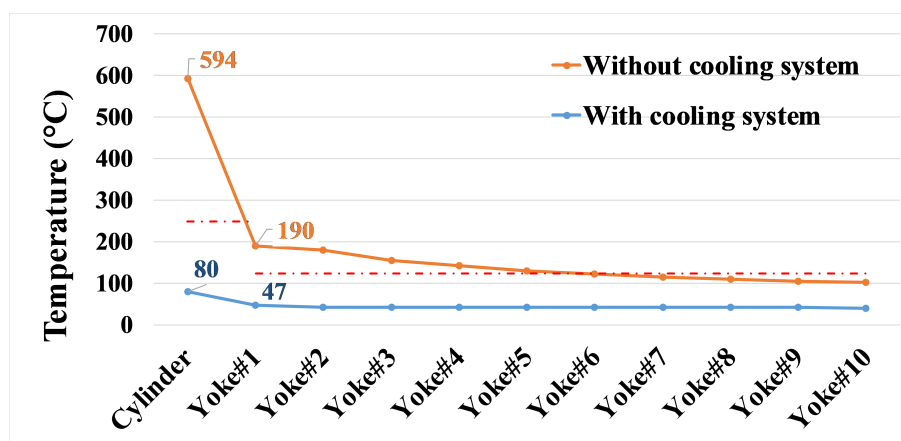


Fig. 6.14 Temperatures obtained with and without cooling system. *Model 4 of power deposition for HL-LHC.*

It can be concluded that the installation of a cooling system is key to keeping the temperatures of all the components below the Curie point. These simulations also confirm that the simplified model is valid for studying the ferrite cylinder temperature. In fact, it predicts a maximum temperature of the cooled ferrite cylinder of 80.6°C (see Fig. 6.7), very similar to the one obtained with the full model (80°C).

6.2.3 Hydraulic system design

A demineralised water network goes around the 27 km long LHC tunnel to cool different equipments. The demineralised water is produced on the surface and is then distributed to the underground caverns for the filling of secondary cooling circuits. Each demineralised water circuit is closed and equipped with a set of pumps and heat exchangers, an expansion vessel, a filter, an ion cartridge and all the necessary control and regulating devices. The heat exchangers are connected to the primary water circuits that dissipate the heat to the atmosphere by cooling towers on the surface [57].

The MKI ferrite cylinder will be cooled with the demineralized water supplied by one of the secondary circuits. The calculation of the hydraulic parameters of the cooling system must aim for an efficient heat extraction, but also take into account the limitations imposed by the LHC demineralized water network. The following requirements must be fulfilled:

- Reynolds number must be higher than 2,000 to ensure a turbulent flow, which extracts the heat much more efficiently than laminar flow.
- The nominal velocity of the fluid is set to 1.5 m/s to avoid erosion of the pipes. This value is based on studies performed at CERN, which indicate that the velocity in copper pipes should be within the range of 0.5 m/s and 3 m/s [43].
- The temperature increase of the circulating water from inlet to outlet at the vacuum tank must be reasonably low, aiming at less than 5°C , to ensure an efficient heat transfer through all the ferrite cylinder.
- The pressure loss in the cooling system must be lower than the differential pressure available from the LHC demineralized water network, which is approximately 12 bar (16 bar at the inlet line and 4 bar at the outlet line [20]).
- The four magnets at each point must be cooled in parallel, to ensure that the input water temperature is similar for all of the magnets.

The hydraulic calculations are done analytically by iterating the value of internal diameter of the pipes until the above mentioned conditions are met. The final values are shown in Table 6.2.

	Value	Requirements
Internal diameter of cooling pipe (mm)	4.5	-
Reynolds number	9,640	>2,000
Convection coefficient (W/m ² ·K)	9,110	-
Flow (l/min)	1.43	-
Water velocity (m/s)	1.5	≥0.5, ≤3
ΔT _{water} (°C)	3.6	<5
Δp (bar)	0.22	< 12
Max. stress in the pipes (MPa)	20	<33 (yield strength)
Minimum wall thickness (mm)	0.96	<1 (actual thickness)
Number of turns around the copper tube	4	-

Table 6.2 Hydraulic system parameters.

It is worth mentioning that the pressure loss of the cooling system has been calculated using the Darcy-Weisbach correlation. For simplicity, and because there is enough margin until reaching the 12 bars limit imposed by the LHC cooling circuit, the additional losses due to bends, flexible pipes, valves, etc, have not been included in the total pressure loss.

The calculation of some of the parameters mentioned in Table 6.2 will be further detailed below:

Maximum stress in the pipes (MPa)

To obtain the maximum stress that will be generated in the pipes due to the material thermal expansion and the fluid pressure, an ANSYS thermo-structural analysis has been carried out.

For this study, some modifications have been introduced to the simplified model: In this case, the cooling pipes have been included. Besides, instead of assuming a fixed temperature of 30°C in the copper tube, the convection coefficient calculated analytically (see Table 6.2) has been introduced as a boundary condition on the internal surface of the pipe. The thermal analysis results are shown in Fig. 6.15. The maximum temperature of the ferrite cylinder is 88°C. Note that with the simplified version it was 80°. This predicted higher temperature in the ferrite cylinder is caused by the temperature distribution in the copper tube, which has now some areas, where there is no direct contact to the cooling pipes, reaching up to 40°C.

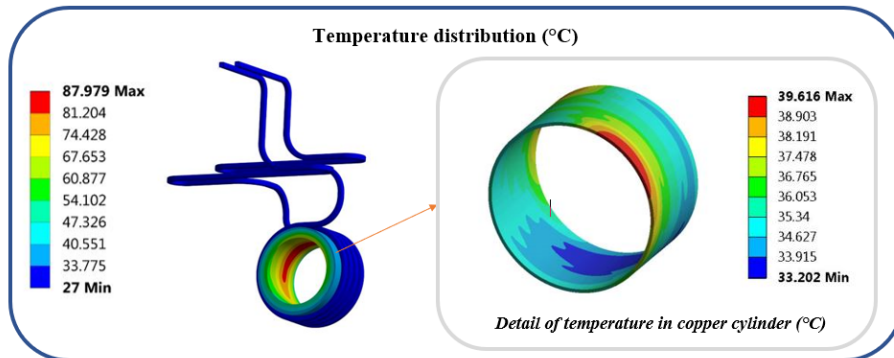


Fig. 6.15 Left: Temperature distribution in the cooling system obtained with the model including the cooling pipes. Right: Detail of the temperature distribution in the copper tube.

The temperature distribution obtained with the thermal analysis has been coupled to a structural analysis in order to account for the thermal stresses. A pressure of 16 bar (available from the LHC demineralized water network at the inlet line) has been defined in the internal surface of the pipes. The stresses obtained are shown in Fig. 6.16. The pipes have been evaluated according to Von Mises failure criterion, which is more convenient for ductile materials as it is the case of the annealed copper. The stresses in the ferrite cylinder have been evaluated according to the Christensen criterion.

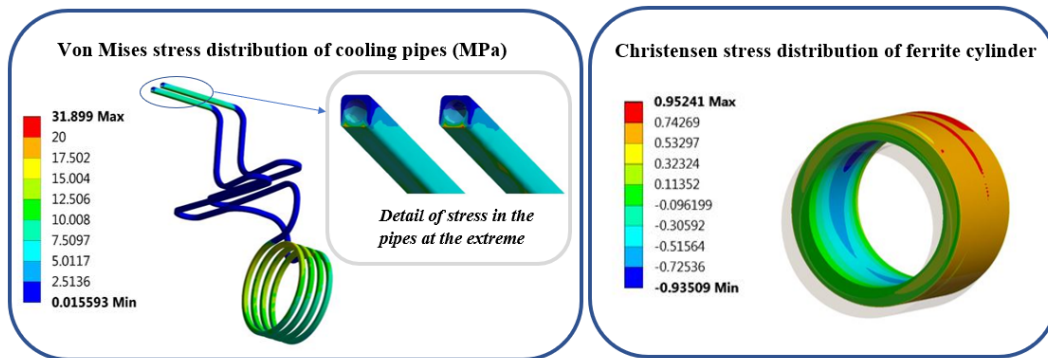


Fig. 6.16 ANSYS Structural analysis results. Left: Von Mises stress distribution in cooling pipes, with detailed view at the end. Right: Christensen stress distribution in ferrite tube.

As shown in Fig 6.16, the maximum stress reached in the cooling pipes is approximately 32 MPa, which is very close to 33 MPa (the yield strength of annealed copper as indicated in Table 6.2). However, this high stress is only found in a localized area at the entrance of the cooling pipes, as shown in the detail of Fig 6.16. Note that here, the model has been constrained by defining the cross-section as a fixed support. Besides, a high density mesh is used in that zone, which can lead to not realistic values of high stress due to the small volume

of the elements. For these reason, and considering the limited area with this high stress peak, it can be neglected. Indeed, apart from this concentrated area of high stress, the rest of the cooling pipes do not exceed 20 MPa. This can be noticed in Fig. 6.16, where the scaling of the legend has been modified to show in red all the areas with values of the stress above 20 MPa, which only appear at the entrance of the pipes. This value is well below the yield strength limit, so it can be concluded that no issues are expected in the cooling pipes. For safety reasons, the pipes are going to be tested prior to the assembly of the cooling system to determine the maximum pressure that they can withstand before cracking.

Regarding the stresses reached in the ferrite cylinder, they are within the limits of 1 and -1 imposed by the Christensen criterion. Thus, no issues are expected either. It should be noted that the maximum stresses calculated with the full model, within -0.94 and 0.95 as shown in Fig. 6.16, compare to the -0.95 and 0.69 predicted by the simplified model: The compressive stress generated at the inside of the cylinder is similar in both cases. However, the full model predicts higher tensile stress at the outside of the cylinder over a limited area.

Required minimum wall thickness of the pipes

The minimum wall thickness of the cooling pipes has been calculated following the guidelines presented in [42]. This technical specification is based on the *European Norm EN13480-5 for metallic industrial piping: Inspection and Testing*. This standard is valid for steels, so to extrapolate the results to the annealed copper OFE, conservative parameters have been chosen for the calculation.

First of all, the maximum allowable stress in the pipes must be estimated. It is determined by the following:

$$f = \min \left(\frac{R_{p0.2}}{1.9}; \frac{R_m}{3} \right) = 17.5 \text{ MPa} \quad (6.13)$$

Where $R_{p0.2}$ is the offset yield point, used in ductile metals that do not have a well defined yield point, as it is the case of the annealed copper, with a value of 33.3 MPa. R_m is the ultimate tensile strength, with a value of 210 MPa.

With this data the minimum wall thickness can be calculated. For the case of a straight pipe, it is defined by the following:

$$t = \max \left(\frac{p_c d_0}{2f + p_c}; \frac{p_c d_{ext}}{2f - p} \right) = 0.81 \text{ mm} \quad (6.14)$$

Where t is the minimum wall thickness, d_0 is the internal diameter, d_{ext} is the external diameter (in this case the perimeter of the square cross-section), f is the maximum allowable stress previously calculated and p_c is the internal pressure of the pipes. For this last value,

although the maximum inlet pressure of the LHC demineralized water network is limited to 16 bar [20], 50 bar has been assumed to include a safety margin.

Nevertheless, as the calculated value of minimum wall thickness with the formula 6.17 is for straight pipes, it does not take into consideration the distortion in the cross section produced in the bends. For that, the minimum wall thickness should be re-calculated with the following formula [42]:

$$t_{bend} = \max \left(t \frac{\frac{R}{d_0} - 0.25}{\frac{R}{d_0} - 0.5}; t \frac{\frac{R}{d_0} + 0.25}{\frac{R}{d_0} + 0.5} \right) = 0.96 \text{ mm} \quad (6.15)$$

Where R is the minimum bending radius of the pipes, that has been obtained from the norm for annealed copper pipes (12 mm). The obtained minimum wall thickness, 0.96 mm, is smaller than the actual wall thickness of the pipes, 1 mm. Hence, it can be concluded that the selected dimensions of the copper pipe fulfill the requirements. For safety reasons, a cross-check with experimental data is needed: A pressure test has been done on the cooling pipe assembly to verify that it can withstand the expected pressure. For that, a hydrostatic pressure is applied during a minimum time using pressurized water in a controlled environment. Visual inspection of the tested object is done before and after the test to verify that there are no signs of damage. A full-scale prototype of the the copper pipe has been produced and tested, successfully performing at 25 bar for 1 hour 15 min, withstanding these conditions without any problem. Results of this test can be found in [58]. Note that 25 bar are well above the maximum inlet pressure available in the LHC water cooling circuit (16 bar). This confirms that the cooling system can operate with a reliable safety margin.

Number of turns of the cooling pipe around the copper tube

In order to determine the number of turns needed around the copper tube to ensure a proper heat extraction, the minimum surface required to evacuate the 364 W generated in the rings must be first calculated. Note that the temperature drop between the internal surface of the pipe and the average temperature of the water has been imposed to be 2.5°C as a design condition:

$$A_{pipe} = \frac{Q}{h (T_{pipesurface} - T_{water})}, \quad (6.16)$$

where Q is the heat generated in the ferrite cylinder (It has been assumed that all the heat flows in one direction, from the tube to the cooling pipe, and radiation to surrounding components is not considered), h is the convection coefficient previously calculated and A_{pipe}

is the heat transfer surface, which corresponds to the internal surface of the pipe. From the obtained value, the length of the pipes in contact with the tube can be obtained by:

$$L_{pipe} = \frac{A_{pipe}}{\pi D_{int}}, \quad (6.17)$$

where L_{pipe} and D_{int} are the length and the internal diameter of the cooling pipe, respectively.

Finally, the number of turns is defined by:

$$N_{turns} = \frac{L_{pipe}}{\sqrt{p^2 + (2\pi(R_{tube} + (\frac{D_{ext}}{2})))^2}} \quad (6.18)$$

Being p the pitch, R_{tube} the external radius of the copper tube, and D_{ext} the external dimension of the cooling pipe.

The minimum number of turns obtained from Eq. 6.18 is 3.3. However, for simplifying the manufacturing, the next highest integer number is chosen, which results in 4 turns. For this new value, the following parameters have been recalculated:

	Initial estimations	Iteration for $N_{turns}=4$
Total power (W)	364	
Convection coefficient ($W/(m^2 \cdot K)$)	9115	
ΔT ($^{\circ}C$)	2.5	2.1
Pipe Length (m)	1.13	1.34
Pitch (m)	0.0125	
Number of windings	3.38	4

Table 6.3 Calculation of the number of windings.

6.2.4 Building a prototype

Prior to the fabrication of the first prototype, the feasibility of joining a ferrite cylinder to a copper tube has been studied. The main issue for joining these two materials is the high mismatch of the coefficient of thermal expansion (CTE) between copper ($17-20 \times 10^{-6}/K$ [19]) and ferrite ($7-8 \times 10^{-6}/K$) [41]. The concept of the brazing assembly has to comply with the following requirements:

1. Withstand temperatures up to $300^{\circ}C$ during a bake-out.

2. Good thermal contact.
3. Low residual stresses on the ferrite cylinder due to its low mechanical strength.

An option to limit residual stresses in hybrid brazing assemblies would be to use low melting point filler metals. The above mentioned requirements for the bake-out temperature exclude commonly used alloys such as SnAg3.5, with a melting temperature of 221°C. Furthermore, the surface preparation without using fluxing agents for vacuum brazing at low temperatures is usually delicate. At CERN, a frequently applied brazing technique to join copper to Al_2O_3 consists of using the silver-copper eutectic alloy (*American Welding Society (AWS)*) BAg-8, with melting temperature of 779°C: The high plasticity at high temperatures and the low re-crystallization temperature of pure copper allows ceramic-metal transitions with low residual stresses.

For proving the feasibility of the brazing technique with copper and ferrite, first trials were performed on available ferrite rings, which are smaller than the ones for the final design.

Pre-treatments of the ferrite rings

The brazing with BAg-8 requires a gap of less than 0.1 mm in the joint between the ferrite and the copper rings. This is needed to maintain the liquid filler metal by capillary force in the joint gap during the brazing process. However, the available ferrite rings had a variance of more than ± 0.5 mm on the outer diameter, so first they were machined to meet the required tolerance before starting the brazing process.

As ferrite is a ceramic substrate, the joining surface has to be prepared with a metallic surface coating to provide sufficient wettability with the liquid brazing filler metal during the brazing process. In this case, an active brazing alloy was applied as paste, manually by brush, on the outer diameter of the ferrite ring. The alloy used was AWS BAg-64 ("BrazeTec CB10") containing 10 wt.-% of titanium, which provides a chemical bond between the oxide-compounds in the ferrite and the metallic filler material.

Prior to the coating process, the ferrite material has to be thermally treated in order to remove any volatile species, which are problematic for the vacuum quality and detrimental to the coating quality. Attempts without firstly outgassing the ferrite parts showed serious peeling-off of the metallization layer (see left hand side of Fig. 6.17).

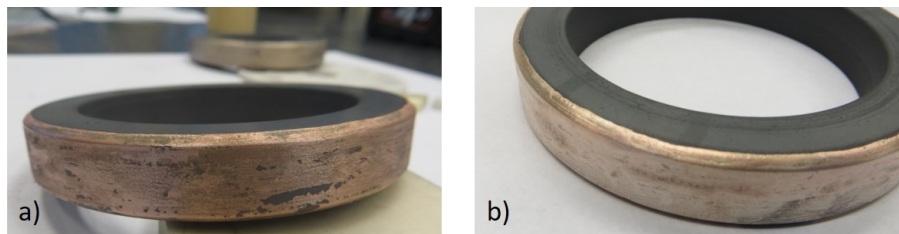


Fig. 6.17 Ferrite rings after metallization with BAg-64 paste: a) Without prior outgassing; b) With prior outgassing (*Courtesy: F. Motschmann.*)

The following steps are performed for the as-delivered ferrites before the brazing treatment:

1. Air-Firing at 1,000°C for 2 h; maximum heating/cooling-rate 50°C/h;
2. Vacuum firing in high vacuum ($< 10^{-5}$ mbar) at 1,000°C for 2 h; maximum heating/cooling-rate 50°C/h;
3. Painting with BAg-64 paste and drying;
4. Heat treatment in high vacuum with maximum temperature of 850°C (in this case temperature is limited to avoid excessive silver evaporation).

Brazing test assembly to prove the feasibility

A simple test assembly, using available ferrite rings, was designed and realized as shown in Fig. 6.18.

The principle of a brazing assembly is shown in Fig. 6.18. During the thermal cycle the copper support is compressed in the area of the joint by molybdenum wires which maintain a small gap between ferrite and copper or even causes a compressive load on the joint.

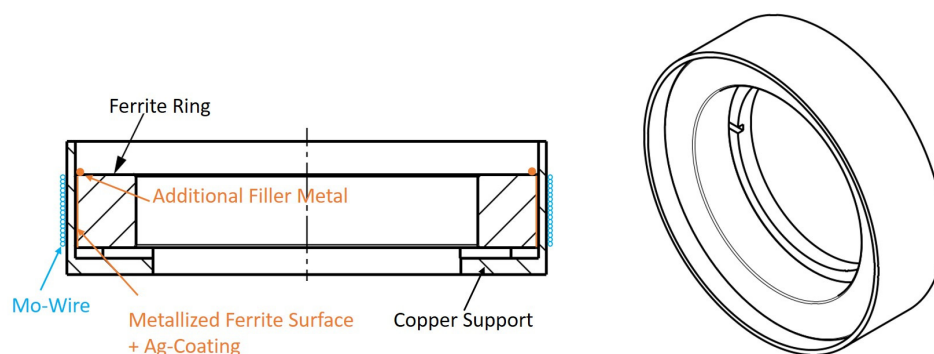


Fig. 6.18 Assembly of ferrite ring and copper ring for the brazing test. (*Courtesy: F. Motschmann.*)

Two test were performed, and the quality of the brazing was assessed by ultrasound tests. The brazing in the first trial showed a local coverage with filler-metal of approximately 33% of the circumference - see the upper part of Fig. 6.19. This was not a good result, and it was thought to be caused by an insufficient clearance available to obtain the flow of the filler from above. To solve this, it was necessary to cover the whole joint surface with a brazing filler material, which can be realized by plating the metallized surface of the ferrite with an additional silver layer that reacts, during the heat treatment, with the copper of the support to the eutectic phase and creates in-situ a liquid filler material. A second trial was done with the additional silver layer on the surface of the ferrite, and a sound joint contact between ferrite and copper could be realized over approximately 90% of the circumference, as shown in the lower part of Fig. 6.19.

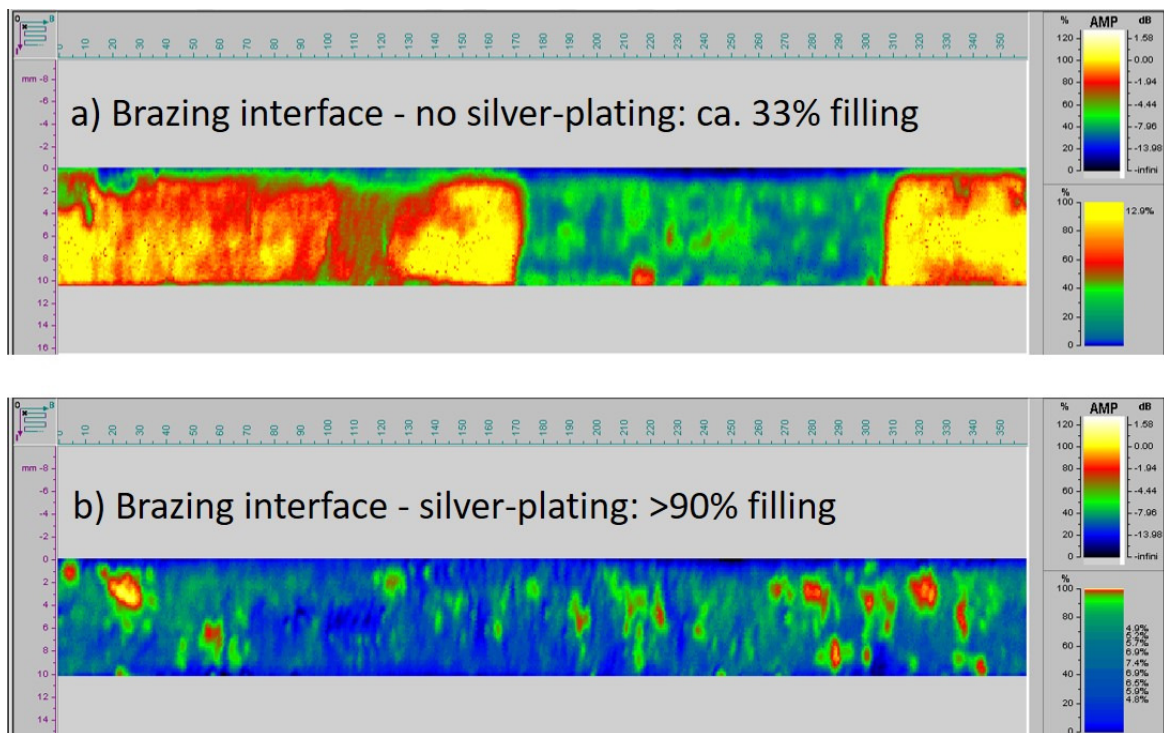


Fig. 6.19 Assembly of ferrite ring and copper ring for the brazing test. *Courtesy: F. Motschmann.*

Subsequent analysis showed that neither of the brazing tests resulted in any visually observed cracking of the ferrite rings. This promises the possibility to keep the induced stresses, during the cooling down after the brazing process, sufficiently low.

Once the ferrite cylinders with the final, bigger dimensions, were received, the brazing technique was applied to them. Two trials were performed before the assembly of the final

prototype. Note that achieving a sound joint over a bigger surface is more challenging, and the risk of cracking of the ferrites is higher too.

The first trial showed significant voids in the joints. This can be appreciated in Fig. 6.20:

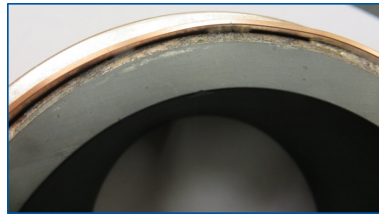


Fig. 6.20 First brazing applied to the ferrite cylinder of final dimensions. *Courtesy: F. Motschmann.*

A second trial was done, and this time the joint was good enough but there were cracks in the ferrite cylinder along the axis direction, as shown in Fig. 6.21:

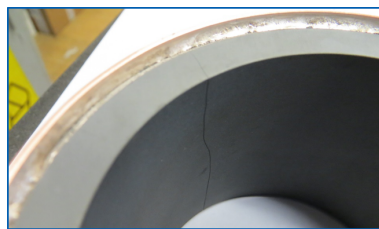


Fig. 6.21 Second brazing applied to the ferrite cylinder of final dimensions. *Courtesy: F. Motschmann.*

Finally, a third trial showed no cracks and the joint was good. It was approved for installation in one of the MKIs.

Production of final prototype

The water cooling pipe was brazed around the copper tube and a leak-tight flange was installed at the entrance of the pipe (see Fig 6.22). The final assembly showed no cracks and minor voids in the bonding.

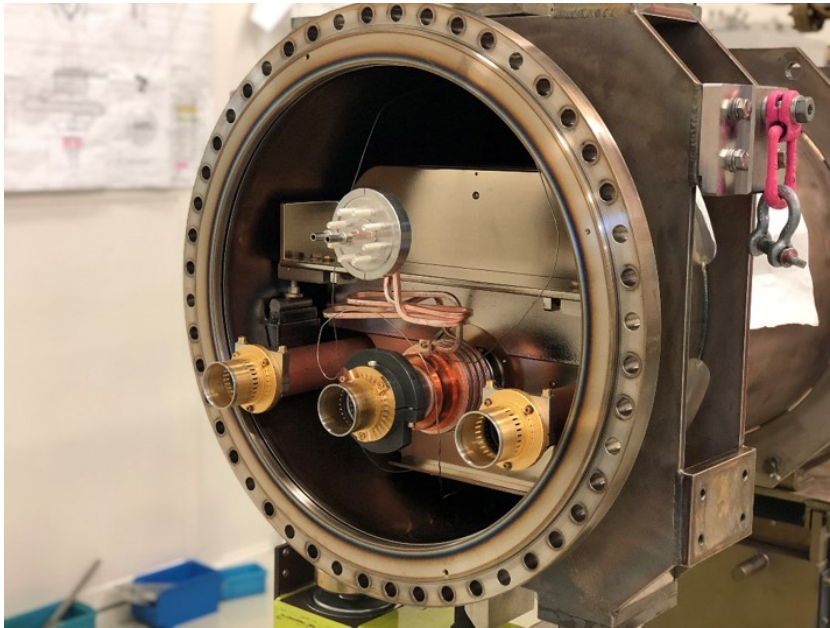


Fig. 6.22 Cooling system installed in the MKI magnet.

As the assembly is going to be installed inside a MKI magnet, which operates under ultra-high vacuum conditions, it needs to pass stringent controls to verify its vacuum compatibility. For that, residual gas analysis and leak tests were performed at CERN by the vacuum experts and the results were positive. The assembly was approved for installation.

Chapter 7

Conclusions

7.1 Summary

The motivation of this thesis was to find a method to limit the temperature of the ferrite yokes of the LHC injection kicker magnets below their Curie point with HL-LHC beam circulating. The necessity of having a better understanding of both the beam induced power loss and the thermal behaviour of these magnets became apparent when, after a series of long fills during Run1 operation, the ferrite yoke Curie temperature was reached in one kicker magnet and LHC operation had to be paused while the magnet cooled, to avoid mis-injection of the beam.

Thanks to the studies performed in the context of this thesis, it was possible to gain knowledge about the amount of power deposited due to the interaction with the circulating beam, as well as its distribution inside the magnets, which was key to propose a cooling method.

Finite element models were developed with ANSYS for thermal analysis. Those models were adapted during the different stages of the thesis to the changes in the power loss calculations, which evolved to give a more representative power distribution and higher accuracies. The models were validated by benchmarking with measured temperatures during LHC operation. Thanks to this, it was found that, for some models, it was necessary to apply a scaling factor to the calculated beam induced power loss so that the temperature predictions matched the LHC measurements. The value of the scaling factor was thoroughly studied for the different models of power distribution to ensure that all the thermal studies were valid.

First of all, analyses were performed to obtain the temperatures in the magnets for different LHC operation scenarios, to determine in which cases they would be above the Curie threshold. As a result of the studies, it was concluded that heating issues were expected for HL-LHC operation scenarios if measures were not taken.

Several alternatives for cooling the magnet yokes were investigated. At the initial stages of the project, a passive cooling method was pursued due to the challenges imposed by the installation of a liquid cooling system inside an environment with both high voltage and ultra high vacuum.

In the context of the passive cooling techniques, the investigation was directed towards improving the radiative cooling inside the tanks. Indeed, one of the greatest limitations for the heat extraction out of the yokes was the low thermal emissivity of the internal surface of the vacuum tanks. The results from simulations confirmed that this approach would reduce the temperature of all the components for HL-LHC operation, but even when assuming an emissivity of 0.8, the first three yokes would still be above their Curie temperature. However, given the fact that this passive cooling method would not imply time consuming and expensive mechanical changes to the magnet, it was kept as the core solution while other complementary measures were investigated.

A test campaign was launched with different companies and institutions to identify and characterize high emissivity, vacuum compatible, treatments. In general, all the investigated treatments showed remarkable increase of the thermal emissivity at the required wavelengths, but the applicability to the whole inside of the tank, given the large dimensions and shape, would have required long times for some of the techniques. Besides, in some cases the tools and equipment had to be re-designed and adapted to the dimensions of the tanks, which remarkably increased the costs. In the end, two coatings based on thermal spraying processes were found to be the best alternatives thanks to their adaptability. Nevertheless, the increase of emissivity would not be sufficient for HL-LHC and hence would need to be combined with another measure to reduce the temperature of the first three yokes. Finding a suitable treatment for increasing the emissivity took a significant time as all the samples had to be tested. By the time the vacuum compatibility tests, compulsory for installing any new material and coating inside the LHC vacuum, were finished, the studies of the complementary measures were well advanced, and some approaches were showing promising results, even without the need of increasing the emissivity.

Although a liquid cooling system was initially discarded because of the pulsed high voltage environment, simulations showed that it was the most efficient option. The investigation was then oriented to the implementation of a reliable cooling system to operate safely in the LHC vacuum environment. Based on the results of extensive thermal analyses, the temperatures of all the yokes would be kept below the Curie threshold by installing two cold plates with embedded water cooling pipes in direct contact with the first and third yokes. However, the design of such a system was particularly challenging due to the limited space available, and the intrinsic risk of using active cooling in contact with the ferrite yokes, which

are at pulsed high voltage. In addition, a separate cooling system was needed to cool down the ferrite rings, whose predicted temperatures were well above their Curie point. Note that even though the ferrite rings are not critical for the functionality of the kicker magnets, if their permeability falls, the amount of power that they absorb diminishes too. This power would be deposited in the yokes instead, significantly increasing the yoke temperature beyond the Curie point. The mechanical design and assembly of the two independent cooling systems (one for the yokes and another for the rings) would be very complicated given the lack of space and the brittleness of the materials to be cooled.

Thermal simulations showed that, by relocating a significant portion of the heat deposition from the yokes to the ferrite rings, plus installing a cooling system for the rings, a significant reduction in the temperatures of all the components could be achieved for HL-LHC operation. This was considered the best approach because the rings could be more easily cooled than the yokes as they are not pulsed at high voltage and are more easily accessible. Thus a colleague launched beam coupling impedance studies to study this idea and confirmed that it was possible not only to reduce the total beam induced power deposition in the magnet, but also to move a substantial portion of the deposited power from the ferrite yokes to the rings. To do so, modifications to the ferrite ring assembly were proposed and they were implemented in the historically hottest magnet, MKI8D, during YETS17-18, to test its performance with real beam during LHC operation. Indeed, during 2018 operation with beam, the upgraded MKI8D presented the lowest measured temperatures of all the MKI magnets, proving the success of the modifications in reducing the power. Nevertheless, due to time constraints, the upgraded MKI8D did not have the cooling system installed. Thus, it still would not be adequate for HL-LHC.

The conception and design of the cooling system in the ferrite rings was particularly challenging due to the difficulties imposed by installing a liquid cooling system in an ultra-high vacuum environment. Besides, ferrites are extremely difficult materials for heat extraction due to the intrinsic poor mechanical properties and limited thermal conduction. First of all, it was decided to substitute the set of nine ferrite rings by one tube to improve and guarantee the longitudinal heat transfer. The water-cooling pipes could not be directly attached to this ferrite tube, but instead to a copper tube which surrounded it. A theoretical analysis, based on a thermal network model, was used to identify the most critical parameters for the heat extraction from the tube to the cooling circuit. The thermal contact between the ferrite and the copper tube was identified as crucial. To that end, after investigating different alternatives, it was decided to braze the copper to the ferrite. However, this was very challenging given the high mismatch of the coefficient of thermal expansion of both materials. Indeed, trials had been reported before but with no success. To study and prove

the feasibility, several prototypes were built for testing the brazing technique using available ferrite rings. After some iterations for optimizing the technique, a sound joint was achieved on over 90 % of the surface.

This optimized technique was applied to the ferrite cylinders with the final dimensions once they were received. The first trials showed voids in the joint and ferrite cracking in the longitudinal direction. After some iterations, a good brazing was achieved, with minor voids in the joint and no observable crackings.

Different configurations of the cooling system were investigated which, together with the dimensions, were optimized by iterating the power loss calculations with CST and the thermo-structural analysis with ANSYS, aiming not only at reducing the total heat deposited but also avoiding areas of high power density, to prevent cracking of the ferrite rings. Given the criticality of the application, the 3D power distribution obtained with the CST software was imported accurately to ANSYS to properly assess the thermal stresses due to temperature gradients between the cooled surface and the hot areas in the ferrite tube. Using this technique, a local hot-spot, which could result in cracking of the ferrite tube, was identified. As a result, the design of the ferrite tube assembly was modified to have a more uniform power distribution by means of an extra inner copper cylinder that changed the beam coupling impedance. The effectiveness of this was confirmed with ANSYS simulations.

According to predictions, the proposed solution would maintain the temperatures of all the components well below the Curie point. In particular, the hottest point of the ferrite tube would be at 80°C, and the first and hottest ferrite yoke would only reach 47°C. These calculations are done with a safety factor applied to the power loss of 2.5.

A full prototype of the cooling system has been built. Before its installation, vacuum compatibility tests have been performed on the whole assembly to ensure that it can operate in the LHC vacuum environment. The results of these tests have been positive and the cooling system is officially approved for installation.

7.2 Contributions to the state of the art

This thesis has contributed to the state of the art of the technologies used for limiting the operational temperature in kicker magnets installed in particle accelerators by proposing a combined method which targets both the reduction and redistribution of beam induced power deposition to accessible areas inside the magnets, as well as the heat extraction out of those localized areas by implementing an active cooling system. This was an innovative approach because the solutions proposed so far in similar systems were not applicable to the LHC kicker magnets given their uniqueness: As these magnets are installed in the LHC,

the world's largest and most powerful particle accelerator, the induced heating due to the interaction with the circulating beam was particularly high. Not only that, but they were designed to meet the stringent LHC operational requirements, having to provide a fast high voltage pulse under ultra high vacuum conditions, which greatly limits the choice of materials and cooling components to be installed inside them without compromising the operation.

Although this thesis was oriented to find a specific solution to the overheating of the LHC kicker magnets expected during HL-LHC operation with higher intensity beams, the presented studies establish the bases to be followed for the design of kicker magnets in future high energy accelerators, providing a better understanding of how to deal with the beam induced heating caused by high energy beams. It must be highlighted that there is an interest of building high energy and luminosity accelerators as they will allow to open new frontiers in the particle physics research.

This thesis has also contributed to the state of the art of the techniques employed for cooling ferrite in vacuum environments. This material is widely used in electronics and high frequency components. The application of ferrites in kicker magnets is of interest due to the ferromagnetic properties and the high magnetic permeability, which makes this material ideal for providing fast magnetic pulses and meet the operational requirements. However, it has poor thermal and mechanical properties: The intrinsic low thermal conductivity and the brittleness make the heat extraction very challenging.

The most commonly applied cooling methods for ferrite were based on active cooling, ensuring a good contact to the heat sink with thermal greases. However, this was not applicable to the specific case of the LHC kicker magnets due to the limitations imposed by the ultra high vacuum environment, not being allowed the use of thermal greases. Due to this, the choice of materials that could be employed was greatly limited. Not only that, but the heat generation was very localized in the surface of the ferrite rings facing the beam, where it was not possible to access and put in contact any cooling component. The only alternative was to cool down the opposite face, but the thermal resistance through the thickness of the rings was considerably high due to the low thermal conductivity. Thus, ensuring a good thermal contact to the heat sink was key to achieve sufficient heat extraction. As thermal greases were not applicable, other techniques were investigated and in the end, brazing the ferrite to a cooled copper plate with water cooling loops was the proposed solution. Trials of this technique had been reported in previous studies but with no success, attributed to the high mismatch of the coefficient of thermal expansion of both materials. However, after several iterations to optimize the technique at CERN, successful results were achieved, proving the feasibility. This innovative approach can be of interest for application in cases where cooling

of ferrite is needed in vacuum environments, as it has demonstrated to be an effective method to ensure good thermal contact.

7.3 Future work

The cooling system has been produced and fully assembled in one MKI magnet, and it is expected to be installed in the LHC in 2020 during LS2. Its performance will be tested during the next LHC operation period (Run3, 2021-2023), when the beam intensities will still be lower than the ones expected for HL-LHC operation and the temperatures, even without cooling system, are predicted to be below Curie temperature.

This magnet has been equipped with a set of temperature sensors positioned in strategic locations to provide key information about the performance of the cooling system. The data collected throughout the two years period of Run3 will be used for benchmarking the thermal models developed in this thesis. This will allow to estimate realistically the parameters used for the definition of the boundary conditions in the electromagnetic and thermal models. Subsequently, modifications can be studied to further improve the design. It must be highlighted that the performance of the cooling system with real beam cannot be reproduced faithfully in a lab, as the heat distribution depends on the beam interaction. Thus there is a degree of uncertainty in the definition of the models, and even though a safety factor has been applied in the design calculations, key information can be obtained from the performance under real conditions. Run3 will be the opportunity to test it and make necessary modifications. If the cooling system proves to be reliable and effective based on the experience that will be gained, it will be implemented in all the MKI magnets to ensure the safe operation with HL-LHC beam in 2025.

References

- [1] Ang, A. S. M., Sanpo, N., Sesso, M. L., Kim, S. Y., and Berndt, C. C. (2013). Thermal Spray Maps: Material Genomics of Processing Technologies. *Journal of Thermal Spray Technology*, 22(7):1170–1183.
- [2] ANSYS, Inc. (2016). *ANSYS Mechanical Users Guide, Release 17.1*.
- [3] Apollinari, G., Alonso, I. B., Brüning, O., Fessia, P., Lamont, M., Rossi, L., and Tavian, L. (2017). *High-Luminosity Large Hadron Collider (HL-LHC): Technical Design Report*. CERN.
- [4] Barnes, M., Adraktas, P., Calatroni, S., Caspers, F., Ducimetière, L., Gomes Namora, V., Mertens, V., Noulibos, R., Taborelli, M., Teissandier, B., Uythoven, J., and Weterings, W. (2013a). Reduction of surface flashover of the beam screen of the lhc injection kickers. In *Proc. 4th International Particle Accelerator Conference (IPAC'13), Shanghai, China*.
- [5] Barnes, M., Caspers, F., Ducimetière, L., Garrel, N., and Kroyer, T. (2006). The Beam Screen for the LHC Injection Kicker Magnets. In *Proc. 10th European Particle Accelerator Conference (EPAC'06), Edinburgh, Scotland*.
- [6] Barnes, M., Caspers, F., Ducimetière, L., Garrel, N., and Kroyer, T. (2007). An Improved Beam Screen for the LHC Injection Kickers. In *Particle Accelerator Conference, 2007. PAC. IEEE*, pages 1574–1576.
- [7] Barnes, M. et al. (2014). Cooling of the LHC Injection Kicker Magnet Ferrite Yoke: Measurements and Future Proposals. In *Proc. 5th International Particle Accelerator Conference (IPAC'14), Dresden, Germany, June 15-20, 2014*, number 5 in International Particle Accelerator Conference, pages 544–546. <https://doi.org/10.18429/JACoW-IPAC2014-MOPME075>.
- [8] Barnes, M. et al. (2018). An Upgraded LHC Injection Kicker Magnet. In *Proc. 9th International Particle Accelerator Conference (IPAC'18), Vancouver, BC, Canada*, number 9 in International Particle Accelerator Conference, pages 2632–2635, Geneva, Switzerland. JACoW Publishing. <https://doi.org/10.18429/JACoW-IPAC2018-WEPMK003>.
- [9] Barnes, M., Mertens, V., Garrel, N., Goddard, B., Weterings, W., and Ducimetière, L. (2012). Analysis of Ferrite Heating of the LHC Injection Kickers and Proposals for Future Reduction of Temperature. In *Conf. Proc.*, volume 1205201.
- [10] Barnes, M. and Weterings, W. (2013). Cooling Water Connections around the Injection Kicker Magnets MKIMA. Technical Report LHC-MKIMA-EC-0001, CERN, Geneva.

- [11] Barnes, M. J., Adraktas, A., Bregliozzi, G., Goddard, B., Ducimetière, L., Salvant, B., Sestak, J., Vega Cid, L., Weterings, W., and Yin Vallgren, C. (2017). Operational Experience of the Upgraded LHC injection Kicker Magnets during Run 2 and Future Plans. *Journal of Physics: Conference Series*, 874(CERN-ACC-2017-310. 1):012101. 7 p.
- [12] Barnes, M. J., Adraktas, P., Baglin, V., Bregliozzi, G., Caspers, F., Calatroni, S., Day, H., Ducimetière, L., Garlaschè, M., Gomes Namora, V., Jimenez, J. M., Magnin, N., Mertens, V., Métral, E., Salvant, B., Taborelli, M., Uythoven, J., and Weterings, W. (2013b). Upgrade of the LHC Injection Kicker Magnets. (CERN-ACC-2013-0077).
- [13] Barnes, M. J., Ducimetière, L., Fowler, T., Senaj, V., and Sermeus, L. (2010). Injection and Extraction Magnets: Kicker Magnets. *CERN-2010-004*, pp. 141-166.
- [14] Barnes, M. J., Mertens, V., Garlaschè, M., Day, H., Sobiech, Z., Weterings, W., Gomes Namora, V., Ducimetière, L., Caspers, F., Uythoven, J., et al. (2013c). Beam Induced Ferrite Heating of the LHC Injection Kickers and Proposals for Improved Cooling.
- [15] Baumeister, P. (2004). *Optical Coating Technology*. SPIE Press monograph. SPIE Optical Engineering Press.
- [16] Bejar Alonso, I. and Rossi, L. (2015). HiLumi LHC Technical Design Report: Deliverable: D1.10. Technical Report CERN-ACC-2015-0140.
- [17] Bergman, T. L., Incropera, F. P., DeWitt, D. P., and Lavine, A. S. (2011). *Fundamentals of Heat and Mass Transfer*. John Wiley & Sons.
- [18] Berrig, O. E. (2018). Beam Impedance. Technical Report CERN-ACC-SLIDES-2018-0002, CERN, Geneva.
- [19] Brandes, E., Brook, G., and Paufler, P. (1992). *Smithells Metals Reference Book*. Butterworth-Heinemann, 7th edition.
- [20] Brüning, O. S., Collier, P., Lebrun, P., Myers, S., Ostojic, R., Poole, J., and Proudlock, P. (2004). *LHC Design Report: the LHC Infrastructure and General Services*, volume 2 of *CERN Yellow Reports: Monographs*. CERN, Geneva.
- [21] Bruzzone, A., Costa, H., Lonardo, P., and Lucca, D. (2008). Advances in Engineered Surfaces for Functional Performance. *CIRP Annals-Manufacturing Technology*, 57:750–769.
- [22] Cattenoz, G., Baglin, V., Bregliozzi, G., Calegari, D., Gallagher, J., Marraffa, A., and Chiggiato, P. (2014). Vacuum Acceptance Tests for the UHV Room Temperature Vacuum System of the LHC during LS1. (CERN-ACC-2014-0270).
- [23] Chao, A. W. (1993). *Physics of Collective Beam Instabilities in High Energy Accelerators*. Wiley.
- [24] Chiggiato, P., Ferreira Somoza, J. A., and Bregliozzi, G. (2018). Criteria for Vacuum Acceptance Test. Technical Report CERN-ACC-V-ES-0001, CERN, Geneva.

- [25] Chimiderouil (2018). Fiche de Sécurité du Produit NET INOX. Technical Report CERN-ACC-2015-0140.
- [26] Chmielinska, A., Popovic, B., Barnes, M. J., Caspers, F., and Vollinger, C. (2018). Measurements of electromagnetic properties of ferrites as a function of frequency and temperature. *Journal of Physics: Conference Series*, 1067:082018.
- [27] Christensen, R. M. (2007). A Comprehensive Theory of Yielding and Failure for Isotropic Materials. *Journal of Engineering materials and Technology*, 129(2):173–181.
- [28] Churchill, S. (1975). Correlating Equations for Laminar and Turbulent Free Convection from a Horizontal Cylinder. *International Journal of Heat Mass Transfer*, 18(1049):53.
- [29] Cid, L. V., Abánades, A., Barnes, M. J., Mostchmann, F., Vlachodimitropoulos, V., and Weterings, W. (2019). Conception and design of a cooling system for the lh injection kicker magnets. *Nuclear Instruments and Methods in Physics Research Section A: Accelerators, Spectrometers, Detectors and Associated Equipment*, 916:296 – 305.
- [30] Cooling, E. (1997). Highly Emissive Ion Beam Textured Surfaces for Improved Cooling of Electronic Devices. <https://www.electronics-cooling.com/1997/09/highly-emissive-ion-beam-textured-surfaces-for-improved-cooling-of-electronic-device/>.
- [31] Davis, J. R. et al. (2004). *Handbook of thermal spray technology*. ASM international.
- [32] Day, H., Barnes, M., Caspers, F., Metral, E., Salvant, B., and Uythoven, J. (2014). Beam Coupling Impedance of the New Beam Screen of the LHC Injection Kicker Magnets. In *Proc. 5th International Particle Accelerator Conference (IPAC'14), Dresden, Germany*, pages 1627–1629, Geneva, Switzerland. JACoW Publishing. <https://doi.org/10.18429/JACoW-IPAC2014-TUPRI030>.
- [33] Day, H., Barnes, M., Caspers, F., Metral, E., Salvant, B., Zannini, C., and Jones, R. (2011). Coaxial Wire Measurements of Ferrite Kicker Magnets. (CERN-ATS-2011-275):4 p.
- [34] Day, H., Barnes, M., Ducimetière, L., Cid, L. V., and Weterings, W. (2016). Current and Future Beam Thermal Behaviour of the LHC Injection Kicker Magnet. In *Proc. 7th International Particle Accelerator Conference (IPAC'16), Busan, Korea*, pages 3615–3618, Geneva, Switzerland. JACoW Publishing. doi:10.18429/JACoW-IPAC2016-THPMW031.
- [35] Day, H., Barnes, M., and Feliciano, L. (2015). Impedance Studies of the LHC Injection Kicker Magnets for HL-LHC. In *Proc. 6th International Particle Accelerator Conference (IPAC'15), Richmond, VA, USA*, number 6 in International Particle Accelerator Conference, pages 370–373, Geneva, Switzerland. JACoW. <https://doi.org/10.18429/JACoW-IPAC2015-MOPJE038>.
- [36] Day, H., Barnes, M. J., Caspers, F., Jones, R., Metral, E., and Salvant, B. (2013a). Evaluation of the Beam Coupling Impedance of New Beam Screen Designs for the LHC Injection Kicker Magnets. In *Proc. 4th International Particle Accelerator Conference (IPAC'13), Shanghai, China*, pages 1649–1651, Geneva, Switzerland. JACoW Publishing.

- [37] Day, H., Barnes, M. J., Caspers, F., Jones, R. M., Salvant, B., and Métral, E. (2013b). Evaluation of the Beam Coupling Impedance of New Beam Screen Designs for the LHC Injection Kicker Magnets. (CERN-ACC-2013-0097):4 p.
- [38] Day, H. A. (2013). *Measurements and Simulations of Impedance Reduction Techniques in Particle Accelerators*. PhD thesis, University of Manchester.
- [39] Denard, J. C. (2009). Beam Current Monitors. <https://cds.cern.ch/record/1213275>.
- [Denton Vacuum] Denton Vacuum. *Magnetron Sputtering Deposition Systems- Emissivity treatments/Optical coatings*.
- [41] Ferroxcube International Holding B.V. 2013 (2013). *Soft Ferrites and Accesories Data Handbook*.
- [42] Garlasche, M. (2012). Minimum Thickness for TCTP Cooling Tubes. Technical report, CERN, Geneva.
- [43] Guglielmini, P. (2006). Corrosion Phenomena in Demineralized Water Cooling Circuits. Technical note, CERN, Geneva.
- [44] Heimann, R. B. (2008). *Plasma-spray Coating: Principles and Applications*. John Wiley & Sons.
- [45] Herr, W. and Muratori, B. (2006). Concept of Luminosity. <https://cds.cern.ch/record/941318>.
- [46] Holzer, B. J. (2014). Higher-order Modes and Heating. (arXiv:1501.07103):14 p. Contribution to the CAS-CERN Accelerator School: Superconductivity for Accelerators, Erice, Italy, 2013, edited by R. Bailey.
- [47] Juhasz, J. and Best, S. (2011). Surface Modification of Biomaterials by Calcium Phosphate Deposition. In *Surface Modification of Biomaterials*, Woodhead Publishing Series in Biomaterials, pages 143 – 169.
- [48] Kelly, P. and Arnell, R. (2000). Magnetron Sputtering: A Review of Recent Developments and Applications. *Vacuum*, 56(3):159 – 172.
- [49] Lee, C., Kim, A., and Kim, J. (2015). Electrochemically Etched Pporous Stainless Steel for Enhanced Oil Retention. *Surface and Coatings Technology*, 264:127–131.
- [50] Maglioni, C., Delonca, M., Costa, M. G., and Vacca, A. (2014). Use of Silicon Carbide as Beam Intercepting Device Material: Tests, Issues and Numerical Simulations. In *Proc. 5th International Particle Accelerator Conference (IPAC'14), Dresden, Germany, June 15-20, 2014*, number 5 in International Particle Accelerator Conference, pages 3998–4000, Geneva, Switzerland. JACoW. <https://doi.org/10.18429/JACoW-IPAC2014-THPRI096>.
- [51] Mantelli, M. and Yovanovicht, M. (2002). Thermal contact resistance. *Spacecraft Thermal Control Handbook*, 1.
- [52] Marois, G. L., Dellis, C., Gentzittel, J. M., and Moret, F. (1996). HIPing of Copper Alloys to Stainless Steel. *Journal of Nuclear Materials*, 233-237:927 – 931.

- [53] Meunier, S., Lecercle, A., and Mongelluzzo, A. (2013). Procédure d'Acceptation de Composants pour les Systèmes à Vide des Injecteurs non Étuvés du LHC. Technical report, EDMS 1347196, CERN, Geneva.
- [54] Mikić, B. (1974). Thermal Contact Conductance; Theoretical Considerations. *International Journal of Heat and Mass Transfer*, 17(2):205–214.
- [55] Mobs, E. (2018). The CERN Accelerator Complex - August 2018. Complexe des accélérateurs du CERN - Août 2018. OPEN-PHO-ACCEL-2018-005, <https://cds.cern.ch/record/2636343>.
- [56] National Magnetics Group Inc. (2015). *Magnetic and Advanced Ceramic Materials*.
- [57] Peón-Hernández, G. (2002). Demineralised Water Cooling in the LHC Accelerator. Technical Report ST-Note-2002-037-CV, CERN, Geneva.
- [58] Pochet, C. (2019). Inspection de Securite A la demande sur CRPEMS-00774 (Equipements Mecaniques Speciaux). Technical report, CERN, Geneva.
- [59] PolyCSP ApS (2017). *PolyCSP Absorber Tubes for Concentrated Solar Power*.
- [60] Riihimaki, A. K. (2019). Outgassing Studies of Some Accelerator Materials. <http://cds.cern.ch/record/2679153>.
- [61] Romano, A., Iadarola, G., and Boine-Frankenheim, O. (2018). Electron Cloud Formation in CERN Particle Accelerators and its Impact on the Beam Dynamics. <http://cds.cern.ch/record/2652799>.
- [62] Salemme, R., Baglin, V., Calatroni, S., Chiggiato, P., Garcia-Tabares Valdivieso, E., Jenninger, B., Prever-Loiri, L., Sitko, M., Abdolvand, A., and Wackerow, S. (2018). First Beam Test of Laser Engineered Surface Structures (LESS) at Cryogenic Temperature in CERN SPS Accelerator.
- [63] Shah, Y. T. (2018). *Thermal Energy: Sources, Recovery, and Applications*. CRC Press.
- [64] Sharma, B. K., Kettner, M., Biebersmith, P., and Roldan, N. (2001). Aluminum Nitride vs. Beryllium Oxide for High Power Resistor Products. *Microwave Journal*, 44(11).
- [65] Shigley, J. E. (1972). *Mechanical engineering design; 2nd ed.* McGraw-Hill, New York, NY.
- [66] Sitko, M., Abdolvand, A., Baglin, V., Bajek, D., Calatroni, S., Chiggiato, P., Colling, M., Di Girolamo, B., Garcia-Tabares Valdivieso, E., Jones, T., McIntosh, P., Taborelli, M., and Wackerow, S. (2018). Towards the Implementation of Laser Engineered Surface Structures for Electron Cloud Mitigation. <http://cds.cern.ch/record/2666553>.
- [67] Sobiech, Z., Barnes, M. J., Bouleghimat, S., Ducimetière, L., Garlaschè, M., Kramer, T., Namora, V., Noulibos, R., and Y. Sillanoli, W. W. (2014). Cooling of the LHC Injection Kicker Magnet Ferrite Yoke: Measurements and Future Proposals. In *Proc. 5th International Particle Accelerator Conference (IPAC'14), Dresden, Germany*, number 5 in International Particle Accelerator Conference, pages 544–546, Geneva, Switzerland. <https://doi.org/10.18429/JACoW-IPAC2014-MOPME075>.

- [68] Tajima, T., Asano, K., Furuya, T., Iida, S., Ishi, Y., Kijima, Y., Kokura, S., Mitsunobu, S., Takahashi, T., and Takashina, H. (1993). Bonding of a microwave-absorbing ferrite, TDK IB-004, with copper for the HOM damper of the KEK B-factory SC cavities. Technical Report KEK-Preprint-93-152, KEK, Tsukuba.
- [69] Tang, G. and Abdolvand, A. (2011). Laser-Assisted Highly Organized Structuring of Copper. *Opt. Mater. Express*, 1(8):1425–1432.
- [70] Tang, G., Hourd, A., and Abdolvand, A. (2012). Nanosecond Pulsed Laser Blackening of Copper. *Applied Physics Letters*, 101(23):1–4.
- [71] Teissandier, B. (2016). Preliminary tests to obtain porous and/or rough surfaces on stainless steel (316LN - 304L). Technical report, CERN, TE-VSC, Geneva.
- [72] Teofili, L. et al. (2018). Analysis on the Mechanical Effects Induced by Beam Impedance Heating on the HL-LHC Target Dump Injection Segmented (TDIS) Absorber. In *Proc. 9th International Particle Accelerator Conference (IPAC'18), Vancouver, BC, Canada*, number 9 in International Particle Accelerator Conference, pages 3448–3451. <https://doi.org/10.18429/JACoW-IPAC2018-THPAK092>.
- [73] Timmins, M., Bertarelli, A., Gaxiola, E., and Uythoven, J. (2006). SPS Extraction Kicker Magnet Cooling Design. Technical report, CERN, Geneva. <http://cds.cern.ch/record/707081>.
- [74] Tucker, Robert C., J. (1994). Thermal Spray Coatings. In *Surface Engineering*. ASM International.
- [Vacuum and group at CERN] Vacuum, S. and group at CERN, C. <http://te-dep.web.cern.ch/content/vacuum-surfaces-and-coatings>.
- [76] Valizadeh, R., Malyshev, O. B., Wang, S., Zolotovskaya, S. A., Allan Gillespie, W., and Abdolvand, A. (2014). Low Secondary Electron Yield Engineered Surface for Electron Cloud Mitigation. *Applied Physics Letters*, 105(23):231605.
- [77] Vega, L., Abánades, A., Barnes, M. J., Vlachodimitropoulos, V., and Weterings, W. (2017). Thermal Analysis of the LHC Injection Kicker Magnets. *Journal of Physics: Conference Series*, 874(1):012100.
- [78] Vega Cid, L. et al. (2018). Preliminary Design of a Cooling System for the LHC Injection Kicker Magnets. In *Proc. 9th International Particle Accelerator Conference (IPAC'18), Vancouver, BC, Canada*, pages 2624–2627. JACoW Publishing.
- [79] Vlachodimitropoulos, V., Barnes, M., Chmielinska, A., Ducimetière, L., Cid, L. V., and Weterings, W. (2019). Studies Towards the New Beam Screen System of the LHC Injection Kicker Magnet for HL-LHC Operation. In *Proc. 10th International Particle Accelerator Conference (IPAC'19), Melbourne, Australia*, number 10 in International Particle Accelerator Conference, pages 3982–3985, Geneva, Switzerland. JACoW Publishing. <https://doi.org/10.18429/JACoW-IPAC2019-THPRB074>.

- [80] Vlachodimitropoulos, V., Barnes, M., Ducimetière, L., Cid, L. V., and Weterings, W. (2017). Study of an Improved Beam Screen Design for the LHC Injection Kicker Magnet for HL-LHC. In *Proc. of International Particle Accelerator Conference (IPAC'17), Copenhagen, Denmark*, number 8 in International Particle Accelerator Conference, pages 3471–3474, Geneva, Switzerland. JACoW Publishing. <https://doi.org/10.18429/JACoW-IPAC2017-WEPVA094>.
- [81] Vlachodimitropoulos, V., Barnes, M., Vega Cid, L., and Weterings, W. (2018). Longitudinal Impedance Analysis of an Upgraded LHC Injection Kicker Magnet. In *Proc. 9th International Particle Accelerator Conference (IPAC'18), Vancouver, BC, Canada*, pages 2628–2631. JACoW Publishing. <https://doi.org/10.18429/JACoW-IPAC2018-WEPMK002>.
- [82] Vorobyev, A. Y., Topkov, A. N., Gurin, O. V., Svich, V. A., and Guo, C. (2009). Enhanced Absorption of Metals over Ultrabroad Electromagnetic Spectrum. *Applied Physics Letters*, 95(12):121106.
- [83] Yovanovich, M. (1982). Thermal Contact Correlations. *AIAA paper*, 81:83–95.
- [84] Yovanovich, M. (2006). Micro and Macro Hardness Measurements, Correlations, and Contact Models. In *44th AIAA aerospace sciences meeting and exhibit*.
- [85] Zolotovskaya, S. A., Wackerow, S., Neupert, H., Barnes, M. J., Cid, L. V., Teissandier, B., Fontenla, A. T. P., and Abdolvand, A. (2020). High-performance Thermal Emitters based on Laser-Engineered Metal Surfaces. *Optical Materials Express*, 10(2):622–631.

